Title
Modulating physical and chemical properties of biomaterials in rapid 3D printing

Author
Wang, Pengrui

Publication Date
2019

UNIVERSITY OF CALIFORNIA SAN DIEGO

Modulating Physical and Chemical Properties of Biomaterials in Rapid 3D Printing

A dissertation submitted in partial satisfaction of the
requirements for the degree
Doctor of Philosophy

in

Materials Science and Engineering

by

Pengrui Wang

Committee in charge:

Professor Shaochen Chen, Chair
Professor Shengqiang Cai
Professor Adam Engler
Professor Samuel Ward
Professor Liangfang Zhang

2019

The dissertation of Pengrui Wang is approved, and it is acceptable in quality and form for publication on microfilm and electronically:

Chair

University of California San Diego

2019

DEDICATION

This dissertation is dedicated to my beloved parents, Xinghua Zhang and Yanmin Wang without whom none of my achievements would be possible; to my wife, Yue Zhang, who is always there for me;

to all of my family for their never-ending support;

and in memory of Tianyuan Liu and Xinghai Huang for their enthusiasm in science and exploration.

I am forever grateful to have them in my life.

EPIGRAPH

We build toys. Some of those toys change the world.

– Nassim Taleb *The Black Swan*

I returned, and saw under the sun, that the race is not to the swift, nor the battle to the strong, neither yet bread to the wise, nor yet riches to men of understanding, nor yet favour to men of skill; but time and chance happeneth to them all.

– Ecclesiastes 9:11

TABLE OF CONTENTS

LIST OF FIGURES

LIST OF TABLES

ACKNOWLEDGEMENTS

First and foremost, I would like to thank my advisor, Professor Shaochen Chen, who realized the human's dream of 3D printing living tissues and personally gave me the opportunity to freely explore the frontier in tissue engineering. He is undoubtedly the best boss I would have ever dreamed of at my age. His open mind has nurtured generations of innovators from our group to expand the horizon of our knowledge about regenerative medicines. His understanding, courage and kindness has been a great guidance in both my academic and personal life. We shared the same dream that 3D printing should be able to help with the advancement of biomedical research as well as medical treatment. Under his leadership, our lab has grown into a big family where members support each other wholeheartedly. Some of us have become life-time friends. I am grateful to have worked with his guidance. It has made my pursue of scientific advancement full of joy and love.

I am also thankful for my collaborators who have given me great help for my projects. Particularly, Dr. Ward, Mary Esparza and other co-workers from their research group in School of Health Sciences for their knowledge in physiology and surgery. They have gave me tremendous help in understanding the actual needs in volumetric muscle loss operations and treatments, which became the key motivation for me to develop a elastomeric biodegradable material. I would also like to thank Dr. Cai and Zhaoqiang Song from his group for their profound knowledge in materials and mechanics. Their knowledge on molecular interactions and simulation helped me developed toughening mechanism. Additionally, they also kindly gave me the opportunity to use their Instron machine, given that machine is extremely fragile and hard to maintain. Their trust has helped me finished the double network projects. I am also grateful to have worked with Dr. Xin Li, Dr. Wenqiu Wang and Zheng Zhong from Dr. Kang Zhang's lab. Their knowledge in stem cells not only helped me with the retina work but also helped me build a basic understanding about developmental biology.

I am also grateful to have the opportunity to work with a group of talented researchers in the Chen lab. They have made great contribution in my graduate study. Moreover, we build strong friendships and ran the lab as a big family. I would give my special thank to our post-doc David Berry. His devotion to science has broaden my research scope. He taught me a lot about research, including the right way to develop methodology and systematically analyzing data without bias. Through his patience and diligence in engaging conversations I became who I am today. He has successfully transformed me from a student into a researcher. Besides him, Dr. Wei Zhu is one of the earliest people who guided me through the research journey. His devotion of innovation and determination in execution have been helping me in my later research life. Dr. Justin Liu, a great scientist and artist in the lab, has been a brother figure in my life who mentored me both in academic and in personal life. I also would like to thank Dr. Michelle Ma for her kind help throughout my research at UCSD. She has been a faithful and supportive friend who always cheered me up when we encountered problems. Dr. Claire Yu's dedication and diligence have made her a role model in the lab. I have learned the perseverance and endurance that a PhD student should have to delivery the results. Additionally, Dr. Bingjie Sun has helped me understanding the chemical physics of tough materials, which led me to develop the elastic polymer for 3D printing. Our families have become good friends, too. I would also like to thank the undergraduate volunteers working with me throughout my research journey, Takeyah Campbell, Amy Moran, Frank He, Brian Xi and Trevor Tam. They helped finished most of the tasks presented in this thesis. Without them I can not reach so far. I would also like to thank my co-workers in the lab, Henry Hwang, Shangting You, Jacob Schimelman, Katy Miller, Min Tang and Ben Wisarut for their tremendous help in my project and my personal life. We have become a big family with shared values and supports. Our memories will linger forever and will always be great treasure in our lives.

I would also like to thank Dr. Liangfang Zhang for running a lab full of creative and hardworking researchers, especially my wife Yue Zhang. Their profound knowledge in drug delivery system and release kinetics helped me develop the heparin project. I also appreciate the friendships with many of their group members, namely Jia Zhuang, Yijie Chen, Hua Gong, Fang Chen, Ronnie Fang and others. They have made my life in UCSD full of joys.

I offer special thanks to Dr. Adam Engler for serving on my committee and help me develop my research in the muscle repair project. I would also like to thank Nano3, Microscopy Core Services and Nanoengineering Materials Research Center for their expertise and successful management of the equipment. Last but not the least, I would like to thank Nanoengineering and Materials Science and Engineering program at UCSD, their administrative staff, Katie and Dana and many of other fantastic staff, for giving me the most memorial, inspiring time of my life.

Most importantly, I would like to thank my wife for teaching me about the drug delivery mechanism and other related knowledge. She has helped me shaped my research and life. Her dedication and diligence has always been of great inspiration to me. With her help, I have learnt the beauty of patience and decision making. We went through this journey together, through up and downs, tear and joys. They are all memorable moments which we learnt to grow up together. Memories shape who we are now, especially the ones that also served as lessons in building our characters. I still remember in the early days when we became together, I was helping her with the DMA machine in the NE-MRC. I was very confident about my work, however, her critical thinking came in to correct some of the missing points that I was not paying attention. I was not very comfortable at the moments but soon realized that it was my blessing to have her looking at my work, otherwise things could go very wrongly. We used to joke that before we were together each of us would spend the late nights in labs alone and now we have a companion in the neighboring lab. There will still be hurdles and challenges ahead but we know we are not fighting alone.

Chapter 1 is a review on biomaterials, particularly polyurethanes, used in 3D printing with focus on different printing techniques and various biomedical applicsations. Some of the materials used in this chapter under review for publication for a book chapter on "Emerging Technologies for Biofabrication and Biomanufacturing".

Chapter 2, in full, is a reprint of the material as it appears in ACS Applied Materials & Interfaces, 2017, Sang-Hyun Pyo, Pengrui Wang, Henry H. Hwang, Wei Zhu, John Warner and Shaochen Chen. The dissertation author was the co-primary investigator and co-author of this paper.

Chapter 3.1, in full, is a reprint of the material as it appears in Bioprint, 2019, Pengrui Wang, Xin Li, Wei Zhu, Zheng Zhong, Amy Moran, Wenqiu Wang, Kang Zhang and Shaochen Chen. Chapter 3.2, in full, is a reprint of the material as being reviewed for publication.The dissertation author was the primary investigator and the main author of these papers.

Chapter 4, in full, is a reprint of the material as it is being review for publication with Zhaoqiang Song, David Berry, Amy Moran, Wisarut Kiratitanaporn, Jacob Schimelman, Bingjie Sun, Frank He, Brian Xi, Shengqiang Cai and Shaochen Chen as co-authors. The dissertation author was the primary investigator and the co-author of this paper.

VITA

2013	B.Sc. & Eng., Materials Science and Engineering; Minor in Music, University of Michigan, Ann Arbor
2014	M.Sc. & Eng., Materials Science and Engineering, University of Michigan, Ann Arbor
2019	Ph.D., Materials Science and Engineering, University of California San Diego, USA

PUBLICATIONS

1. P. Wang, X. Li,; Z. Zhong, W. Wang, W. Zhu, A. Moran, K.Zhang, S.C. Chen "3D Bioprinting of hydrogels for retina cell culturing" Bioprinting, 2019

2. P. Wang, J.-H. Park, M. Sayed, T.S. Chang, A. Moran, S. C. Chen, S.-H. Pyo, "Sustainable synthesis and characterization of bisphenol A-free polycarbonate from six-membered dicyclic carbonate", Polymer Chemistry, 2018 3. S.-H. Pyo*, P. Wang*, J. Warner, W. Zhu, S.C. Chen, "Continuous Optical 3D Printing of Green Aliphatic Polyurethanes", ACS Applied Materials & Interfaces, Vol. 9(1), 2017

4. X. Ma, C. Yu, P. Wang, W. Xu, X. Wan, C.S.E. Lai, J. Liu,A. Koroleva-Maharajh, S. C. Chen, "Rapid 3D bioprinting of decellularized extracellular matrix with regionally varied mechanical properties and biomimetic microarchitecture", Biomaterials, Vol. 185 2018

5. C. Yu, X. Ma, W. Zhu, P. Wang, K. Miller, J. Stupin, A. Koroleva-Maharajh, A. Hairadedian, S. C. Chen, "Scaningless and continuous 3D bioprinting of human tissues with decellularized extracellular matrix", Biomaterials, Vol. 194 2019

6. D. Pan, Z. Cai, S. Ji, S. Fan, P. Wang, Z. Lao, L. Yang, J. Ni, C. Wang, J. Li, Y. Hu, D. Wu, S. C. Chen, J. Chu, "Microtubes with complex cross-section fabricated by C-shaped Bessel laser beam for mimicking stomata that opens and closes rapidly", ACS Applied Materials & Interfaces, 10 (42) 2018

7. W. Zhu, S.-H. Pyo, P. Wang, S. You, C. Yu, J. Alido, J. Liu, Y. Leong, S. C. Chen, "3D Printing of Bisphenol A-free Polycarbonates" ACS Applied Materials & Interfaces, Vol. 10 (no. 6), 2018

8. W. Zhu, X. Qu, J. Zhu, X. Ma, S. Patel, J. Liu, P. Wang, C. S. Lai, M. Gou, Y. Xu, K. Zhang, S.C. Chen, "Direct 3D bioprinting of prevascularized tissue constructs with complex microarchitecture", Biomaterials, Vol. 124, 2017

9. J. Liu, H. H. Hwang, P. Wang, G. Whang, S.C. Chen, "Direct 3D Printing of Cell-laden Constructs in Microfluidic Architectures", Lab on a Chip, Vol. 16, 2016

10. X. Ma, X. Qu, W. Zhu, Y.-S. Li, S. Yuan, H. Zhang, J. Liu, P. Wang, C. S. Lai, F. Zanella, G.-S. Feng, F. Sheikh, S. Chien, S.C. Chen, "A Deterministically Patterned Biomimetic Human iPSC-derived Hepatic Model via Rapid 3D Bioprinting", Proceedings of the National Academy of Sciences (PNAS), Vol. 113 (no. 8), 2016.

ABSTRACT OF THE DISSERTATION

Modulating Physical and Chemical Properties of Biomaterials in Rapid 3D Printing

by

Pengrui Wang

Doctor of Philosophy in Materials Science and Engineering

University of California San Diego, 2019

Professor Shaochen Chen, Chair

Understanding the physical and chemical properties of biomaterials in rapid 3D printing could pave a way for the construction of complex structures with specific functionalities. Both the material conditions and printing techniques play crucial roles in modulating these properties. This dissertation was dedicated to answering the basic questions about how to engineer and improve the mechanical performance of rapidly

3D printed structure from synthesis and printing process. Three distinct groups of materials, namely plastic, soft hydrogels, and elastomeric polymers were used as case studies to reveal their relationships. Additionally, the toughening mechanism of networks with different mechanical properties was discovered and tested. These results could help future studies in rapid prototyping of medical devices, as well as adapting 3D printing in tissue engineering as a new direction.

Chapter 1

3D Printing Polyurethane for Biomedical Applications

1.1 Background

1.1.1 Chemistry

Polyurethanes(PUs) are a family of polymers with urethane (-NHCOO-) group in the polymer backbone. They are commonly derived from exothermic condensation reactions between nucleophilic di-isocyanate and electrophilic agents such as alcohols and amines in presence of a chain extender, catalyst and/or other additives [1]. Based on the mechanisms, it could be classified by one-stage polymerization, where di-isocyante, oligo-diols and chain extenders are reacted simultaneously, or two-stage reaction where the first two components are reacted and chain extenders are added in a separate reaction, as shown in Fig. 1.1 [2]. Both aromatic and aliphatic isocynates can be used in PU synthesis. Compared to aliphatic iscocynates, aromatic isocynates such as diphenylmethane di-isocynate (MDI) or toluene di-isocynates (TDI), shown in Fig. 1.2 are more widely used in industry owing to their high reactivity and better mechanical properties of the PUs produced. The oligo-diols can be categorized as polyether, polyester and other special polyols such as polycarbonate, polycaprolactone and polybutadienes, as shown in Fig. 1.3 Polyether-based PUs are linear polymers commonly made from polyethers such as polyethylene glycol (PEG) and poly (tetramethylene ether) glycol. They have demonstrated high flexibility and hydrolytic resistance. However, researches have found that they suffered from oxidative and thermal stress, excluding them from standard decontamination process such as autoclave. To improve PUs performance at elevated temperatures, polyester-based PUs were developed. They were commonly synthesized from diols such as

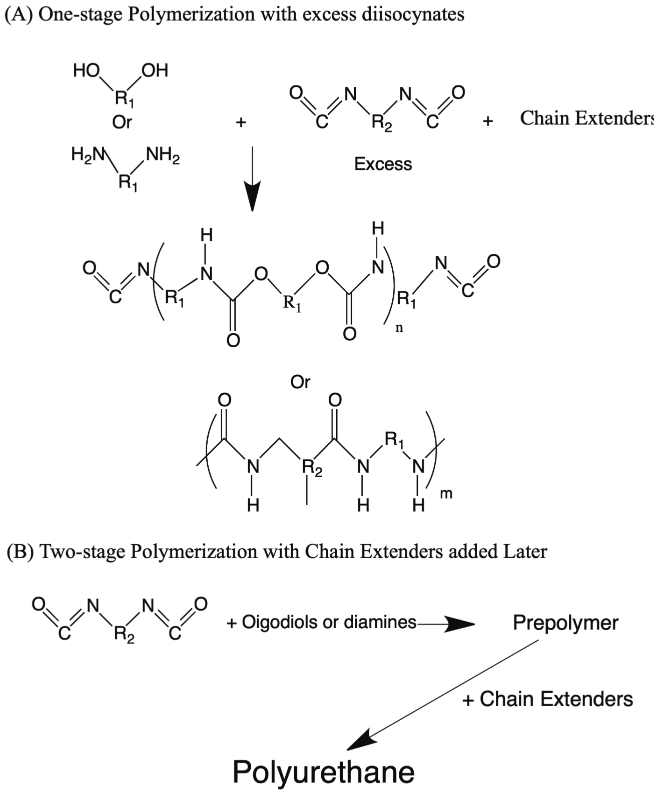

Figure 1.1: Polymerization Mechanism of Polyurethanes

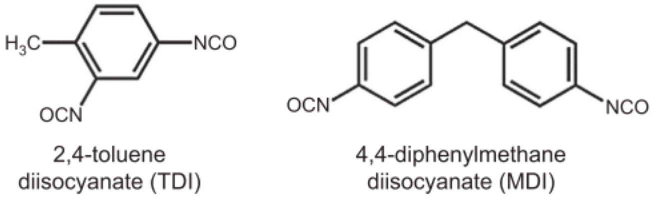

Figure 1.2: Common Di-isocyanates used in Polyurethane Synthesis

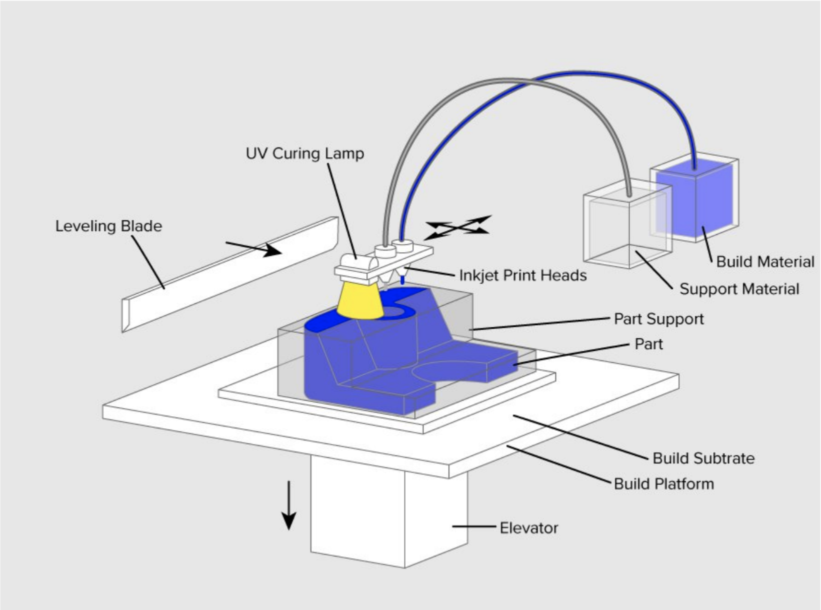

Figure 1.3: Common Oligodiols used in Polyurethane Synthesis

poly(ethylene adipate) diol and poly(butylene adipate) diol. The ester bonds are more stable than ethers at elevated temperatures, resulting in more heat resistant PUs. However, these ester bonds are more prone to hydrolytic degradation, which limited their applications in water contacts such as most of biomedical research. To improve PUs stability in heat and wet conditions, a specially derived PUs, polycarbonate-based PUs were developed. They have demonstrated superior mechanical properties and thermal stabilities. Additionally, they are also more bio-durable and hydrolytic resistant.

The chain extenders and cross-linkers used in synthesizing PUs are generally diols and diamines of lower molecular weight such as ethylene glycol, 1,4-butanediol and cyclohexane di-methanol. They were incorporated into the polymer chains to introduce more cross-linkings and hydrogen bonding to enhance the mechanical

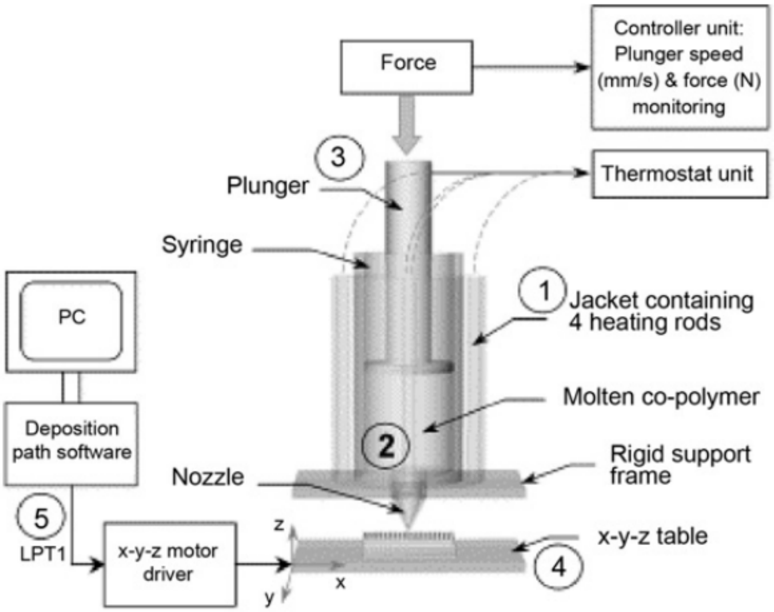

Figure 1.4: Thermoplastic and Thermosetting PUs

properties of the PUs.

Based on the reaction mechanism and polymer backbone structures, PUs can be categorized as thermoplastic or thermosetting, as shown in Fig. 1.4 The main difference is the presence of covalent cross-linking sites on the polymer backbones. Thermoplastic PUs (TpPUs) are linear block polymers synthesized from reagents with di-functional groups such as diols and di-amines without cross-linkers. They typically have low melting point and poor mechanical performance at elevated temperatures. They can be readily dissolved into polar solvent which makes them easily adapted by traditional processing techniques such as solvent casting and fiber spinning. Owing to their mechanical properties, lower glass transition temperature and solubility in polar solvents, TpPUs have also been widely investigated in additive manufacturing such as 3D printing (3DP). Thermoset PUs (TsPUs) are synthesized from reagents with multiple functional groups such as trimethylolpropane and glycerol and/or in the presence of cross-linkers such as excess isocynates. Due to the rigid network structures of TsPUs, they generally have high melting point and do not experience strength reduction at elevated temperatures. Other than these two types of PUs, they can form interpenetrating polymer networks (IPN) with other polymers such as epoxy and acrylates without bulk phase separation. These IPNs have enhanced mechanical performance by combining the advantageous properties of the components. For example, PU/epoxy IPNs have both the flexibility of PU and toughness of epoxy.

One of the most important contributors of PUs mechanical properties is microphase separation within the chemical structures, as shown in Fig. 1.5 [3]. This is due to the complex backbone structures of PUs with hard segments, such as benzenes, and soft segments, such as esters. The hard segment can act as physical cross-linking points whereas the soft segments can rotate freely. In the presence of external forces, the hard segments can retain the integrity of overall structure and the soft segments can absorb the energy and dissipate it as heat.

The development of PUs could be dated back to 1930s where Dr. Otto Bayer and his coworkers at IG Farben AG discovered a new polymer from polymerizing olefins. The early PUs have demonstrated excellent flexibility and strength, which were synthesized as soft foams and flexible fibers. The shortage of rubbery materials during WWII encouraged production of PUs for aircraft coatings and other applications. After the polyisocyanates were commercially available in 1950s, Bayer started to produce flexible PUs using TDI and polyester polyols. Since then, PUs have been

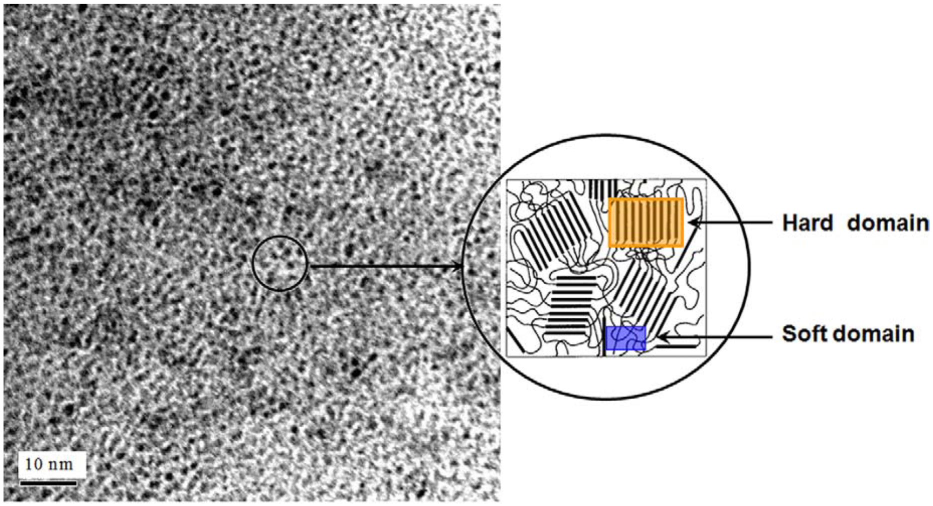

Figure 1.5: TEM showing Microphase Separation of Soft and Hard Segments in PUs

extensively developed into textile, automobile and biomedical applications.

1.1.2 Biomedical Application

Owning to their excellent mechanical properties and biocompatibility, PUs have been extensively investigated for biomedical applications. The early generations of polyester-based PUs have demonstrated superior mechanical properties such as tensile strength, wear and craze resistance. Additionally, they have low immune response *in vivo*, thus were used in making blood pump connectors and breast implants [4]. However, polyester-based PUs are prone to attacks from hydrolytic enzymes, limiting its applications in long-term devices. The reduction in mechanical strength and water resistance at high temperature also prohibits them from standard decontamination process such as autoclave.

Polyether-based PUs were developed for their excellent resistance to hydrolysis as well as elasticity. They were used in neurologic leads, cardiac guidance and pacemaker insulation [5]. Some of the commercially available products such as BioSpan ® from Polymer Technology Group and Pellethane ® from Lubrizol has been widely used in the biomedical field. However, it has been found that polyether-based PUs suffer from stress cracking after implantation due to free radical release from macrophages or foreign giant cell [6–8]. Polyether-based PUs is also prone to enzymic attacks.

To solve the problems faced by both polyester-based and polyether-based PUs, polycarbonate-based and polyolefin-based PUs were developed as the 3rd generation biomedical and biodurable PUs. They have demonstrated better hydrolytic resistance and oxidative stability both *in vitro* and *in vivo.* Two commercially available products, Carbothane ® from Lubrizol and Chronoflex ™ from AdvanSource Biomaterials have been introduced in early 2000s. The current development has been focusing on improving their bio-stability and flexibility, such as enhancing the hydrogen bonding of hard segments and adjusting microphase separation.

1.2 3D Printing of PUs

Three dimensional printing (3DP) is an additive manufacturing process which the object was constructed in a layer-by-layer (LbL) fashion onto a movable platform. During the printing, a fluidic material was introduced then transformed into a solid following guidance from either physical deposition or light patterns for photo-polymerization, depending on the reaction mechanism. Due to the fast processing speed and high degree of customization, 3DP has been widely studied in the biomedical field where time and individuality are crucial [9]. In this section, we will discuss the current progress in adapting different printing techniques on PUs for some biomedical applications.

1.2.1 Thermal inkjet Printing

Thermal inkjet 3DP is a fabrication process by injecting liquid binding solution onto a powder bed [10–14]. The process starts by spreading a layer of fine powder evenly across the stage while the print head selectively deposits binder solutions onto the powder layer. The stage, powder bed and printed parts are then lowered, followed by another deposition process as before until the entire part is fabricated. The unbound powder is then removed by washing. The overall process is illustrated in Fig. 1.6 Thermal inkjet 3DP has been used to print many biodegradable PUs, including PUs from MDI, polycaprolactone diols. Krober *et al.* demonstrated printing of micro-scale dots, lines and pyramids by injecting isophorone di-isocynate and poly (propylene glycol) oligomer. The two inks polymerized in five minutes when injected

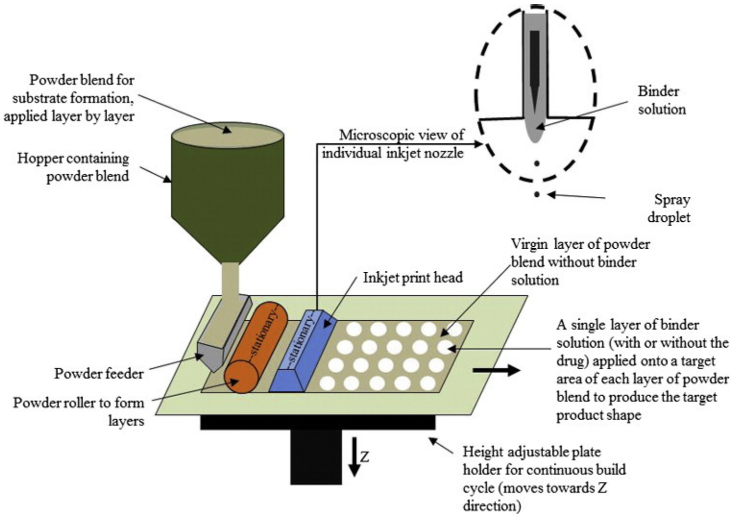

Figure 1.6: Schematic of Thermal Inkjet Printing Process

by two separate nozzles [15]. The addition of fluorescent dyes in only one ink confirmed the homogeneous mixing of both inks on the substrate. Furthermore, Muller *et al.* used different polyols to print structures with gradient local stiffness by varying the stoichiometric ratios of the reagents [16]. The main advantage of thermal inject printing was its relatively low operational cost. However, it lacks precision in droplet directionality. The challenge from nozzle clogging and exposure of ink to thermal and mechanical stress also limited its application in bioprinting [17].

1.2.2 Thermal Extrusion Printing

Thermal extrusion-based 3DP is another LbL process by selective deposition of molten and semi-molten polymer solutions from a movable extrusion print head, as shown in Fig. 1.7 [9, 18–20]. It includes a wide range of techniques such as fused deposition modeling (FDM), fiber deposition, fluid dosing, etc. As one of

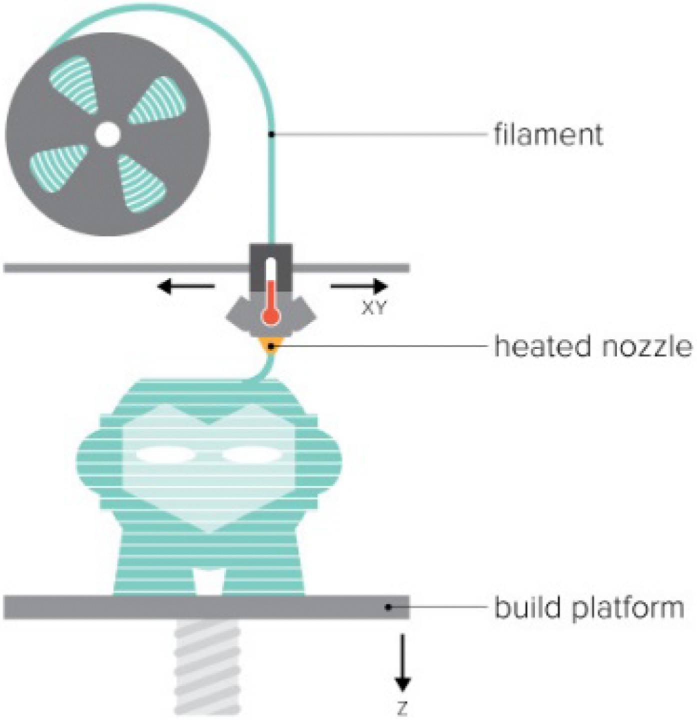

Figure 1.7: Schematic of Thermal Inkjet Printing Process

the most adapted 3DP process, FDM has been used in PU-based biomedical device manufacturing since early 1990s. Chen *et al.* printed a resin composed of PU, poly (lactic acid) (PLA) and graphene oxide via FDM to create a substrate with enhanced mechanical and thermal properties for NIH 3T3 cells to grow on [21]. However, since FDM requires melting of materials before deposition, the heat might induce pyrohydrolysis of polyester segment in biodegradable PUs at elevated temperature and subsequent reduction of tensile strength [22]. Recent development in liquid-frozen FDM (LFDM) overcame the challenge by dissolving PUs into organic solvent to reduce the viscosity, hence improve the ink flowing during the printing process. Xu *et al* reported printing of biodegradable PUs in 1,4-dioxane to fabricate vascular stents. After removing the solvent, the stents retained the excellent mechanical properties and biodegradabilities [23]. The addition of heparin by Yan *et al.* improved the anticoagulation properties of the printed stents [24]. Furthermore, Cui *et al.* and Wang *et al.* used a double nozzle system with two inks from solubilized PUs and type I collagen to print nerve conduits. The printed structure combined excellent mechanical properties from PUs and biological affinity from collagen to promote nerve repair.

LFDM has expanded the material choice of 3DP of biocompatible PUs. However, the toxicity from residual organic solvent still limited their applications in biomedical research such as cell incorporation. This shortcoming has been overcome by the discovery of waterborne biodegradable PUs in FDM. Hsu *et al.* mixed PU nanoparticles consisting diols of PCL and polyethylene butylene with PEO to produce a liquid resin for 3DP [14]. The printed structures demonstrated excellent elasticity and biodegradation. Furthermore, bioactive elements such as growth factors and hydrophilic drugs/antibiotics could be incorporated in waterborne PUs to extend their application in biomedical research [25].

1.2.3 Stereo-lithography 3D Printing

Stereo-lithography (SLA) uses focused light to construct the object from photo-sensitive resins. Unlike inkjet and FDM printing process, the liquid to solid transformation is initiated by exposure of light, typically via activation of photoinitiators and subsequent free radical polymerization. Thus, vinyl groups and derivatives, such as acrylate and methacrylate groups, are required in the resin polymer to be printed by SLA. One of the most commonly used SLA methods is two-photon polymerization by focusing femtosecond laser pulses into a photosensitive polymer resin. Since the probability of electronic excitation of a photoinitiator molecule by simultaneous absorption of two photons is quadratically related to the light intensity, two -photon polymerization can easily achieve nano-meter resolutions in high speed [26]. In the work by Lee *et. al*, a mode-locked Ti:sapphire laser beam with a wavelength of 780 nm and pulse repetition at 80 MHz was used to scan across the focal plane using galvano mirrors. It can construct structures using a voxel matrix scanning method or a contour offset method with resolution of 2.5 nm [27]. In the work by Park *et al.*, acrylated-PU was synthesized and printed by SLA to make phase masks with sub-micron resolution [28]. Additionally, an acrylate aliphatic urethane oligomer was introduced into the resin to tune the elasticity of the printed structures.

Since SLA process does not require thermal energy, it enables rapid fabrication at physiological temperature for biomedical applications. It has been used to print PUs for hearing aids, micro needles for transdermal drug delivery and scaffolds for tissue engineering with or without cells. SLA is also used for dental applications such as surgical guides, crown and bridge replacements. However, some of the toxic photoiniators remained in the final product and are prone to leak out of the structure in their lifespan. Researches has been focused on developing non-toxic photoinitiators and methods to extract out them after fabrication.

1.2.4 Digital Light Processing Based 3D Printing

Digital light processing (DLP) involves regulating light projected onto photopolymer resins to construct an object in a LbL fashion. Unlike conventional SLA methods which uses one laser to "walk-through" the pattern in line-by-line fashion, it projects the pattern by a light modulating unit such as a digital-micro-mirror-device (DMD) [17, 18, 29–31] as shown in Fig. 1.8. For example, the DLP printer developed by Lu *et al.* and Zhang *et al.*, utilized a DMD chip composing approximately one million micro-mirrors to project UV light with optical patterns onto the resin. This dynamic optical projection stereo-lithography (DOPsL) system can print micron-scale features due to the small focal size of the light reflect by each micro-mirror. Additionally, the projection of entire pattern onto the resin eliminates the maneuver time of the nozzles in both inkjet and extrusion based printing and scanning time in SLA technique, hence reduces the overall printing time. Such speed is especially crucial in applications such as direct cell printing and surgical operations. Furthermore, the continuous turnaround of optical patterns with the stage motion

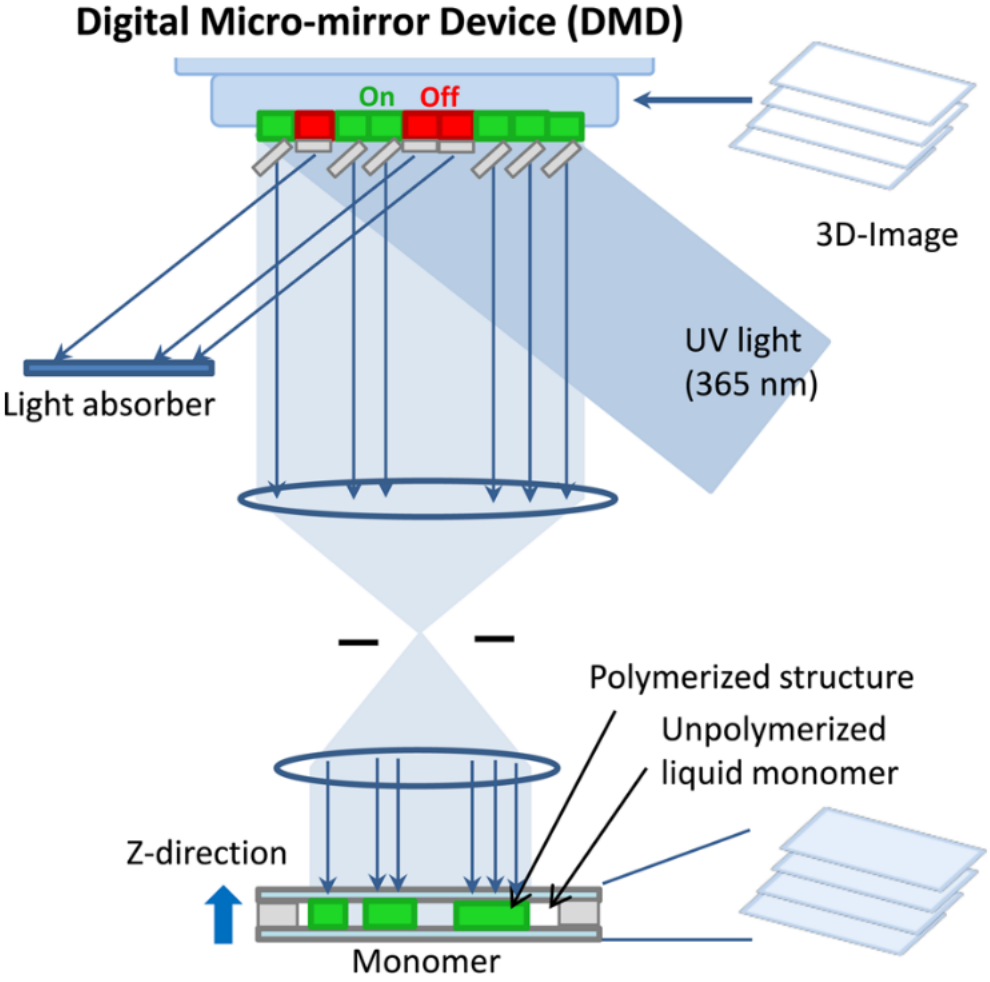

Figure 1.8: Schematic of DLP Printing of PUs

eliminates the artificial interfaces occurred between droplets in inkjet printing or lines in extrusion printing. Owning to these advantages, DOPsL system has been employed to create complex structures such as fractal geometries, domes, artificial micro-fish, vascular network and neuronal conduits [32–38]. Recent development in green chemistry-derived isocynate-free aliphatic PUs was used in the DOPsL system. Pyo *et al.* demonstrated printing of flat surface with stiffness gradient and complex 3D structures with smooth curvatures [17]. The overall fabrication takes less than 1 minute. The photoinitiator used for this printing technique have shown good cell-compatibility and could be washed away by polar solvent such as growth media. Additionally, the similarity between urethane bonds and proteins have promoted cell attachments. Overall this work have demonstrate rapid fabrication of biocompatible PUs with high fidelity and resolution.

1.3 Application

Recent discoveries in PUs have demonstrated their tunable physical, chemical and biological properties. Combining with advancements in 3DP, it is both possible and desirable to expand their application in biomedical and translational applications. The relative recency of such combination makes for relatively few examples of their use in biomedical contexts. Nonetheless, functional examples have been reported. In this section, we will review a number of biomedical applications from PUs by 3DP.

1.3.1 Microfluidics

Microfluidic devices encompass systems that are designed to precisely manipulate small volumes of fluidis and/or quantities of reagents. Conventional microfluidic device fabrication involves photolighography, typically with elastomers like polydimethylsiloxane (PDMS) [39]. However, such conventional process have a number of shortcomings such as protein adsorption and cost of skilled manual labor [40, 41]. In this context, PUs could solve these drawbacks by providing better material properties and enabling greater design flexibility. Additionally, 3d printed PUs allow for direct incorporation of multiple materials to further improve the functionalities of the printed structure.

1.3.2 Soft Robotics

Soft robotics robotics are automated machines made by intrinsically soft material, such as fluids, gel, and elastomers [42]. Conventionally, they are fabricated by casting of soft materials, such as PUs, followed by assembling different parts. Direct fabrication of soft robotic by 3DP could reduce the overall processing time hence reduce the costs. Here we will explore several examples of soft robotics made by 3d printed PUs in biomedical applications.

Patel *et al.* developed a family of highly stretchable with aliphatic urethane di-acrylate as crosslinkers to print robotic hands. In this work, some of the printed structures have achieved failure strain as high as 1100% [43]. With these PUs they have demonstrated direct 3DP of a set of pneumatically actuated grippers that are capable of picking up an object. Ful *et al.* utilized a multi-headed extrusion 3D pritiner with light-assisted curing to build a three-legged soft robot from epoxy and polyurethane as structural components. Furthermore, they embedded shape memory alloy wires as actuators. The printed structures have demonstrated locomotion similar to a spider's gait [44]. Similar to this work, Yang *et al.* used a FDM 3D printer to print a polyurethane based shape memory polymer (SMP) and conductive thermoplastic polyurethane (TPU) to make a pneumatically driven gripper with variable stiffness and active position feedback [45]. When current is applied to the TPU component, the resultant heating will soften the SMP, inducing shape change to work as a gripper as shown in Fig. 1.9. By controlling the piezo-resistance behavior of the TPU parts, they could monitor and control the grippers to grasp objects. Components like these could be readily transferred to biomedical applications such as surgical catheters.

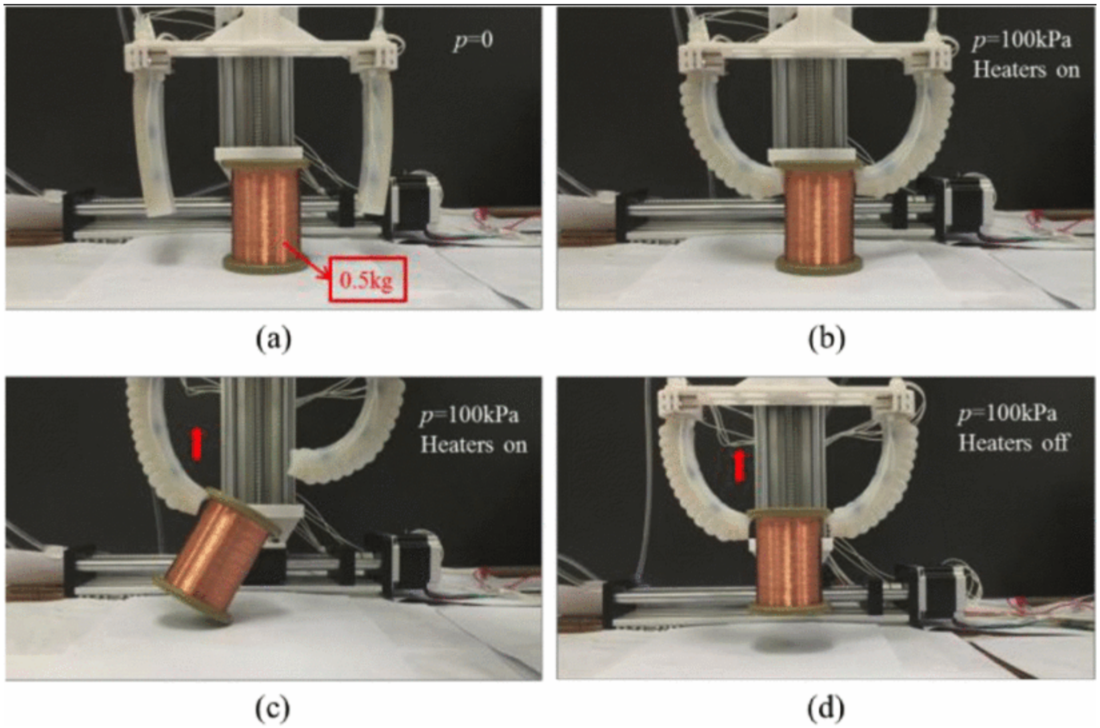

Figure 1.9: Gripping Motion of Soft Robotic Hand Printed by Polyurethane

1.3.3 Tissue Engineering

Tissue engineering and regenerative medicine involved injury repair by tissue scaffolds. The excellent biocompatibility, adjustable biodegradation and versatile mechanical properties of PUs have made them good candidate for such applications [19]. In the work by Whatley *et al.*, a biodegradable and elastic PU was printed by FDM to make intervertebral disk (IVD) scaffolds. The printed structures demonstrated high fidelity and accuracy in replicating the lamellae structures of injury sites at both micro-and macro- scales [46]. The subsequent seeding of neural cells also showed alignment along the concentric lamellae following the topographical cues provided by the printed structures, indicating potential of neural repair. Xu *et al.* used biodegradable PUs dessolved in 1,4-dioxane to make vascular stents via LFDM 3D printing at low operating temperatures [23]. Their results from *in vivo* studies show early vascularization along the stent. In a follow-up work, they mixed heparin in the resin to enhance angiogenesis process. This work has demonstrated the suitable elasticity, anticogagulation and biodegradation of PUs for vascularization work. Furthermore, the inclusion of proteins also show the potential of PUs in applications such as drug delivery and functional scaffolds for tissue repair.

Furthermore, water-based PUs have been used in various cell encapsulation works. Hung *et al.* developed water-based composite with PU nanoparticles and printed by LFDM to make scaffolds for cartilage repair [47]. Compared to PLGA scaffold which were fabricated in the same fashion, the PU nanoparticles improved the elasticity and proliferation of chondrocytes. Another water-based PU bioink developed by Hsieh *et al.* was printed into conduits by LFDM while encapsulating neural stems cells (NSCs). These conduits were implanted into adult zebrafish with traumatic brain injury. After 4 weeks of observation, they have shown significant improvement in recovery of locomotion and survival rates in comparison to the untreated group [48]. Following this study, Lin *et al.* incorporated soy protein isolate into the bioink to further improve the survival and proliferation of NSCs [49]. Similarly, Huang *et al.* introduced water-dispersible graphene and graphene oxides into the bioink to enhance the conductivity of the scaffolds [50]. The printed scaffolds have demonstrated significant improvement in the oxygen metabolism and differentiation of the NSCs encapsulated. In a recent work by Salin *et al.* a personalized left atrial appendage occluder were printed with PU-acrylate resin based on a CT model. The structures were printed with micron size resolutions and smooth surfaces to recapitulate the details of healthy occluder for repair. Moreover, the mechanical properties of the scaffold successfully maintained the stress response of actual part, indicating function repair of damaged tissue in future works.

1.3.4 Surgical Guides and Other Applications

The rapid prototyping of structures based on 3D designs also enabled construction of customized surgical guides for medical operations. Current surgical guides were manufactured in a mass-production fashion, which follow the same design with marginal fitting to the patients. That has became a challenge if they could not perfectly fit into the patient's body during surgery, especially in operations on internal organs such as coronary heart diseases. Due to the nature of the operations, the surgical guide also need to possess adequate mechanical properties to withstand the damages during operations without adversary short-term immune-response. The excellent precision and strength provided by 3DP PUs have been studied for constructing customized surgical guides with high precision and durabilities. Holzapfel *et al.* printed a pelvis based on reconstructed model from CT scanning on a patient with periacetabular tumor. The printed structure closely imitated the modified scanning model. During the operation, the guides were capable to withstand the operation with no adversary effects on the bodies [51].

Other than surgical guides, 3DP PUs have also been used in dental applications such as aligners to correct malocclusion. One of the commercially available products, Invisalign $^{\text{TM}}$ consist a series of computer generated custom aligner molds to mobilize the teeth into proper alignment subsequently. It has generated commercial success since introduction in 1999. The combination of PUs and 3DP can bring in similar products in other biomedical fields in the future.

1.4 Conclusion

The development in PU synthesis and manufacturing has enabled production of materials with better performance and bio-compatibilities. Recent development in 3DP has enabled fabrication of models with high customization and dynamic properties. Using PUs for 3DP has yield some early success for biomedical applications. For example, TPUs and derivatives have been printed as implants for various applications via FDM. The discovery in water-borne PUs further expand the production of elastic and compliant scaffolds with cells. Furthermore, light-based printing technologies such as SLA and DLP have enabled more rapid prototyping with even higher resolutions. Combining the excellent properties of PUs with novel 3DP technologies, we would expect more breakthroughs in fabrication of devices for biomedical applications.

Chapter 2

Continuous 3D Printing of Green Aliphatic Polyurethanes

2.1 Introduction

Replacing hazardous substances and preventing their use are major challenges facing the twenty-first century in terms of human health and environmental impact. Biocompatible and non-toxic materials have played an increasingly prominent role in the manufacturing of biomedical devices and progress of tissue engineering. Additionally, the roles of these materials in promoting tissue formation can potentially open a new frontier in the fast-growing field of regenerative medicine. The advancement of polymer technology continues to create polymeric biomaterials that could fulfill the needs in medical research and clinical operations [52]. Naturally originated polymers such as polysaccharides (alginate, chitosan, starch, cellulose), proteins (collagen, silk, fibroin) and their derivatives are frequently employed due to their biocompatibility [53]. However, natural polymers often do not match well with the physical and mechanical properties of the tissues and organs [54]. Recently, synthetic polymers such as polyethylene glycol, polyvinylalcohol and polyglicolic acid have been widely investigated due to their flexibility and tunability of chemical compositions as well as mechanical properties. Despite of superior control of mechanical properties as compared to natural polymers, most of these polymers still suffer inadequate strength and durability.

As a synthetic polymer, polyurethane (PU) is an attractive candidate for medical device applications due to their excellent mechanical strength, flexibility, hydrophobicity and biocompatibility [55]. In recent years, biomedical PUs have been developed and incorporated in a variety of biomedical devices [54, 56–59]. However, most PUs are produced by a reaction of polyols and isocyanates, which are commonly derived from a reaction of amine with highly toxic phosgene [60, 61]. Other than phosgene, isocyanate itself has been reported as one of the primary causes of occupational asthma worldwide due to its volatility [60, 62]. These toxic residual compounds, although minuscule in amount, are likely to leak from the products during their lifespan of operation [60–64]. Especially, aromatic isocyanates can be converted into aromatic diamines as the residual or degradation products of PUs, which are toxic and potential carcinogenic and mutagenic to humans [61, 64]. To reduce such toxicity, PU networks from an amino acid, lysine-based polyisocyanates was prepared to prevent toxicity of degradation products, and underwent controlled biodegradation to non-cytotoxic decomposition products*in vitro* [55, 65]. However, these materials were still synthesized from polyisocyantes obtained by phosgenation of amine-terminated lysine esters, and the unreacted toxic polyisocyantes could still remain in the polymer materials.

Thus, there has been increasing attention and societal pressure to find an alternative to produce isocyanate-free PUs, and non-toxic alternatives to their existing polymers, especially where toxicity to humans is a concern, such as in medical-, foods- and children products [63, 66, 67]. One way of getting around these toxic raw materials is to produce the polymers by ring-opening polymerization (ROP) of cyclic carbonates with polyamines, which have attracted attention in recent years as an alternative process for the production of PUs through phosgene- and isocyanate-free route [63, 67–69]. Six-membered cyclic carbonates are thermodynamically more suitable precursors for the ROP process [63, 69, 70], especially those with functional groups that can be used to impart different properties to the polymer. We have recently reported the synthesis of six-membered functional cyclic carbonates as a green process [71, 72]. Cyclic carbonates have been used to make scaffolds as biomaterials, but focused on mostly polycarbonate-based materials [73, 74]. Meanwhile, urethane bonds can be formed by ring opening reaction of cyclic carbonates with amines. Especially biogenic aliphatic amines such as putrescine, cadaverine, spermidine and spermine, which are normally formed by the decarboxylation of amino acids as part of the normal metabolism of microorganisms, plants and animals, are considered as harmless alternatives because of their biogenic origin and continuous excretion by the bodyťs metabolisms [75–77].

In terms of applications for 3D printing, there have been attempts to utilize PU as a building material for various research needs. Recently, Park *et al.* used PU-acrylate to fabricate conformal phase masks, which provided the PU elastic modulus of a conformal mold made from a prepolymer, trimethylolpropane ethoxylated (15) triacrylate (TMP(EO)15TA), an acrylate aliphatic urethane oligomer [78]. The bio-printing process of neural stem cell-laden constructs was performed using the thermos-responsive PU hydrogel as the printing ink by a self-designed fused deposition manufacturing platform [79]. However, these methods were a type of stamp lithography and thermal inkjet printing using isocyanate-based oligomer and PU, which lacks resolution and precision. To date, the direct optical 3D-printing of PUs with high resolution has not been reported due to the lack of photo-reactive functional groups in the monomers.

In this study, we report the first-time continuous optical 3D printing using green aliphatic polyurethanes (gPUs). Photo-sensitive diurethane monomers are prepared from six-membered cyclic carbonate functionalized with methacrylate and biogenic amines. The synthesized monomers are then polymerized to isocyanate-free gPU by UV crosslinking using a continuous optical printing (COP) method. 3D structures with user-defined mechanical properties and biologically relevant structures are printed in mere seconds with a high throughput and resolution by COP. The physical properties of gPU structures are characterized on the transparency, stiffness, and thermal behavior. Finally, the biocompatibility of the gPUs was studied by seeding cells on top of the structures.

2.2 Experimental Section

2.2.1 Material Preparation

Monomethacrylated trimethylolpropane cyclic carbonate, and bio-based cadaverine and putresine were kindly provided by Cyclicor AB (Sweden) and CJ Biotech (South Korea), respectively. Spermine and spermidine were purchased from Sigma-Aldrich. All chemicals were used without further treatment. The photoinitiator (lithium phenyl-2,4,6-trimethylbenzoylphosphinate (LAP)) was synthesized according to previous work [80]. Diurethanes functionalized with methacrylate were prepared from reaction of TMPMAC with diamine compounds such as putrescine, cadaverine, spermidine and spermine, respectively. For instance, 1 mmol TMPMAC was mixed, and reacted with 0.5 mmol cadaverine in 1.5 mL vial at 70°C for 10 min without catalyst and solvent. An ethanol and deionized water solution of 3:1 (v/v) ratio was prepared and dissolved the photoinitiator (LAP) to make a photoinitiator solution of

2% (w/v).

2.2.2 Polymerization and 3D-Printing

The resulting diurethane monomers were dissolved in 1:3 ratio into the photoinitiator solution for polymerization. The 3D gradient and functional patterns were designed in Adobe Photoshop and converted into grey-scale images. The gradient pattern was then processed through in-house software into an assembly of 10 strip patterns adjacent to each other. The UV exposure duration of each strip pattern was increased from one end to the other, following the grey-scale intensity of each stripe across the pattern. The diurethane solution was injected into a PDMS compartment covered by a glass coverslip, which was chemically modified by 3-(trimethoxysilyl)-propyl methacrylate. The gradient structure was fabricated by continuously sending the images of strip pattern to the DMD chip as virtual optical masks to be projected onto the monomer solution. The 3D structure was fabricated following a similar continuous process while changing the projection position within the compartment. The fabricated structure was then washed with 70% ethanol solution to remove the unreacted monomers.

2.2.3 FT-IR Characterization

The reactions of thermal ring opening with polyamines and subsequent photopolymerization were monitored based on transformation of functional groups such as hydroxyl, carbonyl, and alkene by FT-IR. The spectra of samples were obtained in region of 500-4000 cm^{-1} using a Spectrum Two spectrometer (Perkin Elmer). An air

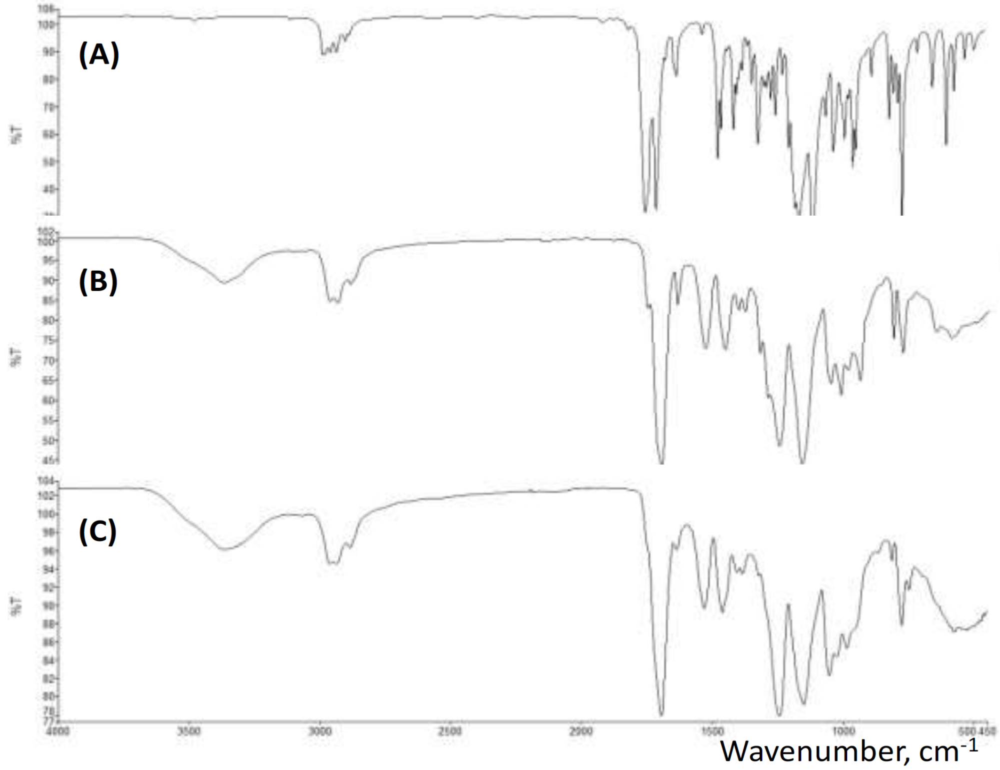

Figure 2.1: FT-IR spectrum for the preparation process of isocyanate-free polyurethane (gPU-1).(A) TMPMAC. (B) Diurethane prepared from TMPMAC and putrescine by thermal reaction. (C)Polyurethane (gPU-1) crosslinked on methacrylate from diurethane by UV-induced polymerization for 30 seconds.

background spectrum was collected before the analysis of the sample, and subtracted from each sample spectrum. The FT-IR spectrum of gPU-1, gPU-2 and gPU-3 are shown in Figure 2.1,2.2 and 2.3.

DSC Characterization

Differential scanning calorimeter (DSC) was then carried out using a DSC Q20 (TA Instrument) DSC12E over a temperature range of -10 200 °C with increasing 10

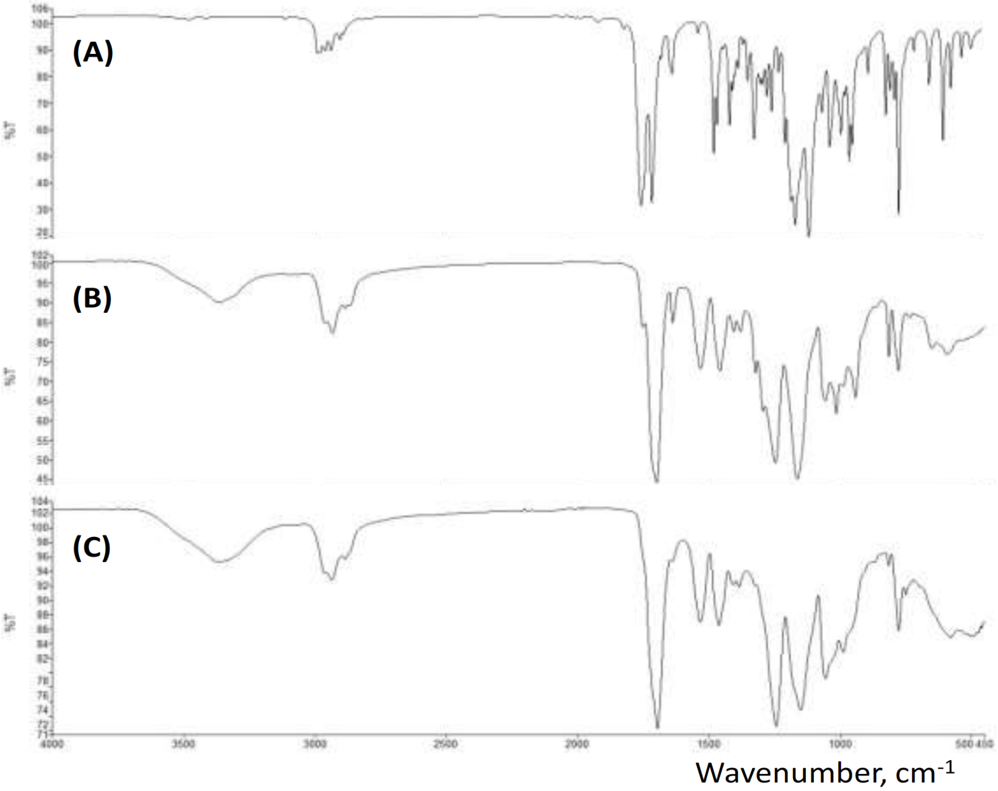

Figure 2.2: FT-IR spectrum for the preparation process of isocyanate-free polyurethane (gPU-2).(A) TMPMAC. (B) Diurethane prepared from TMPMAC and cadaverine by thermal reaction. (C)Polyurethane (gPU-2) crosslinked on methacrylate from diurethane by UV-induced polymerization for 30 seconds.

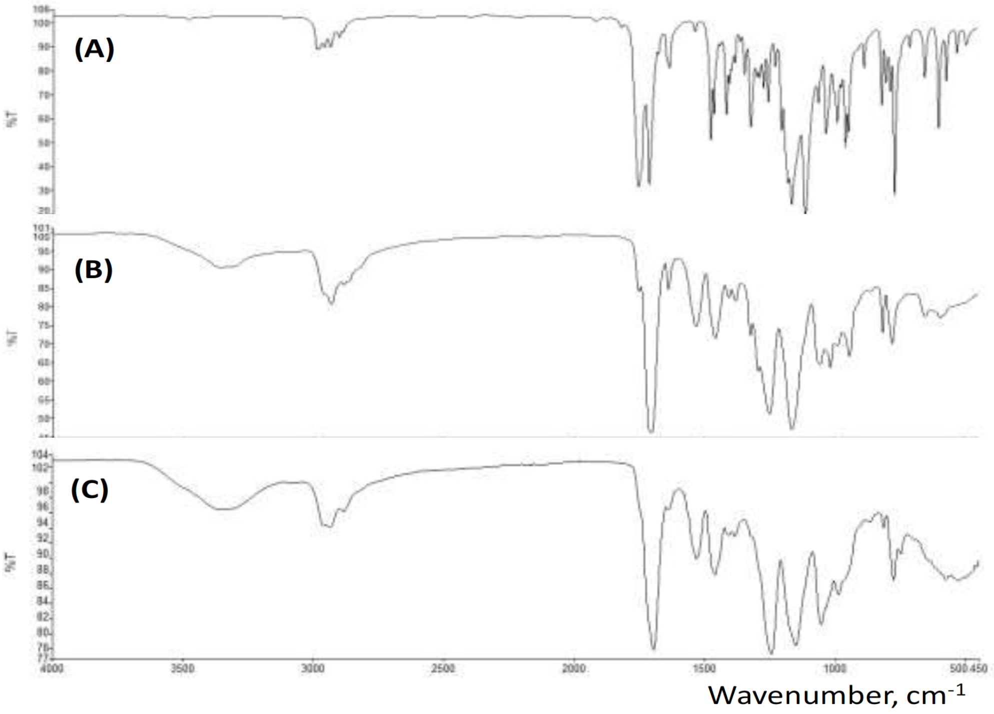

Figure 2.3: FT-IR spectrum for the preparation process of isocyanate-free polyurethane (gPU-3).(A) TMPMAC. (B) Diurethane prepared from TMPMAC and spermidine by thermal reaction. (C)Polyurethane (gPU-2) crosslinked on methacrylate from diurethane by UV-induced polymerization for 30 seconds.

°C /min under nitrogen.

2.2.4 UV-Vis Characterization

Optical absorbance was measured from 350 nm to 1000 nm using a UV-Vis spectrophotometer (Infinite ő 200 Pro, Tecan, Männedorf, Schweiz). To prepare gPU samples, diurethane solutions were prepared from reaction of TMPMAC with diamine compounds such as putrescine, cadaverine, spermidine and spermine, respectively, according to above preparation methods. Resulting solutions were placed in a PDMS compartment, and covered with another PDMS compartment. The height between the two plats was held constant at 500 μm. The gPU structures were then prepared by UV polymerization using a portable UV lamp at 350 nm. Resulting gPU scaffolds were placed in a 48-well polystyrene plate, and analysed by UV-Vis spectrophotometer. Blank was used as a control.

2.2.5 Stiffness Characterization

The stiffness of the PU samples was measured by atomic force microscopy (AFM; Dimension Icon, Bruker) as described previously [81]. Briefly, a cone shaped probe, 0.12 N m^{-1} spring constant with a half angle of 35 (DNP-S, Vecco) was used to indent every strip of the substrates with a gradient of stiffness. The indentation velocity of the probe was fixed at 2 μ m/s, with a trigger force of 2 nN. The force volume maps were determined by Sneddon model with a Poisson ratio of 0.5 [82]. High-resolution scanning electron microscopy (SEM) images were obtained using Philips XL30 ESEM. The surface of the structure was coated by a thin layer of iridium by Emitech K575X Sputter Coater prior to imaging.

2.2.6 Cell Culture

C3H/10T1/2 cells (mouse fibroblast cell line) were maintained in Dulbeccos Modified Eagle Medium (DMEM, Gibco Life Technologies)) supplemented with 10% v/v FBS (fetal bovine serum, Life Technologies,), 1 % penicillin/streptomycin solution (Penstrep) (Gibco Life Technologies).

2.2.7 Cell Viability Assay

10T1/2 cells were obtained at passage 4, used at passage 5-8. The gPUs were printed into round shapes with a diameter of 2.5 mm and was put into a 24-well culture plate, immersed in PBS with 1% Penstrep two days prior to seeding. The cells were seeded onto the gPUs with a density of 100k cells in 1 mL growth media per well. After 3 days and 7 days of culturing, the samples were washed thoroughly with PBS and a solution of calcein AM and ethidium homodimer-1 (EthD-1) (Biotium) in PBS was added to the sample according to the manufacturers protocol. The samples were incubated 30 minutes at room temperature on an orbital shaker and cell viability was assessed by fluorescence microscopy. Cells seeded on the gPUs were scanned and the cells were counted using ImageJ.

2.3 Results and Discussion

2.3.1 Preparation and fabrication of biocompatible green aliphatic polyurethanes

The gPUs were prepared from a cyclic carbonate, tri-methylolpropane methacrylate carbonate (TMPMAC), and polyamines. The overall reaction consists of: A) thermal formation of diurethane monomers and B) UV-induced cross-linking polymerization (Fig 2.4). The cyclic carbonate reacted with biogenic polyamines to produce functional diurethane monomers by ROP reaction. The resulting functionalized diurethanes, which are unique monomers and linkers, were polymerized by free radical polymerization of the methacrylate group to form corresponding cross-linked gPUs. These reactions were accomplished by only heating and light as a green process under mild condition without using isocyanate and phosgene, as shown in Scheme 1. Four different polyamines - putrescine and cadaverine (diamine), spermidine (triamine) and spermine (tetra amine) were chosen to investigate the effects of differences in chemical structure on the properties of the resulting PUs, which were referred as gPU-1, 2, 3 and 4 respectively. The polyamines differ in their linear backbone structure such as chain length and number of amine groups in the molecules. These materials are normally formed by the decarboxylation of amino acids as part of the normal metabolism of microorganisms, plants and animals. They are also present in a wide range of foods, including dairy products, and fermented foods, and can accumulate in high concentrations (e.g. $>$ 1000 mg per kilogram of cheese) [75–77]. In the second step, the resulting functionalized diurethane monomers were further polymerized by free radical polymerization of the methacrylate group to form corresponding cross-linked PUs by 3D printing.

The reactants, products and reactions between cyclic carbonates and polyamines were monitored by the transformation of functional groups using Fourier transform infrared spectroscopy (FT-IR) (Fig 2.5). In the first step of producing functional diurethane from the ROP process, a peak at 1752 cm^{-1} of carbonyl group disappeared and merged with a carbonyl peak (1713 cm^{-1}) of methacrylate group, while a new broad peak is attributed to new hydroxyl group (3000-3500 cm^{-1}) resulted by ring opening (Fig. 1C). This reaction was quantitatively carried out and completed without solvent and catalyst in 10 min. During the second step where functional diurethane monomers are polymerized by free radical polymerization, a peak at 942 cm^{-1}, which is C-H bond of mono-substituted alkene in methacrylate group (Fig 2.5 C), disappeared as new C-C bond formation by UV polymerization (Fig 2.5 D). This process provides a novel, facile, and more environmentally friendly approach for synthesis of aliphatic PUs without using hazard raw materials.

2.3.2 Optical and thermal properties of photopolymerized biogenic green aliphatic polyurethanes

Optical properties and transparency of resulting 4 gPUs were characterized by UV-Vis spectrometer (Fig 2.6 A). Within the range of measurement (350 nm to 1000 nm), the absorbance of all 4 compositions stays below 26% compared with control (blank). The absorbance of gPU-1 is slightly higher than that of the other three gPUs. Rapid drop of absorbance is observed at longer wavelengths (below 5%

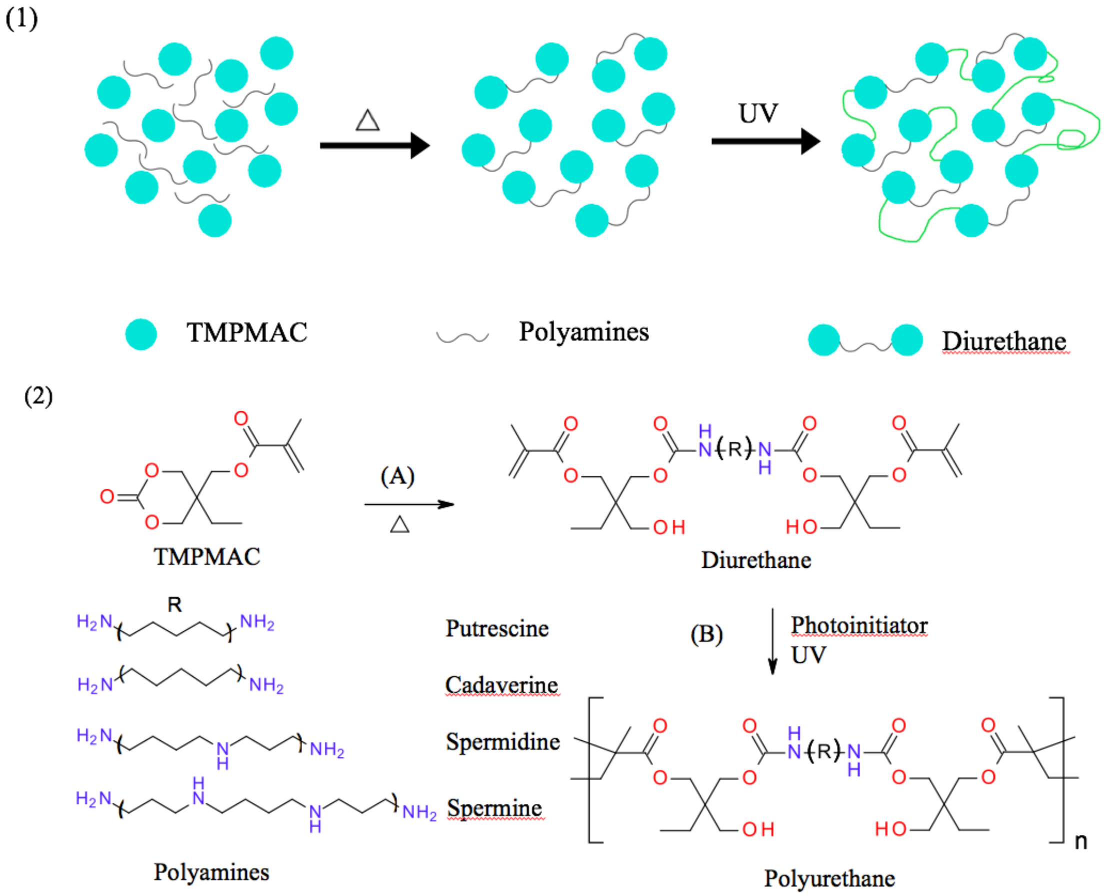

Figure 2.4: Schematic view of Green Chemistry and Optical Printing Process and Synthesis Pathway of Reactions (A) Thermal ring-opening reaction of TMPMAC with biogenic polyamines to diurethane monomers functionalized with methacrylate. (B) UV- induced polymerization of the diurethane monomers on the methacrylate group to polyurethanes.

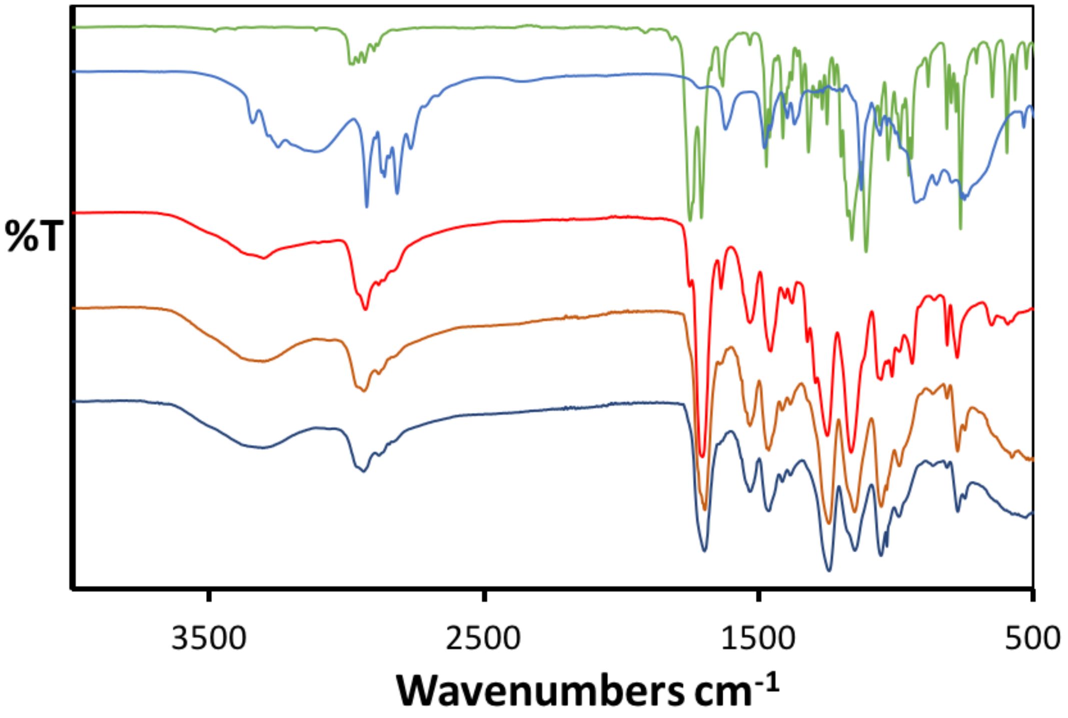

Figure 2.5: Representative FT-IR spectrum for polyurethanes with different preparation processes: (A) TMPMAC, (B) spermine, (C) diurethane prepared from TMPMAC and spermine by thermal reaction, (D) polyurethane cross-linked on methacrylate from diurethane by UV curing for 20 s, and (E) polyurethane cross-linked on methacrylate from diurethane by UV curing for 30 s.

from 550 nm to 1000 nm) for all gPUs. The result indicates that all four gPUs show good optical transparency. The absorbance for gPU-1,2 and 3 reached below 10% , while gPU-1 was about 20% at 365 nm, which is the wavelength of the UV light for 3D printing. Low absorbance at this wavelength will ensure the excitation of the photoinitiator used. The high transparency and low absorbance of gPU materials indicated that these biogenic gPUs could be directly printed into complex shapes using stereolithography based 3D printing system without optical hindrance of already printed structures blocking the optical pathways.

To further study the internal structure and thermal properties of our gPUs, the printed structures were analyzed by DSC to evaluate their crystallinity and glass transition temperature (Tg). The lack of any abrupt changes in energy flow in both heating and cooling conditions demonstrates the gPUs lack of crystallinity (Fig 2.6 B) . Additionally, DSC also showed that the gPUs did not undergo thermal decomposition or oxidation even at temperatures as high as 200 řC. This thermal stability at high temperatures allows gPU to undergo autoclave sterilization, which is a commonly used technique for prepping bio-medical implants and other in vivo interactions. Future work will include other thermal property characterizations, such as thermal expansion and thermal transition coefficient.

To demonstrate the printability of the gPU materials, the COP 3D printing system (Fig 2.7) employs a digital micro-mirror array device (DMD) and projection optics to project patterned UV light onto the diurethane monomer. Via a computer interface coupled with in-house developed software, those optical patterns are automatically and continuously loaded one-by-one onto the DMD chip. Areas illuminated

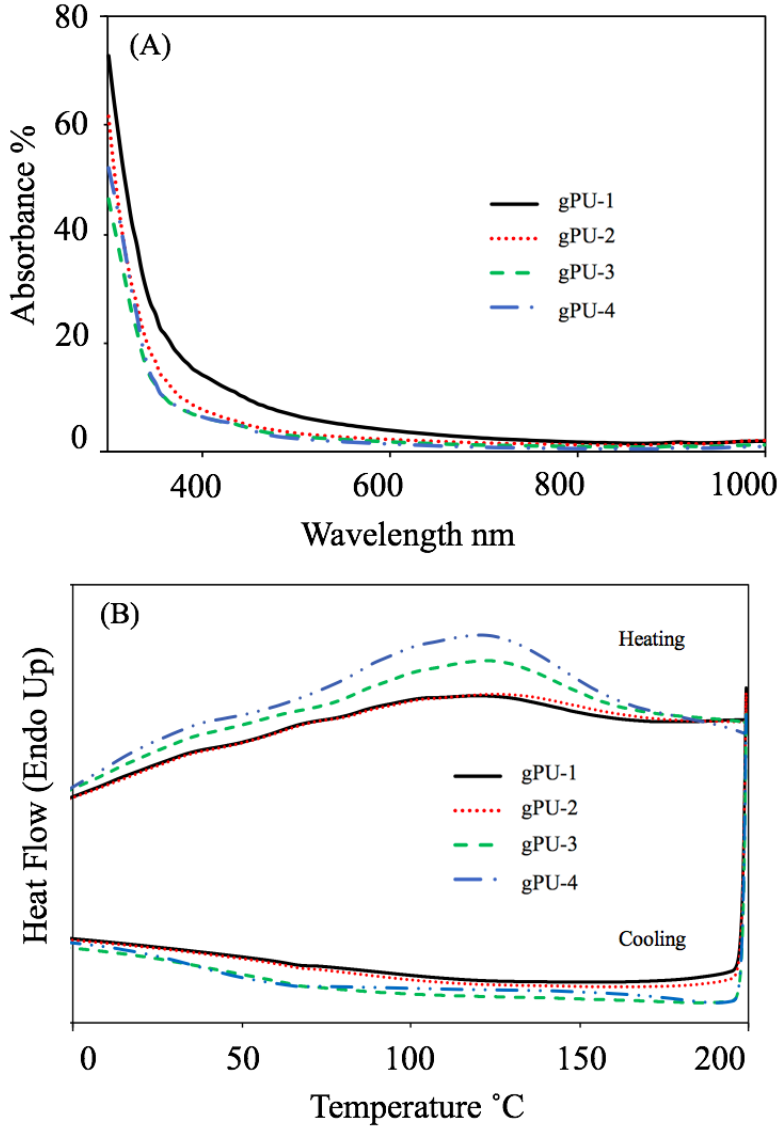

Figure 2.6: (A) Optical transparency of resulting polyurethanes measured by a UVvis spectrophotometer, and (B) thermal properties measured by DSC. Polyurethanes prepared from TMPMAC and putrescine (gPU-1), cadaverine (gPU-2), spermidine (gPU-3), and spermine (gPU-4).

by UV light crosslink immediately, while leaving the dark regions uncrosslinked, forming an image in a specific polymerization plane. This process is dynamically repeated through a series of user-defined digital masks while the stage is translated to construct the 3D device precisely. Since this platform prints the 2D images without scanning in both x and y directions, and creates the 3D object continuously in the Z direction, the printing speed of COP is much faster than a traditional nozzle-based 3D printer. Due to the continuous movement of the stage the fabricated 3D structures do not exhibit the planar artifacts (interfaces) induced by traditional layer-by-layer fabrication approaches that involve discrete movement of the linear stage to a new height position. These existing 3D printing approaches produce structures with step-like artifacts along the Z direction due to the drop-by-drop and layer-by-layer fabrication process. The scanning-less and continuous nature of the COP platform will not yield such artificial interfaces and therefore will produce a whole 3D structure with a smooth contour, significantly improving the structural integrity of the printed structure. This printing platform could not only create complex polymer scaffolds, but also cell-laden constructs [81, 83–85] for both *in vitro* and *in vivo* applications such as early drug screening, tissue regeneration and wound healing. Previous work has demonstrated the speed, precision and versatility of similar fabrication processes on other biomaterials such as poly(ethylene glycol) di-acrylate (PEGDA) and gelatin methacrylate (GelMa) [30, 31, 53]. However, these biomaterials do not have the high durability and stiffness for applications such as lab-on-a-chip devices and medical implants. Combining the 3D printing system with the newly developed gPU, we could potentially solve these challenges. The thermal behavior of gPUs with different polyamines was measured by repeated DSC cycles, and showed similar behavior, which was almost featureless within experimental temperature range due to crosslinking of the methacrylate group upon UV polymerization (Fig 2.4).

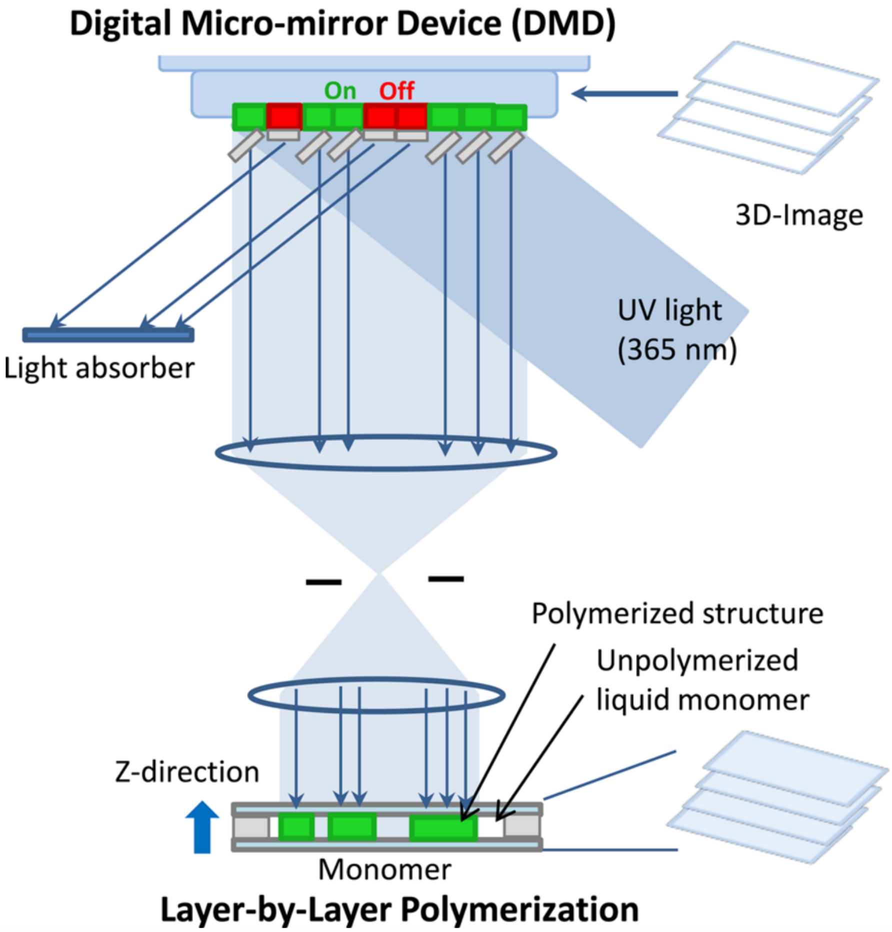

Figure 2.7: Schematic of the Continuous Optical Printing (COP) System. UV light (365 nm) illuminates the DMD system, which generates an optical pattern according to the 3D image flow from the control computer. A 3D scaffold is printed in a layer-by-layer fashion onto the photocurable monomer by the optical pattern projected through an optical lens.

2.3.3 Tunable mechanical properties of gPU via printing

The relation between the printing parameters, such as exposure time, and surface stiffness of printed structures was investigated. Surface stiffness plays an important role in biomedical research [86]. To investigate how to tune the mechanical property of printed structure, we used the equation developed by Askadskii *et al.* to describe the elastic modulus of polymer and its number of repeating units by the following equation [87, 88]:

$$E_n = \frac{3dRT\left(m+\beta\right)}{M_0 m^2}$$

Where d is the polymer density; R is the universal gas constant; T is the temperature for which the modulus was calculated; M_0 is the molecular mass of the repeat unit of the linear network fragment; m is the number of the repeat units in a linear fragment between neighboring crosslinks; SS is the ratio between van der Waals volume of the crosslink over that of the repeated unit. In the case of linear polymerization, SS equals to zero.

Previously Decker *et. al.* has computed the relation between the kinetic chain length during polymerization and UV exposure time. Briefly, the kinetic chain length (KCL) was then calculated by dividing the rate of polymerization by the rate of initiation, which is a function of both the monomer concentration and the quantum yield. The quantum yield of the polymerization is essentially a function of the exposure time, as shown in the following equation [88].

Rate of polymerization $R_p = \frac{k_p}{(2k_t)^{0.5}} \left[M\right] r_i^{0.5}$

Rate of initiation $r_i = \Phi_i \cdot I_a$

Kinetic chain length $KCL = \frac{R_p}{r_i} = \frac{k_p[M]\Phi_i^{0.5}}{(2k_t)^{0.5} I_a^{0.5}}$

Quantum yield $\Phi_i = \frac{[M] \times l}{f \times 1000 \times t_e \times I_a}$

Where $[M]$ is the concentration of urethane monomer; k_p is propagation rate; k_t is termination rate; I_a is the light intensity absorbed; l is the thickness of the printed structure; f is the fraction on incident light absorbed by the sample; t_e is the exposure time. The number of repeat units in a linear fragment between neighboring crosslinks is a linear function of kinetic chain length of the polymerization. Therefore, two equations could be combined to yield the following equation:

$$E_n = A \cdot \frac{d\,(2k_t)^{0.5}\, t_e^{0.5}}{M_0 k_p\,[M]^{1.5}}$$

For polyurethane made by the same reactants, the polymer density, molecular weight of the repeating unit, the reaction kinetics and the monomer concentration are the same. The equation could be further reduced into a square root function of exposure time. Based on the equation, we predicted that the stiffness of the printed structure increases with the raise of exposure time. To prove this relation, we printed a structure using the COP system (Fig 2.7). The structure is made up by a series of stripes with increasing exposure time, as shown in Fig 2.8 A. Here, a shape with increasing greyscale intensity was first designed in Adobe Photoshop. This image file was further processed by an in-house software to divide it into 10 strip patterns according to grey scale intensities as shown in Fig 2.8 B. Each strip pattern was associated with a specific exposure time, running from 12 seconds to 30 seconds with increment of 2 seconds per strip. During the printing, the entire block was initially projected onto the monomer solution, followed by disappearance of strip pattern from one end to another until all disappeared (Fig 2.8 A). A structure with increasing exposure time was obtained and imaged by SEM (Fig 2.8 C). The stiffness of each strip was measured by atomic force microscopy (AFM) after soaking in ethanol and then air-dried for testing. The results, as shown in Fig 2.8 D follow a square root function of the exposure times, as expected. The structures and the number of amine in the polyamine linkers also affect the stiffness of the polymer created as indicated by the AFM data. Between gPU-1 and gPU-2, which were prepared from diamines of straight 4-carbones (putrescine) and 5-carbones (cadaverine), respectively, the higher stiffness gPU was prepared from shorter compounds due to the lower chain flexibility. However, gPU-3 and gPU-4 prepared from tri-amine (spermidine) and tetra-amine (spermine) having longer chain length provided higher stiffness, and this behavior could be explained by partial participation of secondary amines inside the chain in the formation of diurethane. Additionally, since the decreasing number of repeating units between crosslinks has a higher impact on the resultant elasticity, it can compensate the increase of molecular weight of the monomer. The stiffness was tunable by controlling the exposure time and selecting different polyamine compounds. These tunable and gradient patterns can be used for the study of cell motion and differentiation.

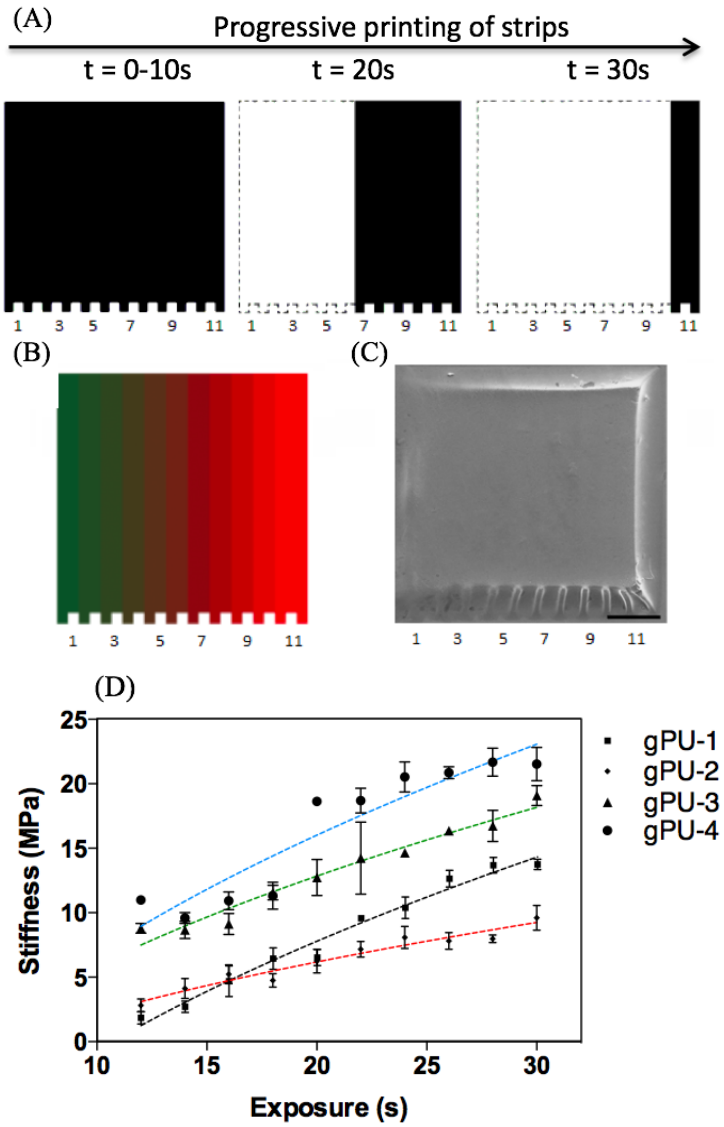

Figure 2.8: Optical printing of gradient pattern using gPUs by the COP system. (A) Progressive printing of strips based on the program of exposure time. (B) Designed pattern for gradient printing. (C) SEM image of printed pattern (scale bar 500 μm). (D) Stiffness of printed scaffolds prepared from different gPUs

2.3.4 Structures featuring curves and complex contours by 3D-printing

Curves and complex contours on the surface are essential in 3D printing of biology relevant and intrinsic structures. To demonstrate rapid 3D printing with the gPUs using the COP system, a complex gradient design was created and processed into a series of transverse planes according to the greyscale of each pixel, as shown in Fig 2.9 A. These planes were projected onto the monomer solution. During the printing process, the stage constantly changes in the z-direction to position the focal plane at different locations within the monomer solution (Fig 2.9 B and C). Only the monomer exposed at the focal plane will be polymerized to form the patterns as projected. When the stage moves to a slightly higher location, a different pattern is formed and is chemically reacted with the pattern at the previous location. Hence a structure with complex surface contour could be fabricated through a series of planetary patterns stacking on top of each other. Fig 2.9 D and E demonstrated a complex structure which resembled the surface outline of a sharkskin. The sharkskin has unique properties for hydrodynamics, antifouling and repelling of bacteria [89]. However, fabricating such biomimetic architecture has been challenging. We demonstrated that the convoluted sharkskin structure with smooth surface contour could be printed by the COP system, and a biomimetic double-bump surface pattern was generated within 30 seconds.

Furthermore, other structures such as logpile, gear, bone and squid were 3D-printed using gPU (Fig 2.9 G, H and I), which are well known for their applications in soft robotics, microfluidics and biomedical researches [89]. The superior mechanical

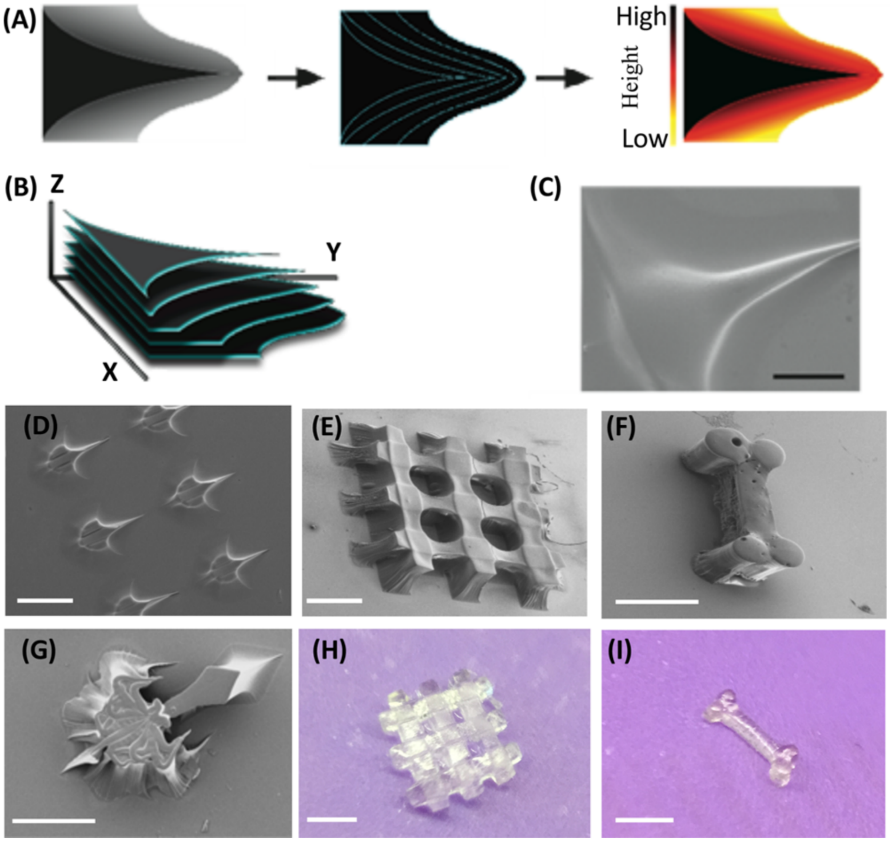

Figure 2.9: Optical printing of intricate structures using gPUs by the COP system. (A) Schematic process showing software-aided 3D reconstruction from grayscale patterns. (B) Layer-by-layer printing procedure of 3D structure guided by computer. (C) SEM image of printed pattern (gPU-4). (D)

and optical properties make the gPUs an excellent material for printing structures with high fidelity and complexity. The printed structure and smooth curves as shown in the SEM images have demonstrated the printability of the materials and process with high resolution within seconds.

2.3.5 Biocompatibility of gPU materials

As a green chemistry process with replacing hazardous ingredients, the overall reaction does not include any cytotoxic materials and the product is potentially toxic-free. Additionally, the similarity between urethane functional groups and amino acids in terms of chemical structures further provokes a question whether this material could be used for coating-free biomaterials. To further explore the potential of using gPU for biomedical research, we investigated the cyto-compatibility of C3H 10T1/2 cells seeded directly on the printed structures (Fig 2.10). This type of fibroblast cell is widely used as a model cell in many biology studies, especially toxicity screening and tissues engineering [90]. The gPU was printed into round shapes with diameters of 2.5 mm and was put into a 24-well culture plate, immersed in PBS with 1% Penicillin Streptomycin two days prior to seeding. The 10T1/2 cells were obtained at passage 4, used at passage 5-8 and maintained in DMEM growth media with 10% FBS. The cells were seeded onto the structures at a density of 100k cells in 1 mL growth media per well. After 3 days and 7 days of incubation, the cell viabilities were measured using calcein AM and ethidium homo-dimer assay according to the manufacturer's instructions. High cell viability (over 95%) for each material was obtained (Fig 2.10). Both the morphology and high viability of the cells suggested that the gPUs are viable choice for biomedical applications.

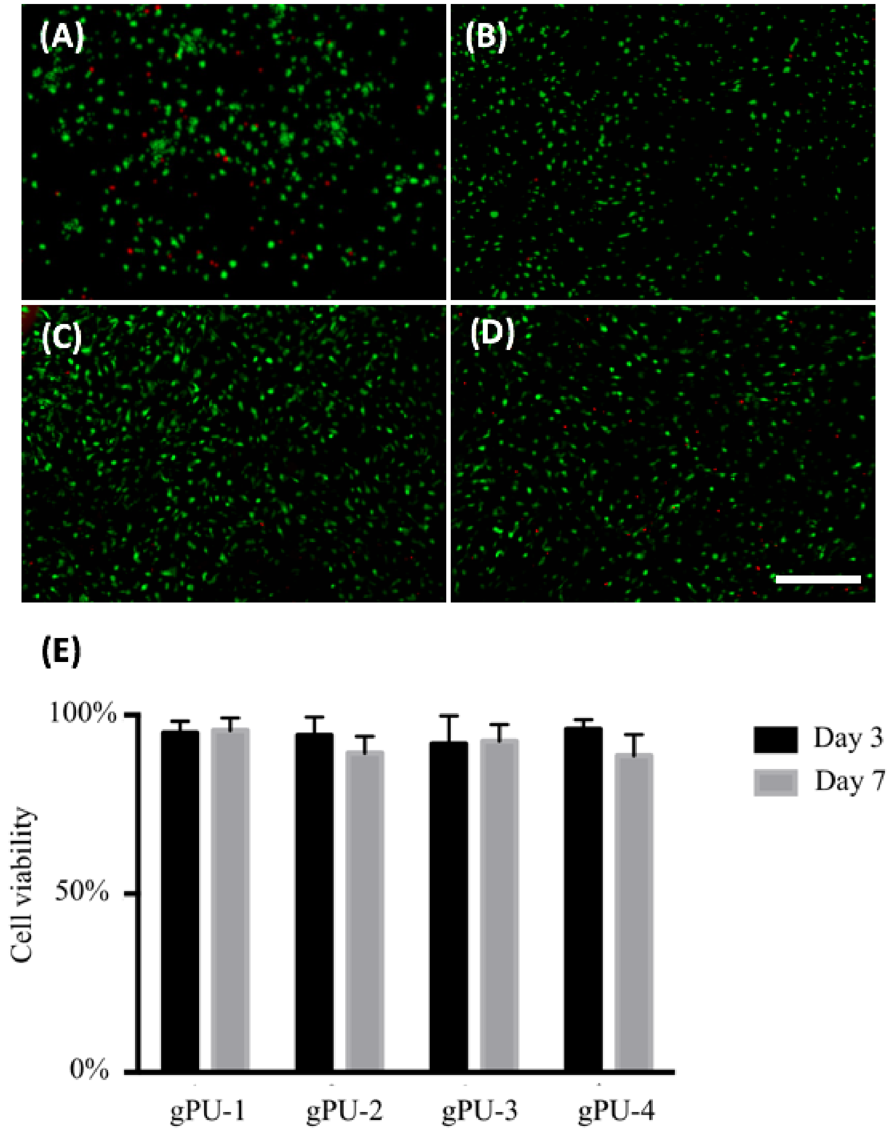

Figure 2.10: Immunostaining to examine cell viability after seeded on (A) gPU-4 at day 3, (B) gPU-4 at day 7, (C) culture plate (control) at day 3, and (D) at day 7. Cells seeded on all 4 gPUs have more than 95% cell viability after 3 and 7 days postseeding. Scale bar = 200 μm.

2.4 Conclusion

In conclusion, continuous optical 3D printing of a novel photopolymerizable isocyanate-free PU was reported for the first time. Rapid printing of smooth gradient and 3D structures has been demonstrated. The mechanical and optical properties of printed materials were characterized. The technology can be used to tailor-make novel gPU materials with specific properties and fabrication process from various functional cyclic carbonates and polyamines. Such printable isocyanate-free gPU materials could fulfill the demands to critical safety issues required in biomedical and consumer products applications. 3D-printed gPU devices could have broader applications such as mechanically strong and durable medical implants, tissue engineering scaffolds, micro-fluidic devices, diagnostic probes, and lab-on-a-chip systems.

2.5 Acknowledgment

S-H. Pyo and P. Wang contributed equally to this work. The work was supported by VINNOVA (The Swedish Agency for Innovation System) and Swedish Research Council Formas to S.-H.P. and grants from the Department of Defense (W81XWH-14-1-0522), California Institute for Regenerative Medicine (RT3-07899) and National Science Foundation (CMMI-1332681 and CMMI-1644967) to S.C. The authors thank Dr. Nathan Gianneschi for providing the AFM for measurements.

Chapter 3

3D Printing Hydrogels for Biomedical Applications

3.1 3D Printing Hydrogels for *In Vitro* Regeneration of Retina

3.1.1 Introduction

The retina is a complex light sensitive tissue that collects light before transmitting the information to brain for realizing the visual environment [91]. In human retinas, cells of specific functions are embedded in extra cellular matrix (ECM) following a multi-layered configuration [92]. These ECMs have specific chemical compositions and physical properties that could affect the functionality of cells residing in them. In human retina, the ECM consists mainly of hyaluronic acid (HA), which is a negatively charged polysaccharide [93]. Photoreceptor cells (PRs), which reside across the intermediate layers of retina, are responsible for light detection. Their degeneration could lead to the onset of blindness in numerous diseases, including retinitis pigmentosa and age-related macular degeneration (AMD) [94]. Regenerating healthy PRs in the eye is a promising strategy to treat these diseases. However, culturing of isolated PRs *in vitro* still remains challenging [95]. Unlike the whole retina, which can be maintained in culture for several days, the PRs undergo morphological changes and profound apoptosis in isolated culturing without the support of ECM and other cell types [96]. The few surviving cells lose their outer segments and downregulate the expression of visual cycle proteins [91]. Therefore, there is a growing need to develop a viable strategy to specifically culture PRs *in vitro* with ECM for biological studies such as drug screening, cell intervention and integration, and disease modeling. Furthermore, the discovery of a suitable ECM material for PRs culturing could help to study their maturation and realizing repair by implantation in the future.

Residing adjacent to the PRs in a similar ECM, retinal pigment epithelium (RPE) is a highly specialized cell with pigmented microvilli [97]. Research has shown the importance of RPE in nutrient transport, growth factor production, and phagocytosis of photoceptors [98]. Although quiescent under physiological condition in the eyes, the RPE cells will start to proliferate in response to traumatic injuries in retina [99]. Previous works have reported sequential development of both RPE and PRs from fetal retinal progenitor cells (fRPCs) [100]. This study has shown that the RPEs assembled a bilayer structure with the neural retina, which matured into PRs at an early stage of development. These findings inspired a strategy to regenerate damaged PRs with the support of RPEs. To realize this strategy, we aim to encapsulate cells with ECMs closely related to native retina and localize individual cell type following the same arrangement as the native retina. Our recent development in 3D bioprinting can construct different tissues through polymerization of cell-containing ECMs [30]. Unlike conventional planar maturation strategies, 3D bioprinting could create mechanical and geometrical cues that closely resemble the cell niche [1,12]. In previous works, we have demonstrated 3D bioprinting of hepatic and vascular system to regenerate functional tissues from embryonic stem cells [30, 101]. The rapid and cell compatible printing process enabled us to create complex 3D structures while maintaining the viability of cells.

Recently, different strategies have been used to develop PRs from human pluripotent stem cells [102]. For example, Lorber *et al.*demonstrated 3D printing of retinal and glial cells as a retina model while Hunt *et al* investigated the effect of stiffness on retinal differentiation [103, 104]. Their results indicated that the differentiation was mostly enhanced in ECMs that mimic the stiffness of the native retina. While these studies have shown the efforts of maturing PRs *in vitro*, recapitulating surrounding environments of the cells such as stiffness and cell hierarchy during differentiation still remain challenging [103]. Mitrousis et al. reported the use of HA in encapsulation of retinal stem cells (RSCs) to improve PR growth [91]. As an abundantly present polysaccharide in the subretinal space, HA is responsible for sequestration and presentation of biomolecules to PRs. It has been reported to facilitate PR maturation by upregulation of the mTOR pathway in RSCs [91]. While native HA does not form a physically stable gel with cells, several chemical modification methods have been reported to functionalize the HA with methacrylation by glycidyl-hydroxyl reaction, resulting in a photopolymerizable hydrogel (HA-GM) that can be 3D printed with our reported printing techniques [105].

In this work, we present a strategy to synthesize HA-GMs with different degrees of methacrylation (DM) by altering molar ratios of initial reagents. Their physical properties such as swelling ratio and compressive modulus are measured and analyzed. Furthermore, we have constructed a multi-layered tissue model using 3D bioprinting to resemble the native retina structure. The fetal retinal progenitor cells (fRPCs) were co-differentiated with RPEs to improve their differentiation.

3.1.2 Experimental

Materials Synthesis

HA-GMs were synthesized following protocols reported previously [30]. Briefly, 1 g of hyaluronic acid (Lifecore Biomedical, MN) was added into 100 ml of 50:50 acetone:water solution. The solution was mixed overnight before adding triethylamine and equal amount of glycidyl methacrylate with a designated molar ratio. The reaction was continued for 24 hours before dialysis over distilled water for 24 hours. The resulting solution was dried by lyophilization (Labconco) over 5 days before rehydrated to make a hydrogel solution. 10 mg of the dried hydrogel was dissolved in 1 mL of deuterium oxide completely and examined by ^{1}H-NMR (ECA 500, JEOL USA).

To improve cell binding of HA-GM, we introduced long chain Arg-Gly-Asp-Ser (RGDS) peptide (American Peptides) into the hydrogel. The polypeptide was synthesized by EDC-NHS synthesis with polyethylene glycol following previously reported protocols [106]. PEG-RGDS was mixed with HA-GM hydrogel in 2 mM/mL concentration [107]. The photoinitiator, lithium phenyl-2,4,6 trimethylbenzoylphophinite (LAP) was synthesized following previously published protocols [30]. Briefly, dimethyl phenylphosphonite was mixed with equal amount of 2,4,6-trimethylbenzoyl chloride overnight. The reaction was conducted over 18 hours under inert gas before heated to 50 °C. Lithium bromide was mixed with 2-butanone and added into the solution slowly over ten minutes before cooled to room temperature over four hours. The precipitates were filtered and washed with 2-butanone before dried by vacuum.

Physical and Mechanical Properties Assessment

To analyze the microstructure of the HA-GMs by scanning electron microscopy (SEM), the printed HA-GM hydrogels were dried over a series of ethanol/water solutions with an increasing ethanol concentration. The hydrogels were further dried by hexamethyldisilazane. After completely removal of any solvents, the samples were sputtered with iridium for 7 seconds and then imaged with SEM (Zeiss Sigma 500). The SEM images were used to evaluate the average pore sizes and interconnections between pores.

To analyze the physical properties such as swelling ratio of the HA-GMs with different degrees of methacrylation (DMs), the hydrogels were printed into cylindrical shape with the same dimensions, exposure duration and light intensity. The samples were then incubated in saline solution at 37 C for 1 day, 3 days and 7 days before being tested. Images were taken to evaluate the swelling ratio of the hydrogels. The porosities of the hydrogels were calculated by swelling factors and polymer volumes. The mechanical properties of HA-GM hydrogels were evaluated by compression test using MicroSquisher (CellScale) at 10% strain and 2 μ m/s strain rates. The instrument collected the force and displacement data, which were further analyzed using an in-house software to calculate the compressive modulus. The diameter and height changes of each hydrogel were measured by a microscope over 7 days to analyze the volumetric swelling ratio of each sample.

RPEs Encapsulation

RPEs were purchased from ATCC and cultured according to manufacturers guide. The RPE cells were cultured to passage 7 before digested to mix with HA-GMs with 500k/mL concentration in the final cell-gel mixture. The mixture was printed and continuously cultured over the course of 10 days. Ethidium homodimer and calcein AM were used to analyze the viability of RPEs encapsulated in different HA-GMs. The viability of RPE cells were calculated as the ratio of number of live cells over total number of cells.

Multilayered Structure Printing

To build a layer-by-layer structure with hydrogel-cell matrix, we developed a rapid 3D printing process to consecutively construct each layer (Fig. 3.1). Briefly, a light source of 365 nm wavelength (Omnicure S2000, Waltham, MA) was used to provide the UV light for photo-polymerization. Structures were designed by Solid Works ő, which were then converted to digital mask patterns and transferred to the digital-mirror array device (DMD) chip by in-house software. The DMD chip was used as an optical mask for projecting patterns onto the solution containing hydrogel, cell, and photoinitiator. Once the light passes through the lenses, it is collimated to form a precise image on the solution, where polymerization occurs to form the structure. The RPEs mixed with HMHA-GM for the first layer was loaded on the reservoir of the stage, which moves in all three directions guided by the computer. After printing of the first pattern, the solution was washed away while the printed structure remained. The RPCs with HMHA-GM for the second layer was then loaded

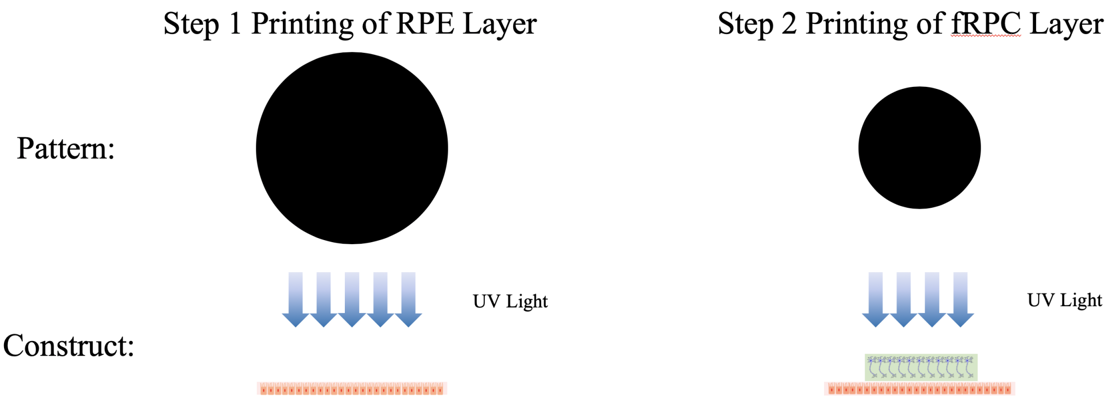

Figure 3.1: Schematic of printing multilayered retina structures

on top of the first layer, followed by lowering the stage. After the second layer is printed, the multi-layer structure was rinsed and put in culture for further analysis.

Co-differentiation of fRPCs

Human fetal retinal progenitor cells (fRPCs) were harvested from 20-24 weeks old fetus and maintained with growth medium (Ultra CULTURE serum-free medium, 10 ng/ml EGF, 20 ng/ml bFGF, 2mM L-Glutamine and 50ug/ml gentamin). The fRPCs were differentiated into PR cells following methods reported in a previous publication [108]. Briefly, after reaching 50% confluency, fRPCs were switched into PR differentiation medium (DMEM/F12: Neurobasal medium 1:1, N2, B27, 0.05% BSA Fraction V; 2 mM Glutamax, 50 nM docosahexaenoic acid and supplemented with 1 μ M IWP2, 10 μ M DAPT, 100 nM purmorphamine, 100 nM retinoic acid, 100 μ M Taurin, 10 ng/ml bFGF) for two weeks. The cells were mixed with HMHA-GM at 500k/mL concentration in the final cell-gel mixture for printing.

3.1.3 Results and Discussions

Methacrylation of HA-GM

The physical properties such as stiffness of the hydrogels is closely related to the degree of crosslinking, which is affected by the number of methacrylate groups attached to the polymer backbone. This number can be quantified as degree of methacrylation (DM), which is calculated by the ratio between the methacrylate groups and remaining methyl groups. By altering the initial molar ratio of the reagents, the ring-opening reaction of the epoxide functional group would occur to different extend, resulting in products of various DMs. Three different molar ratios were used to create low-methacrylated hyaluronic acid (LMHA-GM), medium-methacrylated hyaluronic acid (MMHA-GM) and high-methacrylated hyaluronic acid (HMHA-GM). The hydrogels were examined by ^{1}H-NMR to evaluate their DMs, as shown in Fig. 3.2. The presence of the methacrylate group peaks at 5.6 and 6.0 ppm confirmed the methacrylation, as compared to hyaluronic acid in Supplement Figure 1 d. The DMs were calculated by dividing the integration of peaks from the methacrylate group over that of the remaining methyl groups in hyaluronic acid at 1.7, 1.8 and 1.9 ppm [105]. The results are shown in Table 3.1 The LMHA-GM has a DM of 33.8% , which agrees with the values in previously reports [109].

Physical Properties of HA-GM

The DMs of HA-GMs indicate the amount of functional groups for crosslinking among polymer chains. Physically, the degree of crosslinking will affect the water distribution within the hydrogel, which can be revealed from the pore sizes of the

Table 3.1: Degree of methacrylation of HA-GM synthesized by different glycidyl methacrylate to hyaluronic acid ratios

Initial molar ratio	DM of final HA-GM
5:1	7.78%
10:1	25.54%
20:1	33.78%

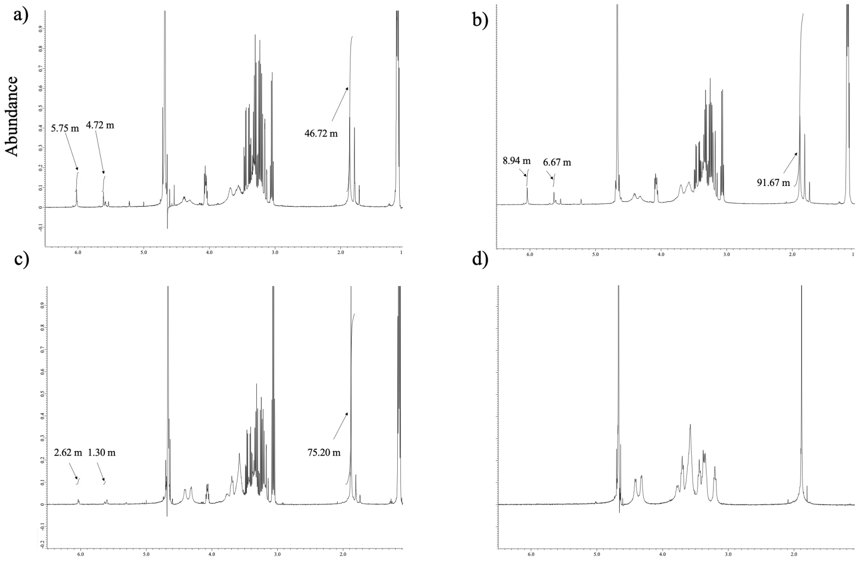

Figure 3.2: ^{1}H NMR of a) HMHA-GM, b)MMHA-GM, c)LMHA-GM, d)HA

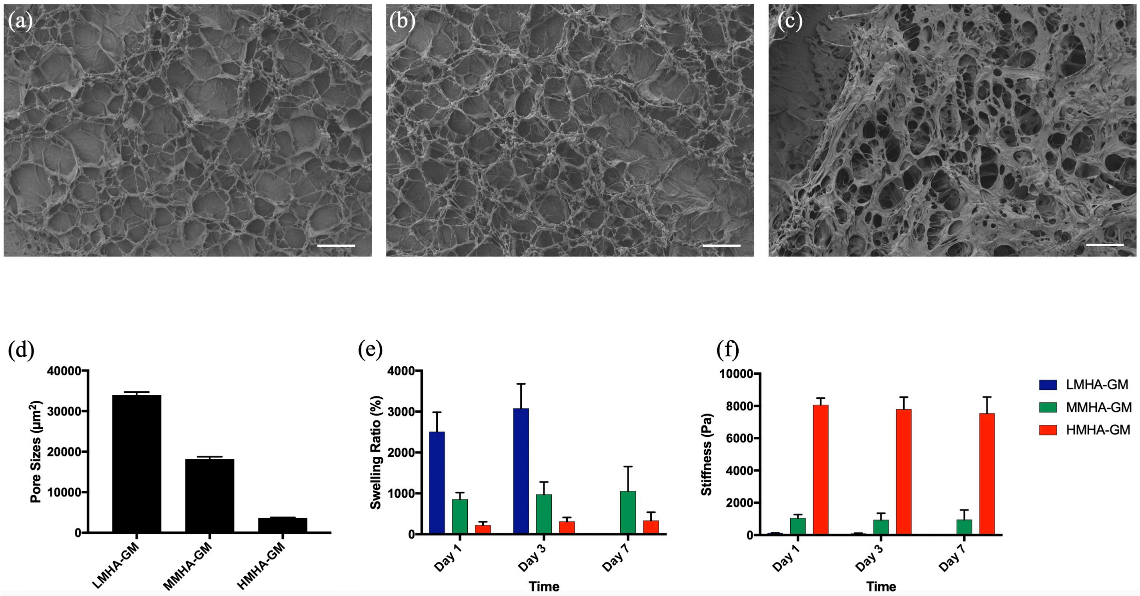

Figure 3.3: Hydrogel characterization: SEM images of dried (a) LMHA-GM, (b) MMHA-GM, and (c) HMHA-GM. (d) The pore size of each HA-GM material indicated that with a higher DM, the resulting photocured HA-GM will have smaller pore sizes. (e) Compressive modulus and (f) swelling ratio of different HA-GMs after curing. Both results show that HMHA-GM has better matched physical properties to use as the ECM to build a multi-layered retina model *in vitro*. Scale bar of SEM images = 100 μ m

hydrogel after removing the water. To examine how the DMs affect the microscopic porous structures of the hydrogels, we compared SEM images of fully cured HA-GM hydrogels after drying. Theoretically, the hydrogels with higher DM will result in structures with smaller and less interconnected pores. As shown in Fig. 3.3 a), b) and c), with the lowest number of DM, the LMHA-GM forms the largest connected pores whereas MMHA-GM has much smaller and isolated pores. The HMHA-GM with the highest DM yielded the smallest pores. The pore sizes of each HA-GM were calculated as shown in Fig. 3.3 1d.

The DMs of hydrogels will affect not only the pore sizes of the hydrogel, but also the physical properties of the gels, such as the swelling ratio. Less crosslinking sites will constitute to lower degree of crosslinking, hence less restrain on the hydrogel under osmotic pressure to swell after crosslinking. The ability of maintaining the structural integrity against swelling is crucial for bilayer construct since it will affect the cell-cell distance and signal transduction within the cell-hydrogel matrix. The less extend of swelling will essentially result in a closer packed matrix for cells to interact. With the least restrains, the LMHA-GM swells the most and eventually lose the shape after 5 days of incubation at 37 C due to the lack of crosslinking sites to withstand the osmotic pressure. MMHA-GM has more crosslinking sites, hence it swells less than the LMHA-GM. With the highest degree of crosslinking, the HMHA-GM has the strongest ability to withhold the osmotic pressure, hence swells the least, as shown in Figure 1e. The porosities of hydrogels were calculated by the ratio between the volume of pores over the volume of the hydrogel. Due to the high swelling ratio of the HA-GMs, there is no significant difference in porosities of all hydrogels since majority of the hydrogel volume is filled by pores containing water.

Furthermore, the compressive modulus of the hydrogel is closely related to the DMs of hydrogels. The higher degree of crosslinking, the more tangling of polymer chains, resulting in stiffer gels under compression. Previous studies have demonstrated that the cell-hydrogel matrix should have the stiffness comparable to native retina, which is about 10-20 kPa, for the survival and development of *in vitro*retina [110, 111]. The compressive modulus of each type of HA-GM hydrogel were measured and demonstrated in Figure 1f. With the highest DM, the HMHA-GM

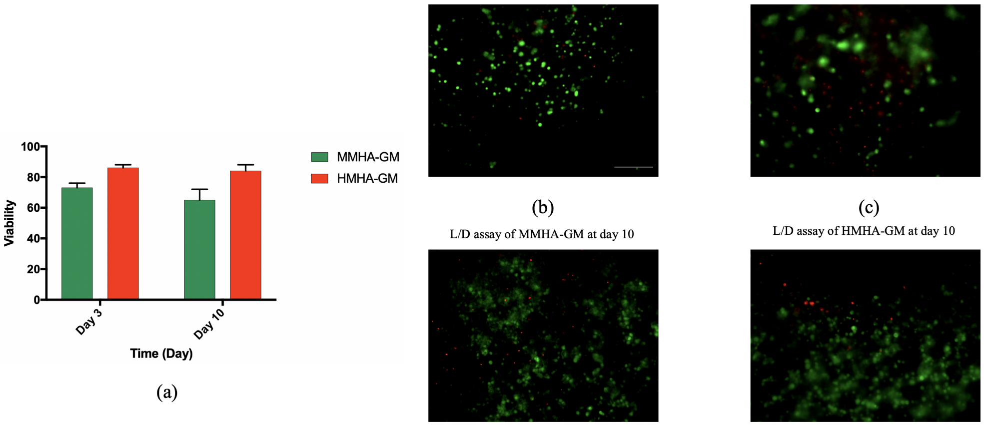

(a)

(b)

(c)

L/D assay of MMHA-GM at day 10

L/D assay of HMHA-GM at day 10

(d)

(e)

Figure 3.4: Viability assay of RPEs encapsulated in MMHA-GM and HMHA-GM. The results shown that RPEs had the highest viabilities in HMHA-GM, which has stiffness close to native retina. Scale bar = 100 μ m.

has the compressive modulus that is comparable to the native retina.

Hydrogel Biocompatibility

To optimize the material composition for cell encapsulation, we investigated viability of RPEs in each HA-GM at different time periods (1 day, 3 days, 10 days). RGDs polypeptide motif was mixed with the hydrogels to improve the cell affinity. For LMHA-GM, the presence of cells did not alter the restrain against osmosis pressure within the matrix, hence it dissolved after 5 days of incubation. The cell viability in the remaining samples were analyzed using calcein AM and Ethidium Homodimer (L/D) assay following manufacturers instruction. The results are shown in Fig. 3.4. RPEs in both remaining HA-GMs show high viability above 70% . Given its low swelling ratio and similar compressive modulus to native retina, the HMHA-GM was selected for the tissue construct.

Multilayer Printing

To create a structure for maturation of PRs from fRPCs [112], we designed a construct to recapitulate the hierarchy of native retina, as shown in Fig. 3.5. Following the structure of native retinas, the base layer was designed with a thickness of 125 μ m to resemble the epithelium tissue. The top layer was 250 μ m tall to give room for the neurons to grow [113]. To validate the print, we created a sample where the bottom layer consists HMHA-GM hydrogel mixed with fluorescein isothiocyanate (FITC) dextran and a top layer mixed with tetramethylrhodamine isothiocyanate (TRITC) dextran. These dextran molecules would illustrate the printed structure due to their different fluoresce colors. The confocal image of the structure is shown in Fig. 3.5 (c). This image demonstrated a bi-layer construct with distinct separation of the two layers.

Differentiation of fRPCs

In cell-hydrogel matrix, the microenvironment around the cells might affect their maturation. To investigate how the HA-GM will affect the maturation process, we used previously reported differentiation protocols on the fRPCs embedded in HA-GM [108]. The fRPCs were mixed with the HMHA-GM and printed in circular shapes. The fRPC-HMHA-GMs were placed in a cell culture incubator with dish and cultured with PR differentiation medium. During the two-week differentiation, small molecules and growth factors (IWP2, DAPT, purmorphamine, retinoid acid, taurin and bFGF) were able to penetrate the scaffold and induce cell reprogramming of fRPCs. As a result, the fRPCs have shown significant morphology change and turn

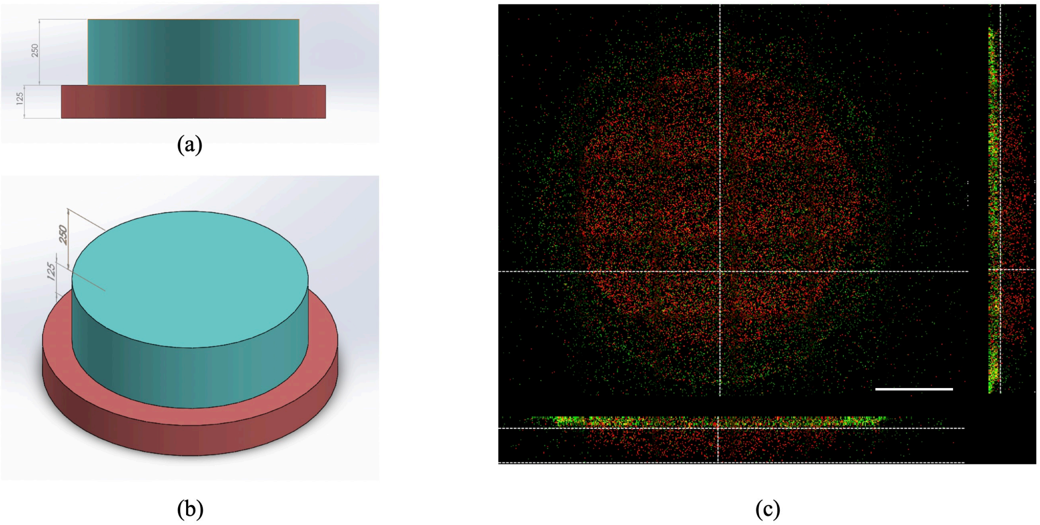

Figure 3.5: Bilayer printing of fluorescent labelled hydrogels: (a) Top view and (b) side view of structural design from SolidWorks®(c) Confocal fluorescent images showing bilayer construct. The printed structure recapitulated the structural design, indicating ability to construct multi-layered structure. Scale bar = 500 μ m.

into typical cone-, rod-like photoreceptor morphology, as shown in Fig. 3.6 a. We used immunostaining of recoverine, a signature protein in the PRs, to verify maturation. The presence of recoverine in Supplement Figure 2b confirmed the maturation of PRs, indicating successful differentiation of fRPC. This strategy has proven that the HA-GM would not alter the differentiation process of fRPCs. We then moved on to include the support from RPEs in the system by printing the bi-layer structure adjacent to the fRPCs.

Bi-layer Construct for PR Maturation

Results from previous tests indicated that HMHA-GM can be used for printing while supporting cell functions and differentiation. We then printed a bi-layer structure

(a) (b)

Figure 3.6: Differentiation of fRPCs

using the HMHA-GM with fRPCs and RPEs following guidance from native retina structure [113]. As shown in Supplement Figure 3, the RPEs were encapsulated into HMHA-GM and printed at the bottom layer with the thickness of 125 μ m. A second layer of HMHA-GM and fRPCs matrix were printed on top of the RPE layer. This design was also expected to introduce a gradient of nutrition and growth factor diffusion from the bottom RPE layer to the fRPC layer, which could guide the orientation of the cells to differentiate into the highly ordered retinal cells including PRs, ganglion cells, and bipolar cells.

To maintain the stability of the cells during differentiation, we modified the differentiation media by adding SU5402 and IWP2 to inhibit FGF and Wnt pathway. These modifications have been proven to have a positive effect during differentiation [10]. With the adapted protocol, we observed PR maturation at day 14. As shown in Fig. 3.7 (a), immunostaining of PR specific marker arrestin-3 indicated signature morphology of mature neurons [114]. The expansion of the outer segment demonstrated development of rod PRs. To further characterize the differentiation of

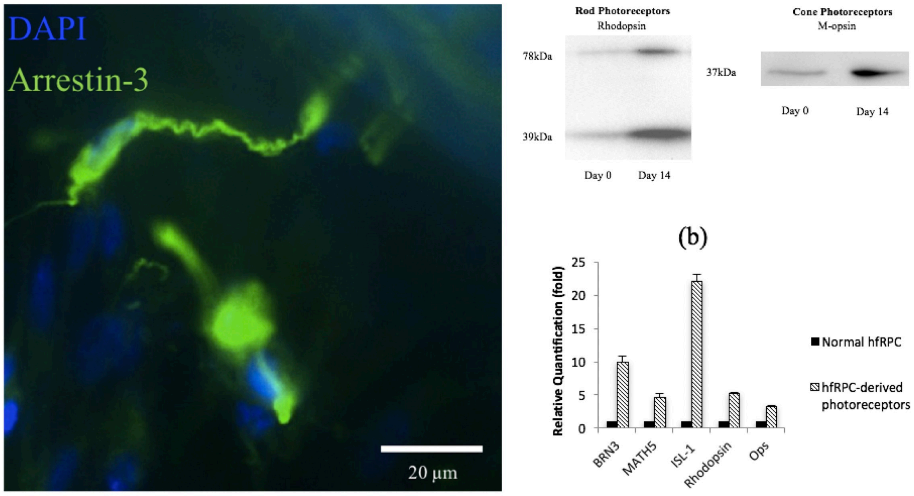

(a) (b) (c)

Figure 3.7: Characterization of co-differentiation: (a) Immunostaining of cone PR specific protein arrestin-3 at day 14. (b) Western blot and (c) qPCR quantification of neuron-specific protein indicating PR maturation.

fRPCs, we used western blot to examine the protein expression in the matrix. As shown in Fig. 3.7 b, the protein profile indicated abundance of both rhodopsin and M-opsin proteins after co-culturing for 14 days, which pinpointed the formation of both rod and cone PRs. Furthermore, we conducted real-time qPCR to verify the neuron formation. As shown in Fig. 3.7 c, the increase in presence of key neuron specific proteins such as Brn3, MATH5 and ISL-1 confirmed the maturation of PRs using the bi-layer construct.

Conclusions

In this work, we have demonstrated chemical synthesis of HA-GMs with different degrees of methacrylation. These HA-GMs exhibit distinctive physical properties such as pore sizes and compressive modulus. We further assessed viabilities of cells encapsulated in these hydrogels and found that the cells have better survival in hydrogels with mechanical properties close to native retina. Furthermore, we have demonstrated bioprinting of a bi-layer structure with cell-hydrogel matrix. After studying the expression of key proteins, we concluded that our co-culture system could recapitulate the native retinal development environment and enhance the maturation of PRs.

3.2 Controlled Growth Factor Release from 3D Printed Hydrogels

3.2.1 Introduction

Growth factors (GFs) regulate proliferation and differentiation of cells in order to promote tissue regeneration [115, 116]. GF turnover is rapid *in vivo*, resulting in very short serum half-lives. In order to better stimulate tissue regeneration, tissue engineering strategies often seek to control the release of GFs [117]. Owing to their controllable degradability and capability to protect enveloped molecules from degradation, hydrogels are often employed to regulate GF release [118, 119]. Hydrogels are cross-linked hydrophilic polymers in which water is the dispersion medium. The high water content, typically 70% to 99% , supports encapsulation of hydrophilic molecules such as GFs, without denaturation and aggregation [117]. Their network structures are also believed to hamper penetration of various proteins, thus preventing premature degradation of encapsulated bioactive molecules from diffusing enzymes [120]. The rich water content also provides physical environments similar to native tissue, thus providing an intimate environment for cells to reside and grow. However, due to high water content, GFs tend to diffuse out quickly from hydrogels since there are no natural moieties where they can attach.

Heparin is a natural linear polysaccharide that is most noted for its anticoagulation effects. It consists of an alternating sequence of disaccharide units with 14 linked 2-O-sulfated iduronic acid and 6-O-sulfated, N-sulfated glucosamine. These building blocks contribute three sulfate moieties per repeating unit, making heparin the highest negative charge density of any known biological molecule [121]. Due to its high negative charge density, heparin can trap positively charged common proteins, such as GFs, by electrostatic forces, which can be used to delay GF release from hydrogel [122–125]. Previous studies have discovered that the kinetics of GF release can be modulated by varying the molecular weight and concentration of heparin in the hydrogel; increased heparin molecular weight and increased heparin concentration results in protracted GF release. This is likely due to a higher electrostatic retention force, which keeps GFs from exiting the hydrogels [126]. However, the low molecular weights of heparin (5-15 kDa) and the repulsion of negative charges limit their crosslinkability. Additional modifications such as acrylation and thiolation also reduce heparins solubility in water to form a stable hydrogel. Thus, most heparin-based systems require another component to create a matrix for modified heparins to reside in [123,126]. Hyaluronic acid (HA) is a hydrogel which has been widely engineered for applications such as wound healing and atopic dermatitis due to its role in granulation and cell migration [94,127,128]. Previous studies have shown that the synthesis of glycidyl methacrylate HA (HA-GM) allows HA to be compatible with light-based 3D printing, as well as provides a mechanism to tune physical properties of the hydrogel [129]. The combination of HA and heparin further allows for the ability to modify GF release kinetics over extended periods of time from hydrogels [130].

To better engineer the hydrogel-based GF delivery system, there is a need to theoretically model drug release profiles from hydrogels. Mathematical models of mass transport in traditional polymeric controlled drug delivery systems have been developed, which allow for the accurate prediction and design of drug release kinetics, accelerating drug development [131]. While the effect of physical shape on the drug release kinetics of conventional dosage forms (i.e. capsules) has been extensively investigated, the influence of hydrogel shape on long term GF release kinetics remain to be quantified [132]. Fundamental studies of the diffusion of proteins in hydrogels have provided some insights on their basic mechanisms. However, due to the lack of control over the shape of hydrogels during fabrication, the role of spatial arrangement within the hydrogels on release kinetics is largely unknown [133,134].

Recent developments in light-based 3D printing allow for the precise control of hydrogel geometry. As one of the most advanced additive manufacturing methods, digital light projection (DLP) based 3D printing techniques has become pivotal in the rapid fabrication of customized hydrogel systems due to its speed and precision [55,101,135,136]. DLP-based 3D printing uses a light modulating device, such as a digital micro-mirror device (DMD), to reflect light in user-defined patterns onto a photosensitive resin. This printing technique has been used to fabricate hydrogel structures with tissue informed, complex geometry, as well as incorporate biomaterials such as GFs and cells directly into the scaffold structure [137,138]. The fast printing speed (typically within 1 min) is also crucial in printing GF-containing hydrogels where release occurs rapidly [124]. Furthermore, DLP-based 3D printing can be used to print functional biomaterials which have been modified to support photopolymerization - such as thiolated heparin (Hep-SH) - in order to tune the hydrogel properties like GF retention [122,139,140]. Therefore, as the influence of hydrogel geometry on GF release kinetics is unknown, the goal of this study is to investigate how geometry influences GF release kinetics in a hydrogel. Hep-SH is synthesized and combined

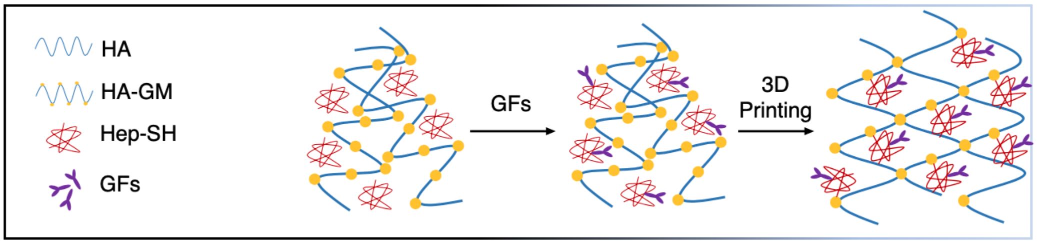

Figure 3.8: Schematic of Synthesis and Polymerization. Thiolated heparin (Hep-SH) was synthesized and mixed with glycidyl methacrylated hyaluronic acid (HA-GM) and growth factors (GFs), followed by 3D printing into a stable hydrogel

with HA-GM and GFs, followed by 3D printing into various geometries (Fig. !3.8). We hypothesized that a barrier layer of HA-GM + Hep-SH could prolong GF release and this bi-layer capsule structure could additionally be used for the sequential release of multiple GFs. The GF release profile is analyzed, and a mathematical model of the release kinetics of each 3D hydrogel design is developed in order to understand the role of geometry on GF release kinetics.

3.2.2 Experimental

Materials

HA with a molecular weight of 200 kDa was purchased from Lifecore Biomedical (Chaska, MN). 1-ethyl-3-[3-(dimethylamino)propyl] carbodiimide (EDC). Sodium chloride, Ellmans test kit and Pierce Bicichoninic Acid (BCA) kit were purchased from Thermo Fisher Scientific (Waltham, MA). 1-hydroxybenzotriazole (HOBt) was purchased from Tokyo Chemical Industries America (Portland, OR). Hydrochloric acid (HCl) cystamine, L-cycstine, tris(2-carboxyethyl) phosphine (TCEP) Glycidyl methacrylate (GM) Dimethyl phenylphosphonite, 2,4,6-trimethylbenzoyl chloride, lithium bromide, 2-butanone, fluorescein isothiocyanate-dextran (FITC-dextran), tetramethylrhodamine isothiocyanate-dextran (TRITC-dextran) deuterium oxide (D_2O) and triethylamine (TEA) were purchased from Millipore Sigma (St. Louis, MO). Heparin was purchased from Celsus Laboratory (Cincinnati OH). Dialysis shells (10,000 MWCO) were purchased from Spectrum Laboratories (Rancho Dominguez, CA). All chemicals were used as received. 1X Dulbeccos phosphate buffered saline (DPBS) was purchased from Gibconco (Carlsbad, CA). Rat-vascular endothelial growth factor (VEGF) and Rat-platelet derived growth factor (PDGF) were purchased from R& D Systems (Minneapolis, MN). The respective ELISA kits were purchased from RayBiotech Life (Norcross, GA). Bovine serum albumin (BSA) was purchased from Gemini Bio-products (Woodlands, CA). Sodium hydroxide (NaOH) was purchased from Spectrum Chemical (Gardena, CA). Polydimethylsiloxane (PDMS) sheets with defined thickness were purchased from Specialty Manufacturing, Inc. (Saginaw, MI).

Synthesis of Hep-SH

Hep-SH was synthesized by adapting a previous protocol [130]. 200 mg of heparin was dissolved into 40 mL of MilliQ water and reacted with 91.04 mg of EDC and 65.05 mg HOBt. The pH was adjusted to 6.8 before 78.06 mg of cystamine was added. The pH of the reaction solution was readjusted to 6.8 and left at room temperature for reaction over 5 hours. The reaction solution was then dialyzed against DI water for 24 hours before lyophilization. The lyophilized powder was then dissolved in 40 mL of water before 966.7 mg of TCEP was added. The pH of the solution was re-adjusted to 7.5. The neutralization was continued for 1 hour in room temperature. The final product was dialyzed against 5M NaCl solution with pH adjusted to 5 by HCl for 24 hours before changing into the solution of the same pH without the salt. The final product was then lyophilized and stored in -20 C before use. The reagent and product were examined by Fourier transform infrared spectroscopy (FT-IR, PerkinElmer, Waltham, MA) and nuclear magnetic resonance (NMR, Bruker, Billerica, MA) to confirm the substitution. The degree of substitution was determined by Ellman's test.

Synthesis of HA-GM and photoinitiator

HA-GM was synthesized following a previously reported method [129]. Briefly, HA was dissolved in acetone/water solution with 1:1 volume ratio. After the HA powder fully dissolved, an equal amount of TEA and GM was added drop-wisely. The reaction continued for 24 hours before dialysis against distilled water. HA-GM foam was obtained after lyophilization, which was re-dissolved into DPBS at predetermined concentrations for printing.

The photoinitiator was synthesized by a previously reported protocol [89]. Dimethyl phenylphosphonate was mixed with 2,4,6-trimethylbenzoyl chloride under argon for 18 hour before heated to 50 °C. Lithium bromide was mixed with 2-butanone and added into the reaction solution drop-wisely. The reaction was cooled to room temperature while precipitates were collected and dried.

3D Printing of Hep-SH with HA-GM

To investigate the effects of Hep-SH and spatial designs on the release of GFs, we printed the hydrogels into cylindrical shapes with core-shell features using our DLP-based 3D printing system [17]. The main components of the DLP-based 3D printing system are an ultra-violet (UV) light source (Ominicure 2000, Waltham, MA), and DMD chip (Texas Instruments, Dallas, TX). The DMD chip consists of 4 millions of micromirrors, which can be individually controlled using a binary, user-defined image. To print a structure, UV light is projected onto the DMD chip, which can in turn project light in a user defined pattern onto a reservoir containing a photopolymerizable hydrogel (Fig. 3.9 A). The prepolymer solution consisted of 1% w/v Hep-SH, 4% w/v HA-GM and photoinitiator in DPBS. To test their respective release kinetics, 200 mg of BSA, 0.1 mg of PDGF, and 0.01 mg of VEGF were dissolved in 1 mL of the hydrogel solution. During the 3D printing process, the hydrogel solutions were loaded into the reservoir between methacrylated glass slides as reported previously [30]. During printing, the hydrogel structures were covalently bonded to the glass surface to prevent diffusion in the z-direction. The glass slides were separated by a 1mm tall polydimethylsiloxane (PDMS) sheet. After printing, the PDMS sheets were removed and UV glue was applied and cured at the four corners of the glass sides to prevent deformation of the hydrogel structure during post printing handling. The structure, together with the glass slides, were then immersed into DPBS reservoir to test the release kinetics (Fig 3.9 B). The overall printing process took less than 1 minute.

subsubsectionPrinted Structure Designs

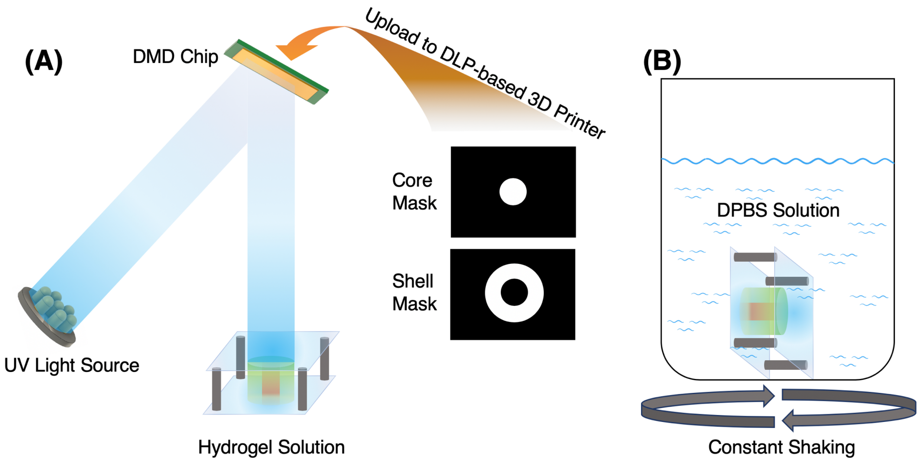

Figure 3.9: (A) Schematic of the DLP-based 3D printing process. The bilayer core-shell structure was fabricated by two digital masks. The first hydrogel was printed into a cylindrical shape and the remaining unprinted hydrogel was rinsed. Then the second hydrogel was printed into a ring shape around the core. (B) The printed hydrogel structures were immersed into DPBS solution to study GF release kinetics.

Several variations of hydrogel composition and geometric shape were systematically tested (outlined in Table 3.2). Each design was printed with FITC and TRITC-dextran containing hydrogels to demonstrate the final structure. First, in order to validate the ability of heparin to prolong GF release, HA-GM and HA-GM + Hep-SH hydrogels were mixed with BSA and printed into a single cylindrical core (Fig. 3.10 A). To further prolong GF release, a bilayer cylindrical core-shell structure, where a BSA containing HA-GM + Hep-SH hydrogel was surrounded by a BSA free HA-GM + Hep-SH hydrogel shell was evaluated (Fig. 3.10 B). To further evaluate the effect of geometric design on the release profile, the thickness of the outer shell of the cylindrical core-shell structures was varied from 0.25 mm to 1 mm (Fig. 3.10 C). Finally, in order to determine whether the release kinematics of multiple GFs could be

Table 3.2: Geometry and Composition of Printed Structures

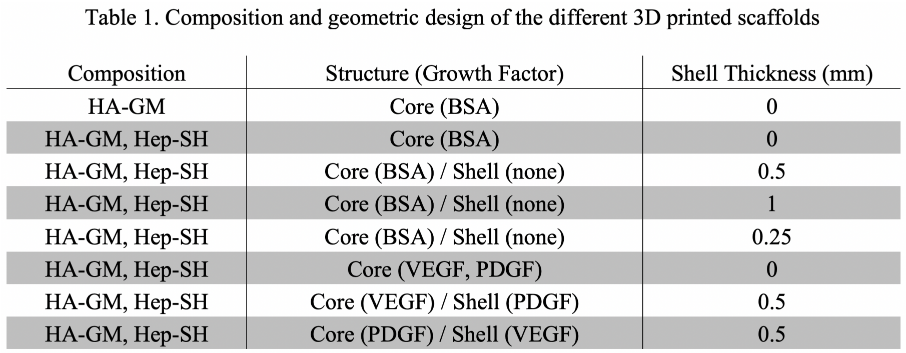

Table 1. Composition and geometric design of the different 3D printed scaffolds

Composition	Structure (Growth Factor)	Shell Thickness (mm)
HA-GM	Core (BSA)	0
HA-GM, Hep-SH	Core (BSA)	0
HA-GM, Hep-SH	Core (BSA) / Shell (none)	0.5
HA-GM, Hep-SH	Core (BSA) / Shell (none)	1
HA-GM, Hep-SH	Core (BSA) / Shell (none)	0.25
HA-GM, Hep-SH	Core (VEGF, PDGF)	0
HA-GM, Hep-SH	Core (VEGF) / Shell (PDGF)	0.5
HA-GM, Hep-SH	Core (PDGF) / Shell (VEGF)	0.5

simultaneously controlled by the spatial order, VEGF and PDGF were encapsulated at either core or shell regions.

Drug Release From Hydrogels

GF release properties of hydrogel structures were assessed every day for 28 days in sealed containment with 1 mL of DPBS. Every 24 hours, 20 μ L aliquots of DPBS were removed from the DPBS reservoir for analysis, and 20μ L of fresh DPBS was replaced in order to maintain the same volume of fluid in the solution. For each GF release profile, data points from four structures in separate DPBS reservoirs were collected. At the end of 28 days, the concentration of the GFs in each aliquot was determined by Pierce BCA essay for BSA release and ELISA for VEGF and PDGF releases. UV-Vis spectrophotometer (Infinite 200 Pro, Tecan, Mannedorf, Switzerland) was used to examine the absorbance and fluorescence of each data point and compared to the standard curves to determine the concentration. These concentration values were then adjusted by the dilution factors from prior removals of DPBS to determine the release profile.

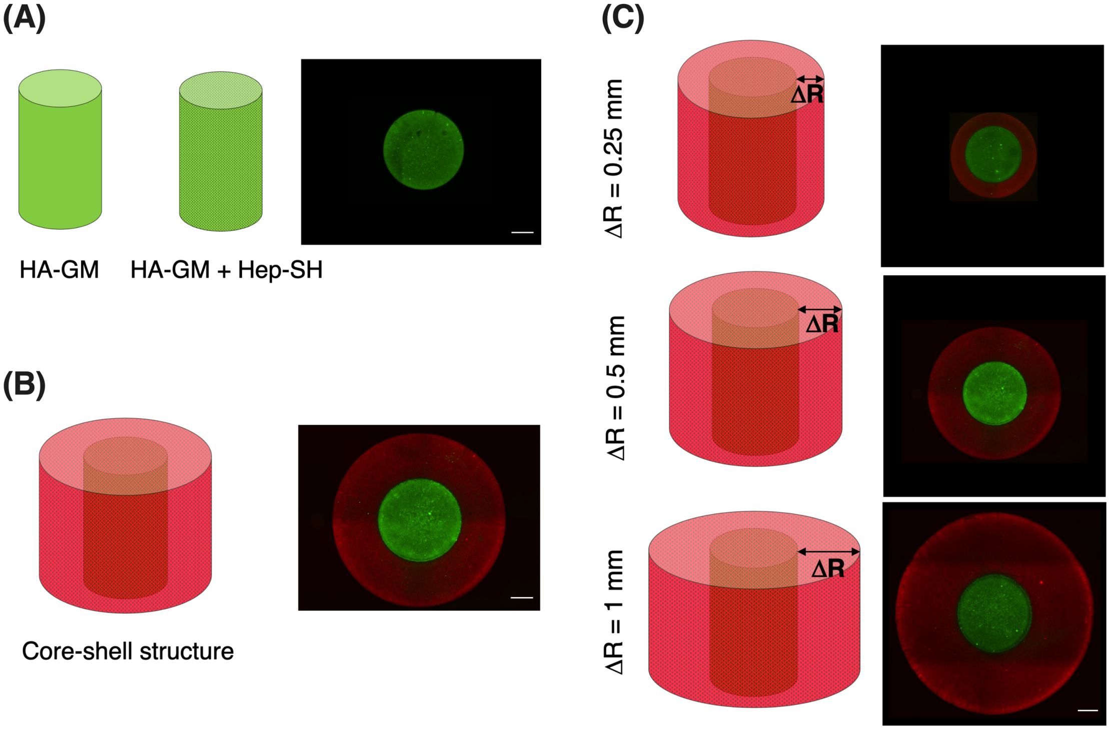

Figure 3.10: Design for 3D printing and structural validation with FITC (green) and TRITC-dextran (red) containing hydrogels. (A) Cylindrical core-only structures, (B) Cylindrical core-shell structures. (C) Core-shell structures with varied outer shell thickness. Scale bar = 200 μm

Mathematical Model

In order to understand the release of GFs from the hydrogel systems, we derived a mathematical model based on the Fick's 2nd Law:

$$\frac{\partial c}{\partial t} = D\frac{\partial^2 c}{\partial x^2} \tag{1}$$

Where c denotes the concentration of the GFs within the hydrogel system, D is the diffusion coefficient of the GF, t and x are time and position respectively. Since both caps of the cylindrical structure were covalently bonded to the coverslips, the GF can only diffuse out of the hydrogel radially. As hydrogel swelling reaches equilibrium after the first day under incubation, the effect of the geometric change and water penetration over time was considered fixed. Also, the initial distribution of GFs within the hydrogel was considered homogeneous at the beginning of the experiment, therefore the initial conditions were defined as:

$$\text{At } t = 0,\ c = c_i,\ -R \leq x \leq R \tag{2}$$

Where c_i is the initial GF concentration and R is the equilibrium radius of the cylinder after swelling. The aqueous solution is well stirred, contains a volume much greater than the volume of the printed structure, and was therefore considered a perfect sink. Thus, the concentration of GFs at far away was assumed to be zero. No accumulation of GFs is considered at the surface of the film. Therefore, the rate at which the GFs diffuse to the hydrogel/solution boundary through the shell was equivalent to the rate at which GFs were depleted from the hydrogel. This is proportional to the concentration gradient between the surface c_s and the concentration required to maintain equilibrium with the surrounding environment c_{∞}. Therefore, this boundary condition can be represented mathematically as:

At t>0, $-D \cdot |\frac{\partial C}{\partial x}|_{x=\pm R} = h\left(c_s - c_{\infty}\right)$ (3)

Where h is the mass transfer coefficient in the shell. Using Laplace transform [132], equation 1 can be solved as:

For the cylindrical structure: $\frac{M_t}{M_{\infty}} = 1 - exp\left(-\frac{2Dt}{R^2H}\right)$ (4)

For the cylindrical core-shell structure: $\frac{M_t}{M_{\infty}} = 1 - exp\left(-\frac{ADKt}{V\Delta R}\right)$ (5)

Where M_t and M_{∞} are the cumulative amounts of GF released at time t and equilibrium respectively. They are results from concentration items (c_s) and (c_{∞}) from equation 3 transformed over time. A represents the total surface area of the hydrogel, D denotes the diffusion coefficient of GF in the hydrogel. H is the height of the cylinder. The partition coefficient K is a measure of relative concentration between the interface shell and the solution at equilibrium condition. It is related to the initial GF concentration and shell thickness. V represents the volume of the drug containing hydrogel, R is the radius of the cylinder and R represent the thickness of the shell.

Statistics

To compare the difference in the drug release profile over time between the HA-GM and HA-GM + Hep-SH hydrogels, a two-way repeated measures analysis of variance (ANOVA) (levels: time, Hep-SH +/-) with a *post hoc* Sidak test was used. To compare the difference in the drug release profile over time between the core only and cylindrical core-shell structures, a two-way ANOVA (levels: time, shell +/-) with a *post hoc* Sidak test was used. The study of shell thickness on retention effect was conducted by a two-way ANOVA (levels: time, shell thickness) with a *post hoc* Sidak test with shell thickness of 0.5 mm as a control. The sequential release of multiple GFs by alternating spatial orders of multiple GFs was investigated by a two-way ANOVA with *post hoc* Sidak test (levels: time, spatial order). The threshold for significance (α) was set to 0.05 for all analyses. All statistics were performed using Prism (Version 7.0a, La Jolla, CA). All data are reported as mean +/- standard deviation.

In order to model the GF release profile, experimental data was fit to equations 4 and 5 respectively in MatLab (Mathworks, Natick MA). Initially, the diffusion coefficient (D) was obtained by fitting the curve to the core only structure. Then, the partition coefficient (K) was obtained using the shell-core design with a radius of 0.5 mm. From the fit D and K values, additional models were generated for the expected GF release profiles of models with varying shell layer thickness. The coefficient of determination (R^2) was calculated between experimental data and the corresponding mathematical model in order to determine the amount of variance explained by the model.

3.2.3 Results and Discussion

Synthesis and UV crosslinking Confirmation from FT-IR and NMR

To confirm the substitution of the thiol group on heparin, we conducted Ellmans test on the heparin solution, before and after the reaction. The assay results indicated 33% substitution of the carboxylic group by the thiol group, similar to previous studies [122, 141]. The reaction to form Hep-SH substitutes less than half of the sulfate groups, leaving the majority of the negative charges untouched. The substitution was further confirmed by comparing the FT-IR and ^{1}H-NMR of the product and native heparin. The broad absorption peak over 1600 cm^{-1} indicated the substitution by the secondary amine from cystamine (Fig. 3.11). The heparin and Hep-SH were dissolved in D_2O and examined by NMR. The chemical shift at 2.6 and 2.85 ppm also confirmed the substitution of thiol group in the Hep-SH. To further confirm the thiol-ene reaction, we mixed Hep-SH with PEGDA and photoinitiator. After UV exposure, the reduction of the absorption peak of alkene around 900 cm^{-1}confirmed the thiol-ene reaction of heparin.

Delayed Release of GFs from HA-GM+Hep-SH Hydrogels

Previous studies have demonstrated synthesis and polymerization of protein retention hydrogels between Hep-SH and HA-GM [126]. The large pore sizes of HA provide space for encapsulated GFs to diffuse out of the hydrogels without obstruction. Thus, it provides an ideal platform to test the drug retention effect due to the addition of heparin. To assess the retention effect of HA-GM, BSA was added to HA-GM and printed into cylindrical structures. Their release pattern was studied by Pierce BCA assay. The initial concentration gradient of GFs between the HA-GM hydrogel and the DPBS solution act to drive BCA out of the hydrogel so that equilibrium is reached. Without any effective retaining agents, the release profile follows zero order pulsatile release, with more than 70% of BSA diffused out of the hydrogel after

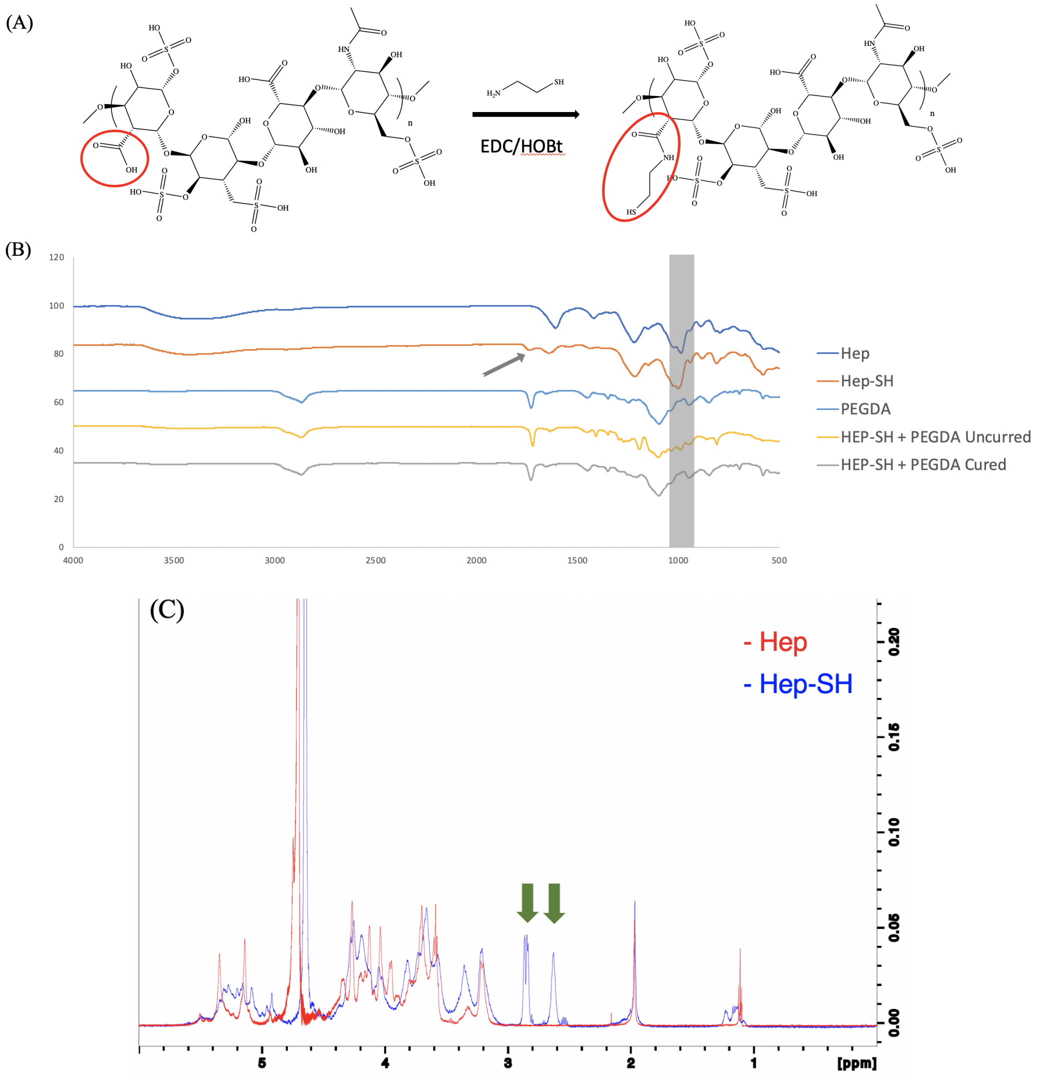

Figure 3.11: Synthesis and characterization of Hep-SH containing hydrogel. (A) Chemical synthesis process (B)FT-IR showing thiolation of heparin at 1600 cm^{-1} absorption and reduction of acrylate group at 900 cm^{-1} (C) ^{1} H-NMR of native heparin and thiolated heparin (Hep-SH)

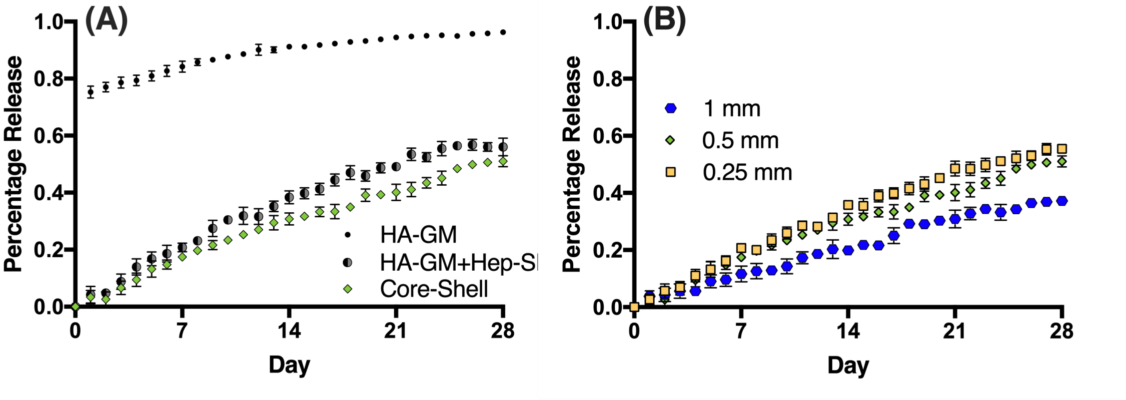

Figure 3.12: Release kinetic of various structures with different composition and shell thickness (A) Release profile of HA-GM only vs HA-GM with Hep-SH core-only vs core-shell structure, (B) Release profile of core-shell structures with different shell thickness.

day 1 (Fig. 3.12 A). The initial burst diffusion of GFs quickly depletes the reservoir of GFs in the hydrogel, thus reducing the chemical potential. The diffusion of BCA out of the HA-GM hydrogel plateaued after 15 days, reaching a local concentration equilibrium after 20 days where 95% of the initial amount of BCA had been released from the hydrogel.

To evaluate the GF retention effect of heparin, we incorporated Hep-SH into the BSA containing HA-GM hydrogel and printed into the same cylindrical structure. The incorporation of Hep-SH into the HA-GM hydrogel was found to significantly decrease the amount of BSA released ($p<0.0001$). A *post hoc* analysis showed a significant decrease in the amount of GF retained at all time points ($p<0.0001$). The release profile of BSA from the Hep-SH + HA-GM hydrogel indicated that less than 10% of BSA had diffused out of the hydrogel on the first day, much less than the 70% BSA diffusion in the HA-GM only hydrogel (Fig. 3.12 A). This is likely due to the increased electrostatic forces attributed to the sulfate groups in heparin. After 28 days, the Hep-SH + HA-GM hydrogel retained 44% of BSA, compared to 4% of the initial BSA in the HA-GM only hydrogel. This experiment confirms that HA-GM itself has poor retention of GFs, but the addition of Hep-SH drastically improves drug retention.

Effect of a GF Laden Core with HA-GM+Hep-SH shell on GF Release

In vivo, the systematic release of GFs is integral to restoring native tissue function after injury. The ability to tailor the release of various GFs in a tissue engineered system allows for a more physiologically relevant replication of the natural cascade of GFs after injury. The DLP-based 3D printing system in this study has previously been used to fabricate HA-GM hydrogels into complex structures [30, 31, 129]. In this study, a similar approach was used to fabricate a complex structure, consisting of two layers: 1) a cylindrical HA-GM + Hep-SH core with BSA, and 2) a HA-GM + Hep-SH shell with no GF incorporated. We hypothesized that the core-shell design would further inhibit GF release, through the addition of a GF retention boundary with no initial concentration of GF.

BSA release in core-only, and core-shell capsules were examined over the course of 28 days (Fig. 3.12 A). The inclusion of the core layer resulted in a significant decrease in the amount of BSA released at all time points after 8 days ($p=0.036$ - $p<0.0001$) with the exception of day 15 where a trend was found ($p=0.0534$). This confirms for the first time that the inclusion of an additional hydrogel layer, not containing any GFs can result in prolonged GF release. For example at day 20, 49%

of the BSA had diffused out of the core-only structure, compared to 39% of BSA that had diffused out of the cylindrical core-shell structure. The experiments demonstrate the GF release profile of a hydrogel can be easily modified by the inclusion of a heparin containing shell, which serves to further slowdown diffusion of GFs out of a hydrogel structure.

In order to further control GF release kinematics, the effect of varying the thickness (R) of the outer shell was examined. Core-shell scaffolds were printed with a shell size double (1mm) and half (0.25mm) of the original design (0.5mm). All release profiles still follow 1st order release. Doubling the shell size resulted in a significantly decreased amount of drug released at all time points after day 3 ($p=0.0137$ $p<0.0001$; Fig. 3.12 B). At the conclusion of the experiment, only 37% of the BSA had diffused out of the cylindrical core-shell structure with doubled shell thickness, compared to 51% of the BSA in the baseline design. Similarly, reducing the shell size resulted in a significantly increased amount of drug released at all time points after day 14 ($p=0.0009 - p<0.0001$). At the end of the 4 weeks observation, 56% of the BSA had diffused out of the cylindrical core-shell structure with halved thickness. Overall, the change in shell thickness significantly altered the GF release ($p<0.0001$). These observations indicate the release kinetics of a GF in a HA-GM + Hep-SH structure can be further tuned by varying geometrical design, which is only possible to fabricate with 3D printing.

Modeling Drug Release Profiles to Predict Release Kinetics

Understanding the relationship between scaffold geometry and GF release kinetics allows for precision engineered GF release platforms. In order to predict drug release profiles from equations 4 and 5, we first had to measure the intrinsic diffusion coefficient (D) and partition coefficient (K) of BSA in a HA-GM + Hep-SH hydrogel. To estimate the intrinsic diffusion coefficient, we initially fit the release profile of BSA in a core-only hydrogel to equation 4. The diffusion coefficient of BSA in a HA-GM + Hep-SH hydrogel was found to be 0.0045 mm^2/day with 96% of the variance explained by the model. Then, using the measured diffusion coefficient, the partition coefficient was obtained by fitting the release profile of BSA in a baseline core-shell design to equation 5. The partition coefficient of BSA in a HA-GM + Hep-SH hydrogel was found to be 0.485 with 98% of the variance explained by the model.

In order to evaluate how well the models predict BSA release in structures with different shell thicknesses, models with R = 1mm and R = 0.25mm were compared to experimentally measured data (Fig. 3.13). Excellent agreement was found for the model with R = 1mm, with the model explaining 96% of the variance. However, poor agreement was found for the model with R = 0.25mm, with the model explaining 53% of the variance in the data. This may be due to a higher concentration gradient across the shell of the thinner shell structures, resulting in a larger driving force and less obstruction for BSA to diffuse out of the structure. This will affect the relative concentrations at equilibrium, which in turn would affect the partition coefficient (K). With larger driving force and a shorter distance to travel before exiting into

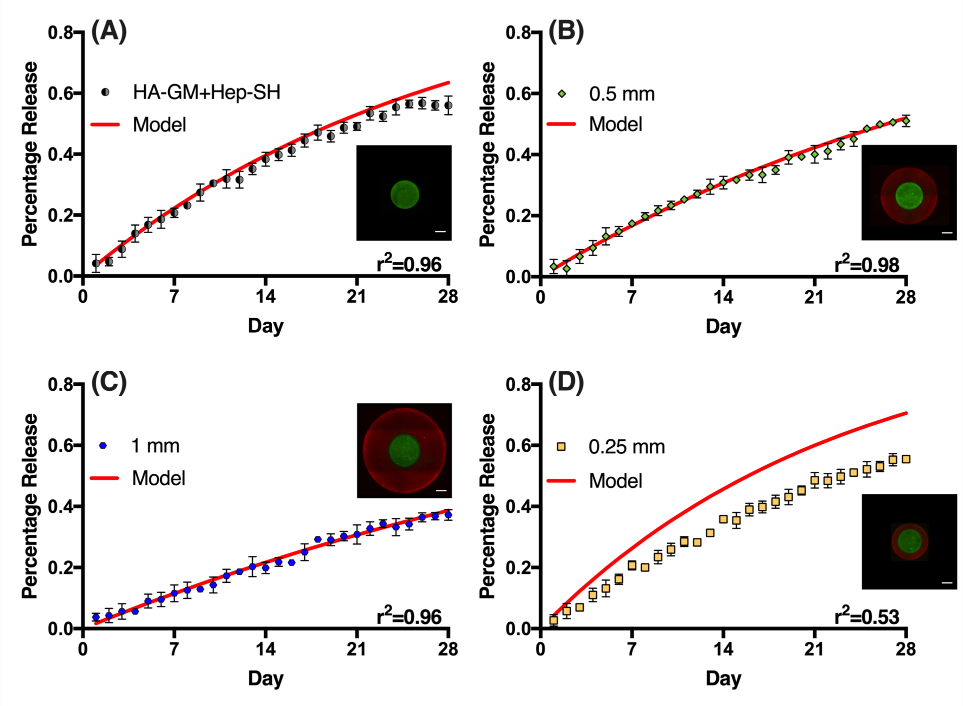

Figure 3.13: Evaluation of models predicting BSA release in structures with different designs and shell thicknesses. (A) HA-GM+Hep-SH core-only structure, (B) Baseline core-shell structure with shell thickness = 0.5 mm, (C) Core-shell structure with shell thickness = 1 mm, (D) Core-shell structure with shell thickness = 0.25 mm. Scale bar = 200 μm.

the aqueous solution, the concentration of GF inside the hydrogel will be lower in the sample with a thinner shell at equilibrium. Therefore, we hypothesize that the partition coefficient for the $R = 0.25$mm should be smaller than what was measured in the $R = 0.5$mm model.

Sequential GF Release

In vivo, GFs are sequentially released in order to initialize cell differentiation and tissue regeneration. For example, the sequential release of VEGF followed by

PDGF has been shown to improve the regeneration of cardiomyocytes [35,36]. As the DLP-based 3D printed system is capable of printing cylindrical core-shell structures with spatial control to alter the release kinetics of GFs, we sought to simultaneously release multiple GFs over an extended period of time. Additionally, we sought to investigate how the spatial ordering of GFs within the cylindrical core-shell structure affects the sequence and rate of GF release kinetics (Fig. 3.14 A). As a control, VEGF and PDGF were mixed into a HA-GM + Hep-SH hydrogel, and printed into a cylindrical structure and the release of each GF was examined by ELISA. The release profile indicated that both GFs are released following 1st order pulsatile release similar to BSA. Additionally, PDGF was found to diffuse slightly faster than VEGF ($p=0.0115$; Fig. 3.14 B).

In order to deliver the VEGF earlier than PDGF, we adapted a similar core-shell approach by printing structures loaded with PDGF first in the core, followed by the hydrogel loaded with VEGF. The release profile indicated that VEGF was released faster than PDGF ($p<0.0001$) and reached 40% release almost three days before PDGF reached the same level (Fig. 3.14 C). This data supports that the sequential release of different GFs from the same structure can be obtained by using the core-shell design. To further explore the flexibility of cylindrical core-shell structure designs, the spatial order of the GFs was reversed by printing a structure with VEGF at the core and PDGF as shell to examine whether the system will work in the opposite order. As anticipated, the release profile indicated that PDGF was released faster than VEGF ($p<0.0001$), reaching 40% released 5 days before VEGF (Fig. 3.14 D). Additionally, the % of VEGF released decreased when printed into the core of the

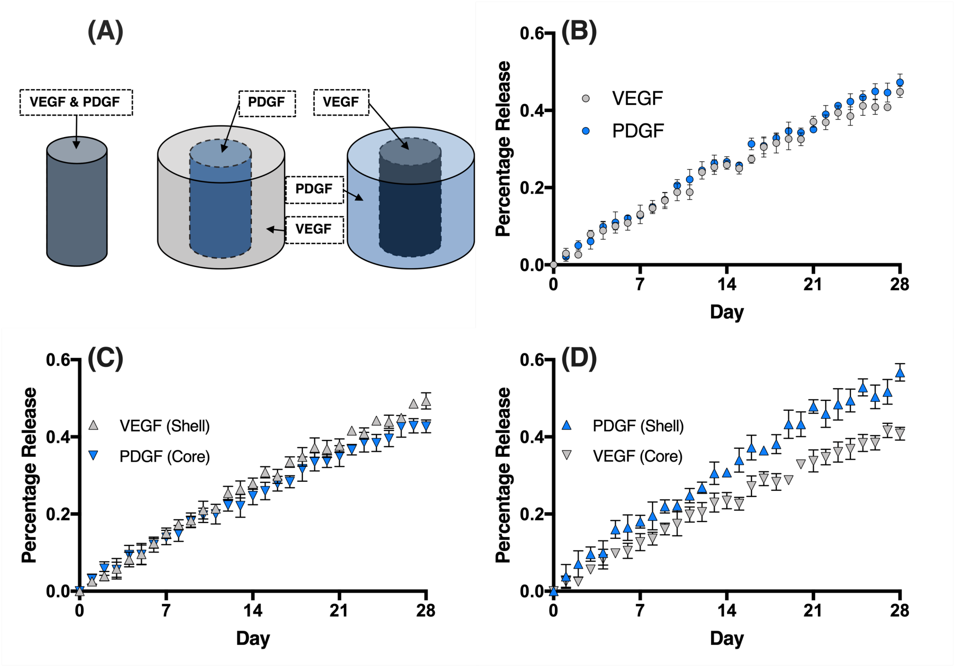

Figure 3.14: Sequential release of VEGF and PDGF (A) Schematics of structural designs (B) Release profile of nonhierarchical structure (C) Release profile of structure with shell containing VEGF and core containing PDGF. (D) Release profile of structure with reversed spatial order. (PDGF shell, VEGF core).

structure as compared to the homogeneously mixed structure (p=0.0135), supporting that the core-shell structure decreases GF release rate, even if there is another GF within the shell layer. As PDGF was released faster in the homogeneously mixed structure, it is unsurprising that the difference in the release rates of VEGF and PDGF was greatest when PDGF was located in the shell of the structure. This likely can be contributed to the higher native diffusion rate of PDGF in this hydrogel system. Finally, both GFs had a significant decrease in release rate when printed in the core of the structure compared to the shell respectively (VEGF p=0.0002; PDGF p<0.0001). These observations further support that the core-shell design can be utilized to modify not only GF release rates, but the sequence in which GFs are predominantly released from a hydrogel.

Conclusion

This study demonstrates how geometry can be manipulated in order to influence GF release from a hydrogel structure for the first time. Heparin was incorporated into a hydrogel to provide retention for GFs. A capsule-inspired, cylindrical core-shell hydrogel structures were 3D printed to study the effect of spatial arrangement on GF release kinetics. The DLP-based 3D printing system used in this study demonstrated excellent speed and flexibility for rapid fabrication of precision engineered multi-material structures. Furthermore, an initial diffusion model was evaluated in order to predict GF release kinetics for different structures. While the diffusion model was ineffective at predicting diffusion kinetics in structures with shell layers approaching 0 mm thickness, the model had excellent agreement with experimental data in structures with a shell layer greater than or equal to 0.5 mm. The failure of the model to predict release kinetics in structures with a smaller shell thickness may be the result from the change in geometric design, which will affect the relative concentration of GFs across the shell at equilibrium which in turn affects the partition coefficient. Finally, the core-shell model was utilized to demonstrate the simultaneous release of multiple growth factors, and how geometric design can be manipulated in order to preferentially release different growth factors in a particular sequence. Nonetheless, a major limitation of this study is that hydrogel system still leaks out GFs right after fabrication. Thus, on-demand delivery with a higher level of control such as tailoring release starting time is still challenging. This is due to the high water content in hydrogels providing a medium for payloads to diffuse out. The initial swelling of hydrogels may also contribute to this effect. Controlled release with distinctive order might be only achieved by polymeric materials where close packing of polymer chains keep the payloads within containment until degraded [37]. Future development of 3D printed hydrogels for GF release include varying shell and core thickness to further control multi-GF release and varying heparin molecular weight to increase or decrease drug release kinetics. This study has demonstrated how geometry can be modified to control GF release profiles in 3D-printed hydrogels, with the long-term goal of developing more advanced drug delivery systems to accurately replicate the complex GF release cascade that occurs *in vivo*.

Acknowledgement

This work was supported by National Institutes of Health (R21AR074763, R01EB021857) and National Science Foundation (CMMI-1644967).

Chapter 4

Rapid 3D Printing of Dual Network by Elastomeric and Bioabsorbable Polymer

4.1 Introduction

Medical operations, such as volumetric repair and wound dressing, requires elastic material that could withstand complex loading conditions and physical manipulation such as patching and suturing. In particular for in vivo operations, the materials need to be bioabsorbable by the body to avoid complication from possible immune response. As one of the best candidates meeting these two requirements, poly (glycerol sebacate) (PGS) has demonstrated superior mechanical properties and controllable bio-degradation due to their chemical structures. Their linear and flexible backbone structures have permitted freedom for polymer chains to move in the presence of external forces, making them easy to elongate before ruptures. Additionally, the presence of ester hydroxyl groups made them permeable to enzymic degradation into shorter chain carbohydrates such as glycerol, which are readily absorbable by our body.

Inspired by natural spider webs and interpenetrating polymer networks, the improved mechanical properties of structures with inter-connected hard and soft segments has become of great research and engineering interest recently. In particular, the double network hydrogel, developed by Suo et. al. contains two types of bonds. The strong bonds link monomers in a chain, crosslink chains in the network, and enable each chain to store high mechanical energy before rupture. While, the weak bonds between chains enable each chain to dissipate all its mechanical energy when the chain breaks. Such tough double network hydrogels show an excellent toughness and flaw tolerance behavior. By combining the elasticity of soft segments and the strength from the hard segments, the overall toughness of the structure can be improved.

Particularly, the spider-web inspired network structures can potentially absorb the same amount of energy from tensile force while having more voids for the overall structures. This is particularly of interest for biomedical applications where open space is crucial for vascularization and engineering degradation process. Suo and his cooperators synthesized tough double network hydrogels. Inspired by the tough double network hydrogels, we proposed the network structure composed by materials with different modulus by PGS.

However, building device from PGS has become a great challenge. Due to their high viscosity and glass transition temperatures, processing PGS are limited to molding and electrospinning into woven-like sheets. To adapt PGS with more advanced manufacturing process, such as additive manufacturing, to make more complex structures, researches have added functional groups, such as acrylate groups into the polymer chain to use it in free-radical based photopolymerization and subsequently light-based 3D printing (Fig. 4.1 A).

In recent work, Singh et. al used laser assisted printing system to build tubes from acrylated PGS (PGSA). However, due to the lack control of light processing techniques, the structures lack resolution and hardly applicable in biomedical application. DLP-based 3D printing system has demonstrated rapid processing time with dynamic control of light during printing. In previous publications we used it to investigate the relationship between exposure time, degree of crosslinking, thus the mechanical properties of polyurethane materials [17]. By assigning different exposure conditions at designed locations, we have printed structures with discrete stiffness out of the same material. This technique enabled printing of multi-component structures

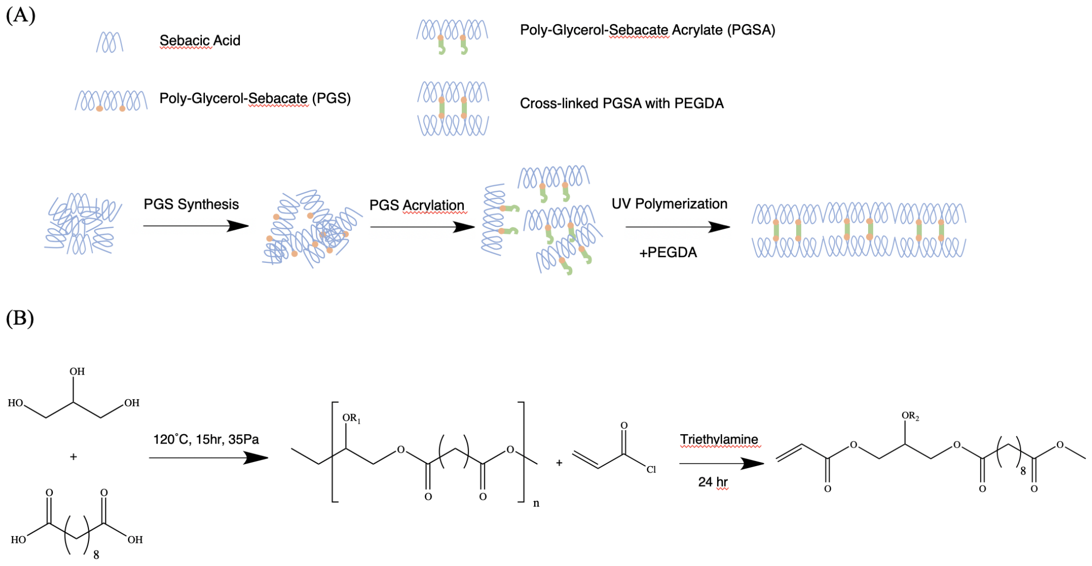

Figure 4.1: Photopolymerization of PGSA

with distinct mechanical properties with single material rather than multiple materials, which simplified the process and shorten the fabrication time. It could also be easily adapted in printing double-network structures by allocating different exposure conditions at hard and soft segments. In this work, we would like to investigate how to modulate the mechanical properties of the PGS materials by crosslinker density as well as printing conditions. Furthermore, we used both finite-element analysis (FEA) and 3D printing to investigate the enhanced mechanical properties of double network structures. The materials with different crosslinker density and exposure conditions, as well as the double network structures were printed and tested by standard tensile tests to evaluate their mechanical properties. By combining the strength from simulation and dynamic 3D printing, the toughening mechanism of double network was revealed.

4.2 Experimental

4.2.1 Materials

Triethylamine (TEA), Diphenyl (2,4,6-trimethylbenzoyl) phosphine oxide (TPO), anhydrous dichloromethane (DCM), D-chloroform ($CDCl_3$) polyethylene glycol di-acrylate (PEGDA) with molecular weight of 700 Da and gelatin were purchased from Millipore Sigma Aldrich, MO. Sebacic acid (SA), glycerol, 4-Dimethylaminopyridine (DMAP), Ethyl Acetate (EA) were purchased from Fisher Scientific, NH. Acryloyl chloride (AC) was purchased from Alfa Aesa, MA. For cell culture and viability test, Dulbeccos Modified Eagle Medium (DMEM), fetal bovine serum (FBS) and penicillin/strepotomycin (P/S) Calein AM were purchased from Thermo Fisher Scientific, MA. Ethidium Homodimer was purchased from Biotium, CA.

4.2.2 PGS Synthesis

PGS was synthesized following a previously reported protocol with modifications (Fig. 4.1 B). All glassware were pre-dried by heat 24 hours prior to experiment. SA and glycerol were mixed with 1:1 molar ratio and melted at 140 °C over 1 hour under argon. The polycondensation was conducted at 120 °C in three-necked round bottom glass flask with pressure reduced to 35 Pa. The reaction was continued for 15 hours while pressure was maintained at 35 Pa with active pumping. The final product has conversion rate of 90% by calculating the weight difference before and after the synthesis.

4.2.3 PGSA Synthesis

The acrylation reaction was conducted from previously published method with modifications (Fig. 4.1 B). All of the containers used in the reaction were dried in heat oven at 55C prior to the experiment. 30 g of PGS were dissolved in 300 mL of DCM followed by 30 mg of DMAP. The reagents were cooled to 0 °C under argon for 10 minutes before 7 mL of TEA were added dropwise. 3.3 mL of AC was added drop-wisely over period of 5 min. The reaction was continued in room temperature for 24 hours. After the synthesis, DCM was removed by rotary evaporation at 40 °C and the remining solution was dissolved in EA to precipitate the excess TEA. The mixture was filtered, and the solute was collected, which was further dried by rotary evaporation at 50 °C at 5 Pa. The final product was stored at -20 °C

4.2.4 ^{1}H NMR Characterization

^{1} H nuclear magnetic resonance (^{1}H NMR) spectra of the PGS and PGSA were measured (JEOL-500, Peabody , MA) and compared to confirm the chemical structure of the final products. Chemical shifts were referenced relative to the peak of CDCl3 at 7.26 ppm. The signal intensity of the methylene groups of sebacic acid (1.3 ppm) and the average of the acrylate groups (5.85 ppm, 6.15 ppm and 6.4 ppm) were used to calculate the degree of acrylation to be 40%.

4.2.5 Mechanical Properties of PGSA/PEGDA resins

The PGSA/PEGDA resins were prepared by adding PEGDA as crosslinkers with concentrations of 1% (LoResin), 5% (MeResin) and 10% (HiResin) respectively. 4% (w/w) of TPO was added in to the solution as photoinitiator. The materials were printed into modified ASTM Type IV tensile bars with our 3D printer under the same exposure intensity with different durations (30s, 45s and 60s) respectively. Tensile tests were conducted with Instron 5920 (Norwood, MA) following constant strain rate of 0.5% /s. The tensile modules were determined by the tangent of the stress/strain curve during elastic deformation. The ultimate tensile strength and failure strain was obtained at the rupture points of the tensile test.

4.2.6 3D Printing of PGSA/PEGDA resins

The structures were printed by our continuous 3D printing system (Fig. 4.2 A). First, a 3D model was designed by Fushion 360 ®and processed by our in house software into a series of images. The images were uploaded onto DMD chip and used to pattern the projected lights onto the polymer reservoir. The HiResin were loaded in the reservoir with PDMS coated bottom and the build platform was immersed into the resin solution. During printing, the series of images were projected onto the resin while the build platform raised up to allow structures to be printed on it in a layer-by-layer fashion on top of previous layer. The oxygen inhibition from the PDMS prohibits the crosslinking of the resin to the bottom layer. By changing the optic modules, structures with 100-micron features as well as in decimeter sizes were printed. The printed structure was removed from the build platform and washed using

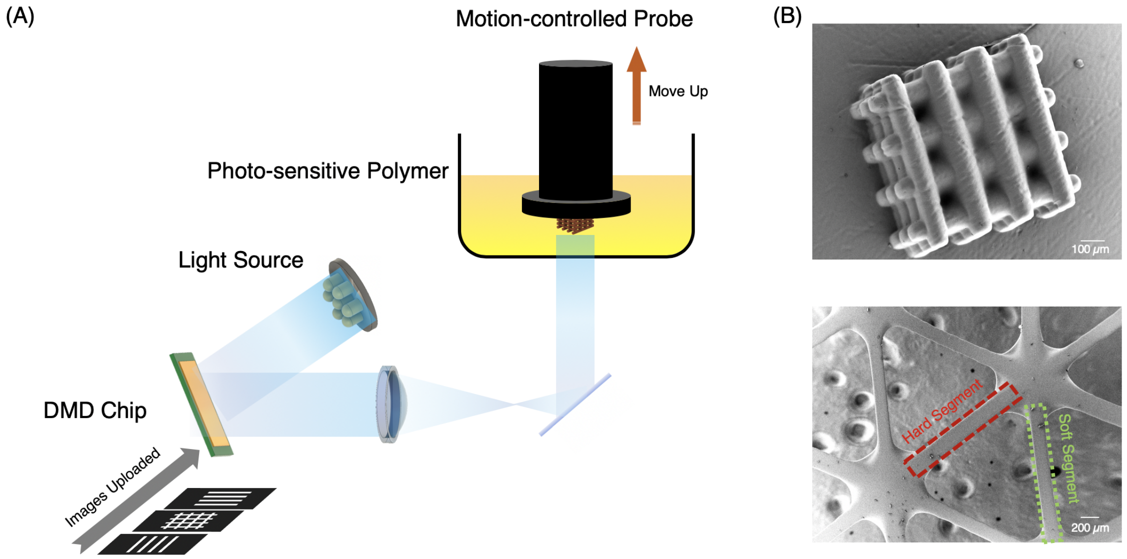

Figure 4.2: 3D Printing of PGSA/PEGDA Resin

IPA before further examination by optical microscopy camera and SEM (Fig. 4.2 B).

4.3 HUVEC Viability Test

Human umbilical vein cells (HUVEC) were purchased from ATCC ő (Manassas, VA) and cultured in Endothelial Cell Growth Medium 2 (EGM-2) from PromoCell ®, Heidelberg, Germany. The cells were harvested after 7-9 passages. The PGSA/PEGDA composite was printed into disks with diameter of 4 mm followed by coating with 2.5% gelatin solution for 30 minutes at 37 °C. The disks were washed with PBS and immersed in growth media 1 day before seeding. At day 1, 3 and 7 post seeding, the disks were washed thoroughly with PBS and stained by calcein AM (Invitrogen ®, Carlsbad, CA) and ethidium homodimer-1 (Biotium ®, Fremont, CA) per manufacturers protocol. The cell viability was assessed by pictures from fluorescence microscopy (Leica DMI-6000, Wetzler, Germany) and ImageJ analysis.

4.4 Tensile test of network structures

The single network with exposure time of 30s and 60s, as well as double network structures containing these two exposure conditions as soft and hard segments respectively were printed with HiResin. The tensile tests were setup on Instron 5920 with the same parameters as for the tensile bars made by PGSA/PEGDA resins. During the test, a video was recorded to assess the rupture propagation, as well as comparison to simulation. The tensile modulus was determined by the tangent of the stress/strain curve during elastic deformation and the failure strain were obtained by the fracture point of the curve. The toughness was calculated by the integrals of area under the curve.

4.5 Finite element simulation

The tensile behavior and failure process of double-network made by HiResin was simulated using the Abaqus (version 6.13) combined with self-developed codes. The geometries of network are based on the measured parameters from tensile test of HiResin and SEM measurements (shown in Fig. 4.3). The mechanical properties of network are from figure 3 and shown in Table S1. The beams in network are meshed with beam element (B23). When the tension stress of beam element reaches the strength, this element is deleted, and a new structure generates. The new structure

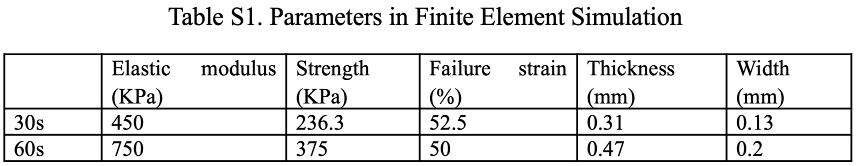

Table S1. Parameters in Finite Element Simulation

	Elastic modulus (KPa)	Strength (KPa)	Failure strain (%)	Thickness (mm)	Width (mm)
30s	450	236.3	52.5	0.31	0.13
60s	750	375	50	0.47	0.2

Figure 4.3: FEA parameters

is stored into a new input file (.inp) and then calculated by Abaqus. The above calculation processes are integrated into self-developed codes. The strain and stress of network is calculated and plotted in Fig. 4.4.

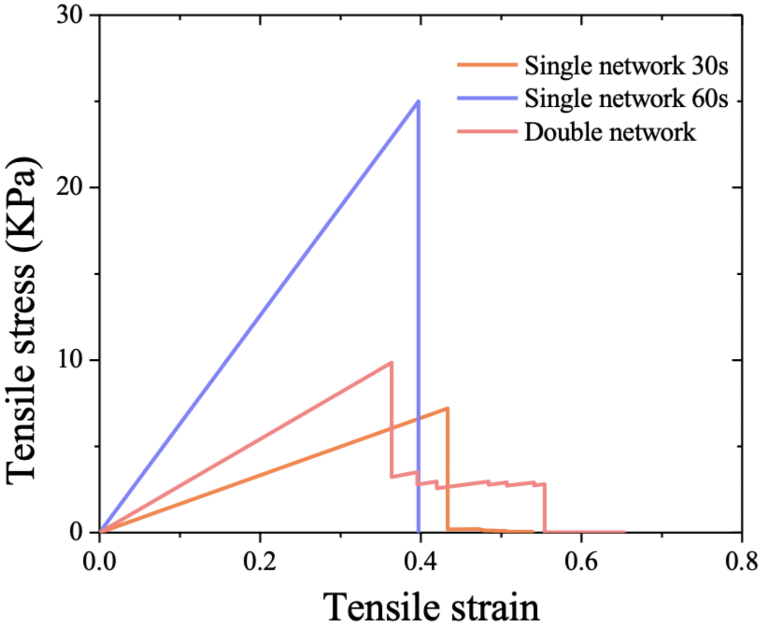

Figure 4.4: Simulation Results for Tensile Tests of Network Structures

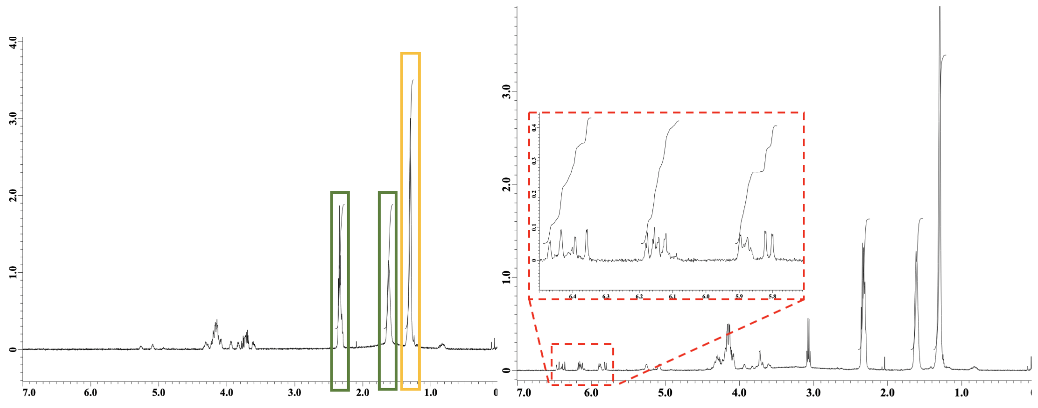

NMR of PGS

NMR of PGSA

Figure 4.5: ^{1}H NMR Results of PGS and PGSA Synthesis

4.6 Results and Discussion

4.6.1 Synthesis of PGSA

The successful synthesis of PGS was confirmed by ^{1} H NMR in Fig. 4.5. The substitution by acrylation group was confirmed by the chemical shifts at $\delta 6.4$, 6.15 and 5.9. The acrylation ratio was calculated by the ratio between the average of acrylation groups and that of the methyl groups on the PGS backbone with chemical shifts at $\delta 2.4$. Our protocol yielded PGSA with acrylation ratio of 40%.

4.6.2 3D Printing of PGSA

Our 3D printing system has demonstrated high precision and fidelity in fabricating structure with small features with materials such as PU, PC and hydrogels [17, 30, 129]. As a proof of concept, a 6 layered log pile structure with rods of 75 μm in diameter perpendicularly to each other between each layer was designed and printed. The log pile structure was printed with high resolution lens module and examined by SEM. The structure has recapitulated the details from design, such as the smooth surfaces and layered structure. Additionally, our printing system has provided the versatility of printing structures with the large features, such as the network structure with total size 17 cm X 7 cm X 0.1 cm, which was printed with high range lens module. Moreover, the printer can be used to print a structure with different mechanical properties by allocating explicit exposure time at specific locations. The network structures were printed following the guide from the design with the hexagon skeletons using longer exposure time whereas the internal diagonals with lower durations. By using different printing time, we have fabricated a network where the skeletons with stronger material to retain the shape and the diagonals with softer material to absorb the energy. The SEM image in Fig. 4.2 B has shown the smooth surface of the double network structure printed.

4.6.3 Mechanical Properties of PGSA/PEGDA Resin

The PGSA and PEGDA resins provided a molecular-scale double network where main component PGSA provided the elasticity and crosslinker PEGDA gave the strength. Thus, by changing the relative concentration of each components, the mechanical properties of the final polymer could be modulated. To investigate their relationship, we prepared samples with crosslinker concentration ranging from 1% (LoResin), 5%(MeResin) and 10%(HiResin). They were printed into modified ASTM type 4 tensile bars and tested following ASTM standards. As shown from Fig. 4.6, the tensile modulus and ultimate tensile strength of three resins follows

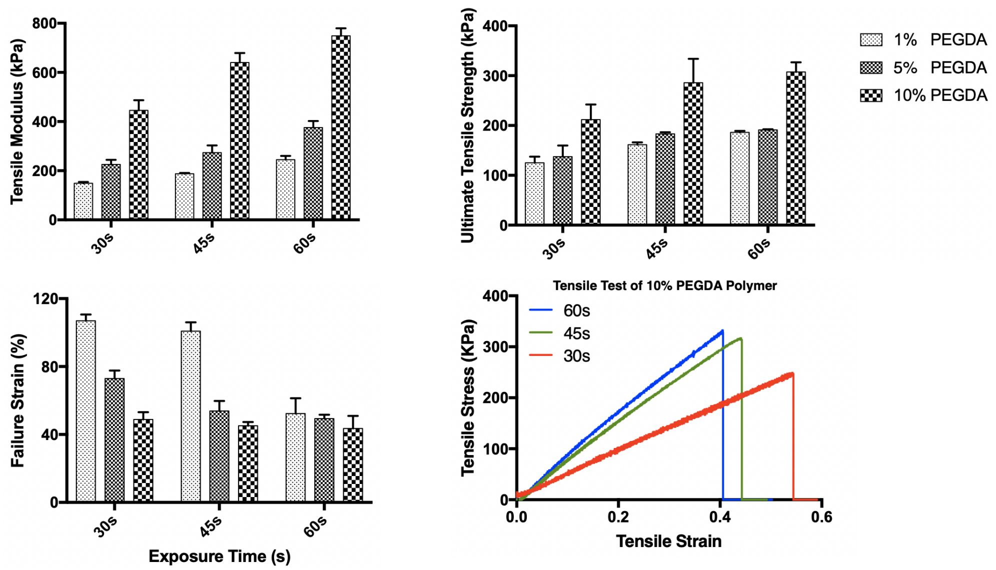

Figure 4.6: Tensile Test Results of PGSA/PEGDA Resins

the order of LoResin < MeResin < HiResin whereas the failure strain follows the reverse order. Such observation could be explained by the polymer network structure composition. The flexible PGSA polymer chains could move freely with respect to each other, thus providing the room for elongation of the polymers. However, the short-chain crosslinker PEGDA bring the PGSA polymer chains closer to each other while restricting their motions by forming network structure between them. In the presence of external forces, the PGSA polymer chains in HiResin has limited room to change their conformations and locations, thus the chemical bonds of the backbone structures and crosslinker will withstand the forces, making the polymer stiffer and stronger. The restriction for PGSA polymer chains to move also reduced their elongation before rupture, making the HiResin having the lowest failure strain.

Other than the composition, the mechanical properties of the printed structure could also be tailored by varying the exposure time, hence the degree of cross-linking.

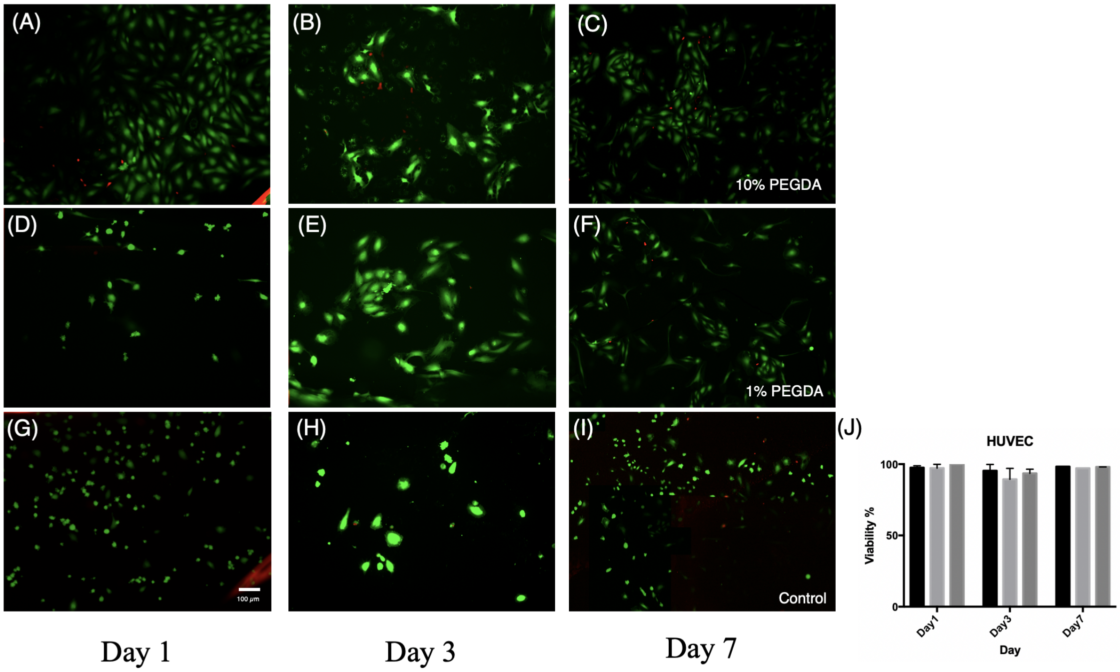

Figure 4.7: HUVEC Viability Test on PGSA

In our previous publications, we investigated the relationship between the exposure time and the stiffness of the printed structures [17]. To apply the similar approach in the PGSA/PEGDA resins, the same materials were printed with different exposure time, ranging from 30s, 45s and 60s. As shown in Fig. 4.6. the longer exposure time will provide structures with more crosslinking, hence higher strength but lower failure strain. This could be explained by the same analogy as for crosslinker concentrations in previous discussion.

4.6.4 HUVEC Viability

Previous studies have reported that PGSA supported fibroblasts and cardiomyocytes. However, as a potential material for vascular patch and grafting, the response from vascular endothelial has yet been discussed. The viabilities of HUVEC cells on coated PGSA/PEGDA resins have indicated good compatibility of the material. Compared to seeding on covershlip glass as control, the results show similar viability ($p<0.005$) (Fig. 4.7), indicating a potential choice for vascularization work. Their reported degradation also show suggest in will be compatible for in vivo repair.

4.6.5 Tensile Test of Network Structures

The results from the tensile tests on single (SN) and double network (DN) structures were presented in Fig. 4.8. As predicted by the models, the SN with 30s exposure has the lowest elastic modulus whereas the SN with 60s exposure is the strongest amongst the three structures printed. The elasticity of double network structure fell in between the two SN structures, as predicted. The failure strain appeared to be the reciprocal relationship with the elasticity of the structures where the softest SN structure printed in 30s has the longest elongation and the strongest structure has the shortest before rupture.

4.6.6 Toughening Mechanism of Double Network Structure

For SN structure, the beam sustains the stretching deformation (stretching-dominated structure). For DN structure, the soft beam still sustains the stretching deformation, but the stiff beam sustains bending deformation if the modulus of stiff beams is much larger than that of soft ones. Bending deformation of stiff beam results in the large deflection but small stress in the stiff beams. As shown in the figure 4, the dimensionless stress (ratio between stress and strength) of soft beam is

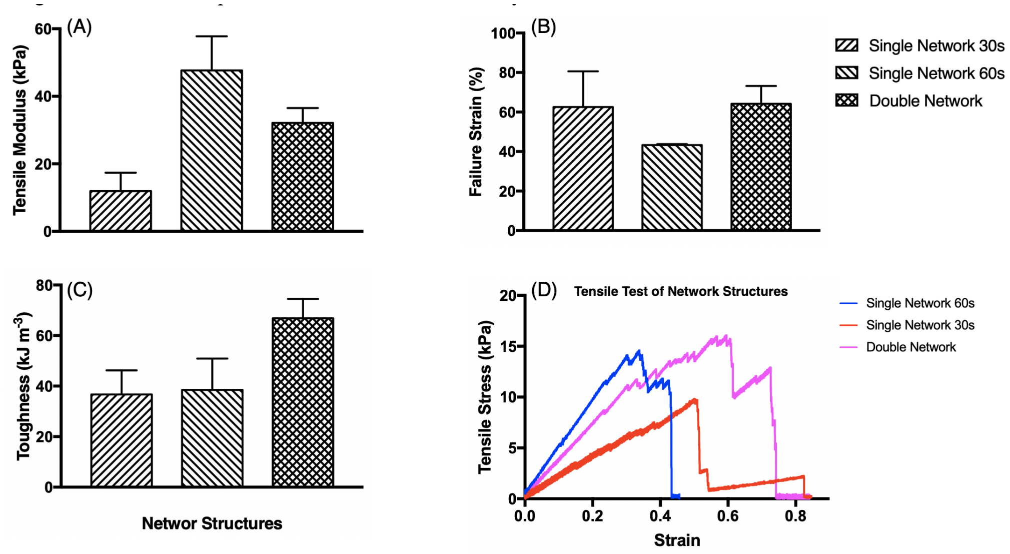

Figure 4.8: Tensile Test Results of Network Structures

larger than that of stiff beams. As a result, the stretched soft beam firstly reaches the strength and be broken without any breakage of stiff beam. Compared with the failure of SN structure, the failure of DN structure is controllable. Some of soft beams break before any breakage of stiff beams. As we seen from Fig. 4.9 - Fig. 4.12), the work of rupture of soft beam and stiff beam is the same. The breakage of soft beam will dissipate a lot of energy and avoid catastrophic failure of whole network. The generously sequenced breakage of soft beams will also keep the integration of the structure and maintain the function of the structure. Both our simulation results and experimental results show that the failure strain of double network before catastrophic fracture is larger than SN structures and bulk materials. The ductility of DN structure is dramatically increase based on this design.

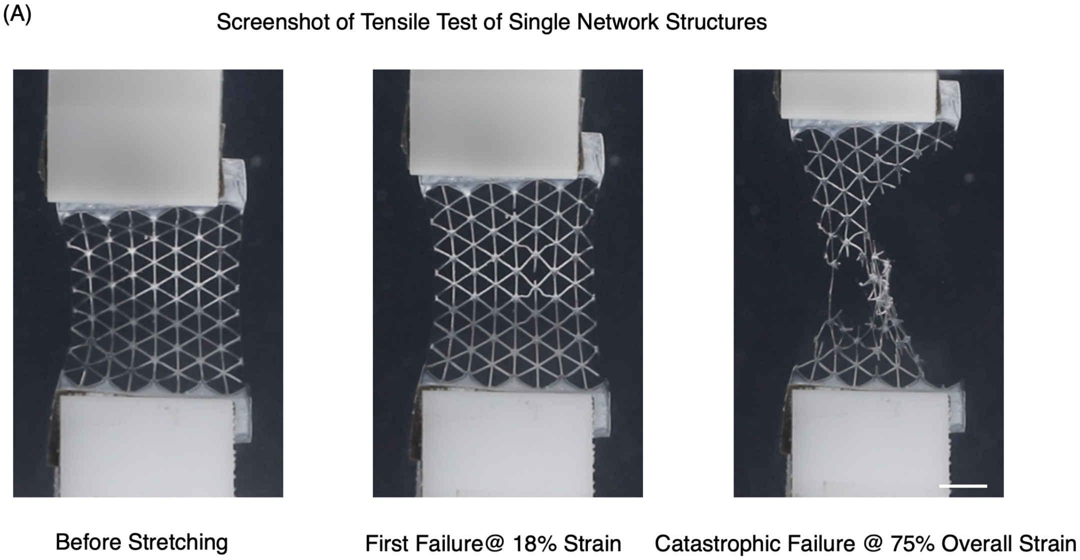

Before Stretching

First Failure@ 18% Strain

Catastrophic Failure @ 75% Overall Strain

Figure 4.9: Rupturing Process of Single Network Structures

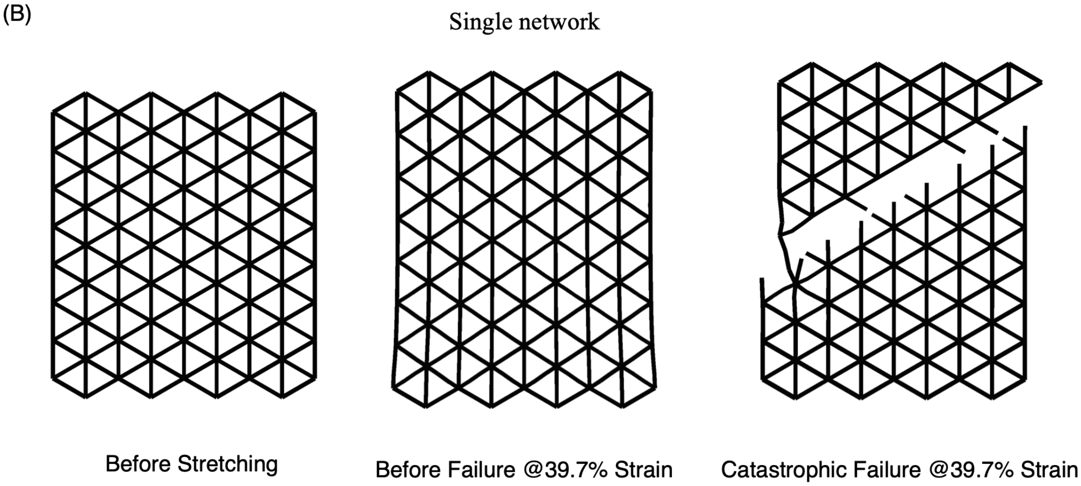

Before Stretching

Before Failure @39.7% Strain

Catastrophic Failure @39.7% Strain

Figure 4.10: Simulated Rupturing Process of Single Network Structures

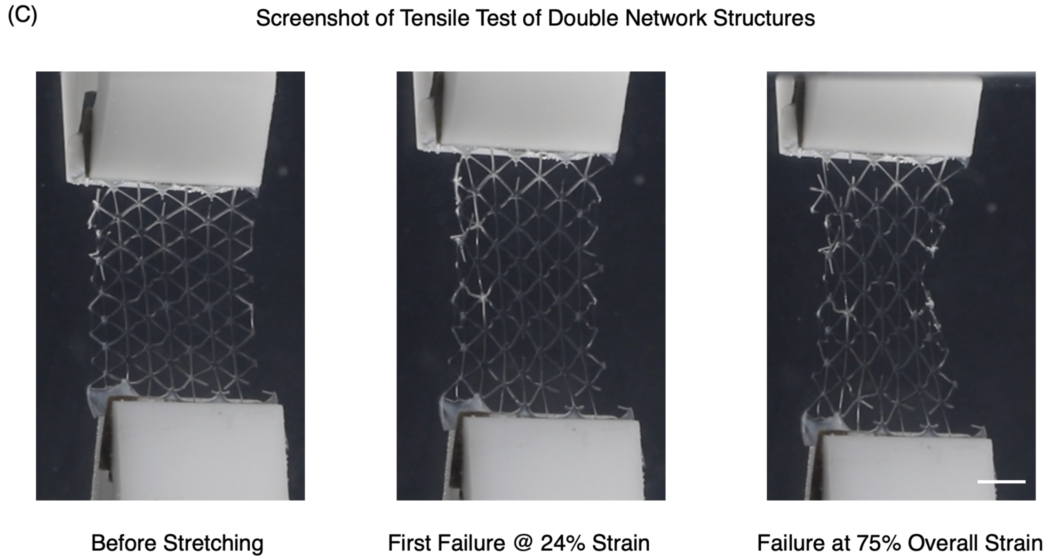

Figure 4.11: Rupturing Process of Double Network Structures

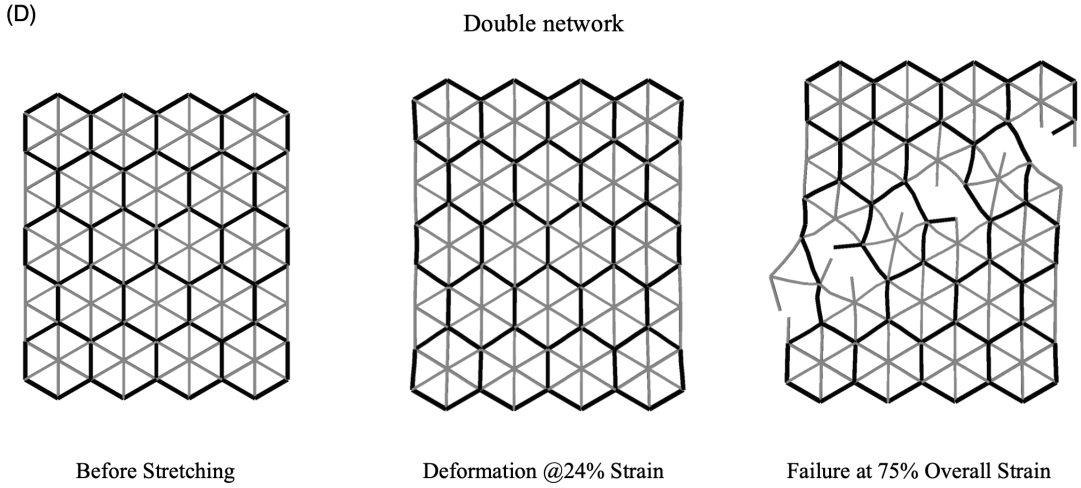

Figure 4.12: Simulated Rupturing Process of Double Network Structures

4.7 Conclusion

This study has demonstrated the synthesis of elastomeric PGSA material by esterification and acrylation. The DLP-based micro-scale continuous printing system (ţCOMP) was used to print the polymer into structures sub-100 ţm resolution within minutes. The mechanical properties of the polymers with different concentrations of crosslinkers and exposure duration were examined. The results shown that by modulating these two conditions, the elastic modulus of the printed polymers ranged from 150 kPa to 800 kPa while the ultimate tensile strength expanded from 100 kPa to 300 kPa. All of the printed polymers could sustain more than 50% strain before failure, which is optimal for most of biomedical applications, with some specific combinations reached 100% strain before rupture. Furthermore, a polymer inspired double network structure were printed by allocating hard and soft segments in specific locations using different exposure durations. This double network structure demonstrated enhanced toughness by introducing soft sacrificial arms to absorb the energy during tensile test while the hard segments withstand the overall structure intact. To understand this observation, a finite-element analysis was conducted to evaluate the mechanism. This study has demonstrated methods of fabricating structures with enhanced mechanical properties from elastomeric polymers with long-term goals of developing functional and bioabsorbable medical devices for implementations.

4.8 Acknowledgement

This study was supported in part by grants from Department of Defense (W81XWH-14-1-0522), California Institute for Regenerative Medicine (RT3-07899), and National Institutes of Health (R01EB021857 and R21HD090662). We would like to appreciate Zhaoqiang Song, David Berry, Amy Moran, Wisarut Kiratitanaporn, Jacob Schimelman, Bingjie Sun, Frank He, Brian Xi for their effort in this work.

Chapter 5

Conclusions

5.1 3D Printing Polyurethane for Biomedical Applications

The use of three-dimensional (3D) printing for rapid prototyping and manufacturing has promised to produce components with complex geometries following customized designs. Due to the excellent mechanical strength, flexibility and potential biocompatibility, polyurethane (PU) has been developed for fabricating convoluted biomedical devices by 3D printing. It offers many advantages in the manufacturing of PU, including high fidelity, cost effectiveness and volatile customization. For the past decade, numerous studies have explored 3D printing of PUs for biomedical research. Notably, most of the work reported utilized an extrusion-based 3D printing system. This chapter will discuss the properties of 3D printed PUs as well as their potential application in the fields of biomedical engineering. 3D printing techniques such as inkjet-based, extrusion-based and stereolithography are introduced and compared. Lastly, we will explore the future application of 3D printed biocompatible PUs in biomedical research.

5.2 Continuous 3D Printing of Green Aliphatic Polyurethanes

Photo-sensitive diurethanes were prepared from methacrylate functionalized six-membered cyclic carbonate and biogenic amines. A continuous optical 3D printing method for the diurethanes was developed to create user-defined smooth gradient and complex surface microstructures in mere seconds. The resulting polyurethane from green chemistry synthesis (gPU) showed high transparency and good optical and mechanical properties. The gradient stiffness of the printed structure was obtained, and the range of stiffness was tunable by controlling the exposure time and selecting various amine compounds. 3D bio-mimicking and intricate structures featured with smooth curves and complex contours were printed using the gPU materials with high resolution. High cell viability (over 95%) was obtained in cytocompatibility testing using C3H 10T1/2 cells seeded directly on the printed structures after 3 days and 7 days incubation.

5.3 3D Printing Hydrogels for *In Vitro* Regeneration of Retina

Recapitulating native retina environment is crucial in isolation and culturing of retina photoreceptors (PRs). To date, maturation of PRs remains incomprehensible *in vitro*. Here we present a strategy of integrating the physical and chemical signals through 3D-bioprinting of hyaluronic acid (HA) hydrogels and co-differentiation of retinal progenitor cells (RPCs) into PRs with the support of retinal-pigment epithelium (RPEs). To mimic the native environment during retinal development, we chemically altered the functionalization of HA hydrogels to match the compressive modulus of HA hydrogels with native retina. RPEs were incorporated in the culturing system to support the differentiation due to their regeneration capabilities. We found that HA with a specific functionalization can yield hydrogels with compressive modulus similar to native retina. This hydrogel is also suitable for 3D bioprinting of retina structure. The results from cell study indicated that derivation of PRs from RPCs was improved in the presence of RPEs.

5.4 Controlled Growth Factor Release from 3D Printed Hydrogels

Growth factors (GFs) are critical components in governing cell fate. Their controlled delivery has been challenging due to their rapid turnover rates *in vivo*. Functionalized hydrogel delivery system, such as heparin-based hydrogels, has demonstrated great potential in regulating GF release for prolonged delivery. The effect of concentration and molecular weights of heparin on retaining GFs has been investigated. However, the role of geometry of their release kinetics has yet been discovered. In this work, we combined our digital light projection (DLP) based 3D printing technology with heparin-based hydrogels to study the release pattern of GFs from core-shell structures. Cylindrical core-shell structures with varied shell thickness were printed, and their release profiles were studied individually. Additionally, a mathematical model was developed to predict GF release kinetics. From the curve-fitting of the equation, we obtained the intrinsic diffusivity of GF from hydrogel, as well as the other parameters, such as partition coefficient. Furthermore, we achieved sequential release of VEGF and PDGF from specially designed hydrogel structure. By switching the spatial order of the two GFs, we successfully changed the release sequence.

5.5 Rapid 3D Printing of Dual Network by Elastomeric and Bioabsorbable Polymer

This study has demonstrated the synthesis of elastomeric PGSA material by esterification and acrylation. The DLP-based micro-scale continuous printing system (ţCOMP) was used to print the polymer into structures sub-100 ţm resolution within minutes. The mechanical properties of the polymers with different concentrations of crosslinkers and exposure duration were examined. The results shown that by modulating these two conditions, the elastic modulus of the printed polymers ranged from 150 kPa to 800 kPa while the ultimate tensile strength expanded from 100 kPa to 300 kPa. All of the printed polymers could sustain more than 50% strain before failure, which is optimal for most of biomedical applications, with some specific combinations reached 100% strain before rupture. Furthermore, a polymer inspired double network structure were printed by allocating hard and soft segments in specific locations using different exposure durations. This double network structure demonstrated enhanced toughness by introducing soft sacrificial arms to absorb the energy during tensile test while the hard segments withstand the overall structure intact. To understand this observation, a finite-element analysis was conducted to evaluate the mechanism. This study has demonstrated methods of fabricating structures with enhanced mechanical properties from elastomeric polymers with long-term goals of developing functional and bioabsorbable medical devices for implementations.

Acknowledgement

The work was supported in part by grants from the Department of Defense (W81XWH-14-1-0522), California Institute for Regenerative Medicine (RT3-07899), and National Institutes of Health (R01EB021857).

Bibliography

[1] O. Bayer, “Das Di-Isocyanat-Polyadditionsverfahren (Polyurethane),” *Angewandte Chemie*, vol. 59, pp. 257–272, sep 1947.

[2] C. Lövenich, R. Albers, L. Brassat, A. Chrisochoou, H. Ehbing, and J. Hättig, “Polyurethanes (PU),” *Kunststoffe International*, vol. 107, no. 10, pp. 46–51, 2017.

[3] A. Murase, A. Angulo, R. Sahara, and O. N. Jiménez, “Color variation of a damselfish, Stegastes flavilatus (Perciformes: Pomacentridae), from the Pacific coast of Costa Rica and comparison with a sympatric congener,” *Pan-American Journal of Aquatic Sciences*, vol. 11, no. 4, pp. 361–366, 2016.

[4] K. Stokes, R. McVenes, and J. M. Anderson, “Polyurethane elastomer biostability.,” *Journal of biomaterials applications*, vol. 9, pp. 321–54, apr 1995.

[5] H. N. Chia and B. M. Wu, “Recent advances in 3D printing of biomaterials.,” *Journal of biological engineering*, vol. 9, p. 4, 2015.

[6] M. J. Cima, E. Sachs, L. G. Cima, S. Khanujal, S. W. Borland, B. Wu, and R. a. Giordano, “Computer-derived microstructures by 3D Printing : Bio and Structural Materials,” *Solid Freeform Fabrication Symposium*, pp. 181–190, 1994.

[7] L. G. Griffith, B. Wu, M. J. Cima, M. J. Powers, B. Chaignaud, and J. P. Vacanti, “In vitro organogenesis of liver tissue.,” *Annals of the New York Academy of Sciences*, vol. 831, pp. 382–97, dec 1997.

[8] B. M. Wu, S. W. Borland, R. A. Giordano, L. G. Cima, E. M. Sachs, and M. J. Cima, “Solid free-form fabrication of drug delivery devices,” *Journal of Controlled Release*, vol. 40, no. 1-2, pp. 77–87, 1996.

[9] P. Bartolo, J.-P. Kruth, J. Silva, G. Levy, A. Malshe, K. Rajurkar, M. Mitsuishi, J. Ciurana, and M. Leu, "Biomedical production of implants by additive electro-chemical and physical processes," *CIRP Annals*, vol. 61, no. 2, pp. 635–655, 2012.

[10] K. Stokes, R. McVenes, and J. M. Anderson, "Polyurethane Elastomer Biostability," *Journal of Biomaterials Applications*, vol. 9, pp. 321–354, apr 1995.

[11] M. J. Wiggins, B. Wilkoff, J. M. Anderson, and A. Hiltner, "Biodegradation of polyether polyurethane inner insulation in bipolar pacemaker leads.," *Journal of biomedical materials research*, vol. 58, pp. 302–7, may 2001.

[12] M. A. Schubert, M. J. Wiggins, J. M. Anderson, and A. Hiltner, "Role of oxygen in biodegradation of poly(etherurethane urea) elastomers.," *Journal of biomedical materials research*, vol. 34, pp. 519–30, mar 1997.

[13] Q. Zhao, N. Topham, J. M. Anderson, A. Hiltner, G. Lodoen, and C. R. Payet, "Foreign-body giant cells and polyurethane biostability:In vivo correlation of cell adhesion and surface cracking," *Journal of Biomedical Materials Research*, vol. 25, pp. 177–183, feb 1991.

[14] S.-h. Hsu, K.-C. Hung, Y.-Y. Lin, C.-H. Su, H.-Y. Yeh, U.-S. Jeng, C.-Y. Lu, S. A. Dai, W.-E. Fu, and J.-C. Lin, "Water-based synthesis and processing of novel biodegradable elastomers for medical applications," *J. Mater. Chem. B*, vol. 2, no. 31, pp. 5083–5092, 2014.

[15] P. Kröber, J. T. Delaney, J. Perelaer, and U. S. Schubert, "Reactive inkjet printing of polyurethanes," *Journal of Materials Chemistry*, vol. 19, no. 29, p. 5234, 2009.

[16] J. Z. Gul, M. Sajid, M. M. Rehman, G. U. Siddiqui, I. Shah, K.-H. Kim, J.-W. Lee, and K. H. Choi, "3D printing for soft robotics a review," *Science and Technology of Advanced Materials*, vol. 19, pp. 243–262, dec 2018.

[17] S. H. Pyo, P. Wang, H. H. Hwang, W. Zhu, J. Warner, and S. Chen, "Continuous optical 3D printing of green aliphatic polyurethanes," *ACS Applied Materials and Interfaces*, vol. 9, no. 1, pp. 836–844, 2017.

[18] R. B. N. Scharff, E. L. Doubrovski, W. A. Poelman, P. P. Jonker, C. C. L. Wang, and J. M. P. Geraedts, "Towards Behavior Design of a 3D-Printed Soft Robotic Hand," in *Soft Robotics: Trends, Applications and Challenges*, pp. 23–29, Springer, Cham, 2017.

[19] S. A. Guelcher, “Biodegradable Polyurethanes: Synthesis and Applications in Regenerative Medicine,” *Tissue Engineering Part B: Reviews*, vol. 14, pp. 3–17, mar 2008.

[20] B. Banjanin, G. Vladić, M. Pál, V. Dimovski, S. Adamović, and G. Delić, “PRODUCTION FACTORS INFLUENCING MECHANICAL AND PHYSICAL PROPERTIES OF FDM PRINTED EMBOSSING DIES,” pp. 225–236, 2018.

[21] Q. Chen, J. D. Mangadlao, J. Wallat, A. De Leon, J. K. Pokorski, R. C. Advincula, A. D. Leon, J. K. Pokorski, and R. C. Advincula, “3D printing biocompatible polyurethane/poly(lactic acid)/graphene oxide nanocomposites: Anisotropic properties,” *ACS Applied Materials and Interfaces*, vol. 9, no. 4, pp. 4015–4023, 2017.

[22] H.-J. Yen, S.-H. Hsu, C.-S. Tseng, J.-P. Huang, and C.-L. Tsai, “Fabrication of Precision Scaffolds Using Liquid-Frozen Deposition Manufacturing for Cartilage Tissue Engineering,” *Tissue Engineering Part A*, vol. 15, pp. 965–975, may 2009.

[23] Wei Xu, Xiao Wang, Yongnian Yan, Renji Zhang, W. Xu, X. Wang, Y. Yan, and R. Zhang, “Rapid prototyping of polyurethane for the creation of vascular systems,” *Journal of Bioactive and Compatible Polymers*, vol. 23, pp. 103–114, mar 2008.

[24] Y. Yan, X. Hong Wang, D. Yin, and R. Zhang, “A New Polyurethane/Heparin Vascular Graft for Small-Caliber Vein Repair,” *Journal of Bioactive and Compatible Polymers*, vol. 22, pp. 323–341, may 2007.

[25] J. Sohier, L. Moroni, C. van Blitterswijk, K. de Groot, and J. M. Bezemer, “Critical factors in the design of growth factor releasing scaffolds for cartilage tissue engineering.,” *Expert opinion on drug delivery*, vol. 5, pp. 543–66, may 2008.

[26] T. B. F. Woodfield, J. Malda, J. de Wijn, F. Péters, J. Riesle, and C. A. van Blitterswijk, “Design of porous scaffolds for cartilage tissue engineering using a three-dimensional fiber-deposition technique.,” *Biomaterials*, vol. 25, pp. 4149–61, aug 2004.

[27] K.-S. Lee, D.-Y. Yang, S. H. Park, and R. H. Kim, “Recent developments in the use of two-photon polymerization in precise 2D and 3D microfabrications,” *Polymers for Advanced Technologies*, vol. 17, pp. 72–82, feb 2006.

[28] J. Park, D. Tahk, C. Ahn, S. G. Im, S.-J. Choi, K.-Y. Suh, and S. Jeon, "Conformal phase masks made of polyurethane acrylate with optimized elastic modulus for 3D nanopatterning," *Journal of Materials Chemistry C*, vol. 2, no. 13, p. 2316, 2014.

[29] J. Liu, H. H. Hwang, P. Wang, G. Whang, and S. Chen, "Direct 3D-printing of cell-laden constructs in microfluidic architectures," *Lab Chip*, vol. 16, no. 8, pp. 1430–1438, 2016.

[30] X. Ma, X. Qu, W. Zhu, Y.-S. Li, S. Yuan, H. Zhang, J. Liu, P. Wang, C. S. E. Lai, F. Zanella, G.-S. Feng, F. Sheikh, S. Chien, and S. Chen, "Deterministically patterned biomimetic human iPSC-derived hepatic model via rapid 3D bioprinting," *Proceedings of the National Academy of Sciences*, p. 201524510, 2016.

[31] W. Zhu, X. Qu, J. Zhu, X. Ma, S. Patel, J. Liu, P. Wang, C. S. E. Lai, M. Gou, Y. Xu, K. Zhang, and S. Chen, "Direct 3D bioprinting of prevascularized tissue constructs with complex microarchitecture," *Biomaterials*, vol. 124, pp. 106–115, 2017.

[32] A. P. Zhang, X. Qu, P. Soman, K. C. Hribar, J. W. Lee, S. Chen, and S. He, "Rapid fabrication of complex 3D extracellular microenvironments by dynamic optical projection stereolithography.," *Advanced materials (Deerfield Beach, Fla.)*, vol. 24, pp. 4266–70, aug 2012.

[33] P. Soman, S. Chen, and D. Y. Fozdar, "Micro-structured biomaterials and fabrication methods therefor," 2013.

[34] X. Qu, W. Zhu, S. Huang, J. Y.-S. Li, S. Chien, K. Zhang, and S. Chen, "Relative impact of uniaxial alignment vs. form-induced stress on differentiation of human adipose derived stem cells.," *Biomaterials*, vol. 34, pp. 9812–8, dec 2013.

[35] S. Suri, L.-H. Han, W. Zhang, A. Singh, S. Chen, and C. E. Schmidt, "Solid freeform fabrication of designer scaffolds of hyaluronic acid for nerve tissue engineering.," *Biomedical microdevices*, vol. 13, pp. 983–93, dec 2011.

[36] W. Zhu, X. Qu, J. Zhu, X. Ma, S. Patel, J. Liu, P. Wang, C. S. E. Lai, M. Gou, Y. Xu, K. Zhang, and S. Chen, "Direct 3D bioprinting of prevascularized tissue constructs with complex microarchitecture.," *Biomaterials*, vol. 124, pp. 106–115, 2017.

[37] W. Zhu, J. Li, Y. J. Leong, I. Rozen, X. Qu, R. Dong, Z. Wu, W. Gao, P. H. Chung, J. Wang, and S. Chen, “3D-Printed Artificial Microfish,” *Advanced Materials*, vol. 27, no. 30, pp. 4411–4417, 2015.

[38] J. Warner, P. Soman, W. Zhu, M. Tom, and S. Chen, “Design and 3D Printing of Hydrogel Scaffolds with Fractal Geometries,” *ACS Biomaterials Science and Engineering*, vol. 2, no. 10, pp. 1763–1770, 2016.

[39] J. Zeltinger, J. K. Sherwood, D. A. Graham, R. Müeller, and L. G. Griffith, “Effect of pore size and void fraction on cellular adhesion, proliferation, and matrix deposition.,” *Tissue engineering*, vol. 7, pp. 557–72, oct 2001.

[40] S. S. Kim, H. Utsunomiya, J. A. Koski, B. M. Wu, M. J. Cima, J. Sohn, K. Mukai, L. G. Griffith, and J. P. Vacanti, “Survival and function of hepatocytes on a novel three-dimensional synthetic biodegradable polymer scaffold with an intrinsic network of channels.,” *Annals of surgery*, vol. 228, pp. 8–13, jul 1998.

[41] C. X. Lam, X. M. Mo, S. H. Teoh, and D. W. Hutmacher, “Scaffold development using 3D printing with a starch-based polymer,” *Materials Science and Engineering C*, vol. 20, no. 1-2, pp. 49–56, 2002.

[42] D. Rus and M. T. Tolley, “Design, fabrication and control of soft robots,” *Nature*, vol. 521, pp. 467–475, may 2015.

[43] D. K. Patel, A. H. Sakhaei, M. Layani, B. Zhang, Q. Ge, and S. Magdassi, “Highly Stretchable and UV Curable Elastomers for Digital Light Processing Based 3D Printing,” *Advanced Materials*, vol. 29, no. 15, pp. 1–7, 2017.

[44] J. Z. Gul, B.-S. Yang, Y. J. Yang, D. E. Chang, and K. H. Choi, “In situ UV curable 3D printing of multi-material tri-legged soft bot with spider mimicked multi-step forward dynamic gait,” *Smart Materials and Structures*, vol. 25, p. 115009, nov 2016.

[45] Y. Yang and Y. Chen, “3D printing of smart materials for robotics with variable stiffness and position feedback,” in *IEEE/ASME International Conference on Advanced Intelligent Mechatronics, AIM*, pp. 418–423, IEEE, jul 2017.

[46] B. R. Whatley, J. Kuo, C. Shuai, B. J. Damon, and X. Wen, “Fabrication of a biomimetic elastic intervertebral disk scaffold using additive manufacturing,” *Biofabrication*, vol. 3, p. 015004, mar 2011.

[47] K.-C. Hung, C.-S. Tseng, and S.-h. Hsu, “Synthesis and 3D Printing of Biodegradable Polyurethane Elastomer by a Water-Based Process for Cartilage Tissue Engineering Applications,” *Advanced Healthcare Materials*, vol. 3, pp. 1578–1587, oct 2014.

[48] F.-Y. Hsieh, H.-H. Lin, and S.-h. Hsu, “3D bioprinting of neural stem cell-laden thermoresponsive biodegradable polyurethane hydrogel and potential in central nervous system repair,” *Biomaterials*, vol. 71, pp. 48–57, dec 2015.

[49] H.-H. Lin, F.-Y. Hsieh, C.-S. Tseng, and S.-h. Hsu, “Preparation and characterization of a biodegradable polyurethane hydrogel and the hybrid gel with soy protein for 3D cell-laden bioprinting,” *Journal of Materials Chemistry B*, vol. 4, no. 41, pp. 6694–6705, 2016.

[50] C.-T. Huang, L. Kumar Shrestha, K. Ariga, and S.-h. Hsu, “A graphenepolyurethane composite hydrogel as a potential bioink for 3D bioprinting and differentiation of neural stem cells,” *Journal of Materials Chemistry B*, vol. 5, no. 44, pp. 8854–8864, 2017.

[51] B. M. Holzapfel, H. Pilge, P. M. Prodinger, A. Toepfer, S. Mayer-Wagner, D. W. Hutmacher, R. Von Eisenhart-Rothe, M. Rudert, R. Gradinger, and H. Rechl, “Customised osteotomy guides and endoprosthetic reconstruction for periacetabular tumours,” *International Orthopaedics*, vol. 38, no. 7, pp. 1435–1442, 2014.

[52] F. M. Chen and X. Liu, “Advancing biomaterials of human origin for tissue engineering,” *Progress in Polymer Science*, vol. 53, pp. 86–168, 2016.

[53] R. Ravichandran, S. Sundarrajan, J. R. Venugopal, S. Mukherjee, and S. Ramakrishna, “Advances in Polymeric Systems for Tissue Engineering and Biomedical Applications,” *Macromolecular Bioscience*, vol. 12, no. 3, pp. 286–311, 2012.

[54] C. Cha, P. Soman, W. Zhu, M. Nikkhah, G. Camci-Unal, S. Chen, and A. Khademhosseini, “Structural Reinforcement of Cell-Laden Hydrogels with Microfabricated Three Dimensional Scaffolds.,” *Biomaterials science*, vol. 2, pp. 703–709, may 2014.

[55] C. Cha, P. Soman, W. Zhu, M. Nikkhah, G. Camci-Unal, S. Chen, and A. Khademhosseini, “Structural Reinforcement of Cell-Laden Hydrogels with Microfabricated Three Dimensional Scaffolds.,” *Biomaterials science*, vol. 2, no. 5, pp. 703–709, 2014.

[56] J. Kucinska-Lipka, I. Gubanska, H. Janik, and M. Sienkiewicz, "Fabrication of polyurethane and polyurethane based composite fibres by the electrospinning technique for soft tissue engineering of cardiovascular system," *Materials Science and Engineering C*, vol. 46, pp. 166–176, 2015.

[57] X. Li, L. Wang, Y. Fan, Q. Feng, F. Z. Cui, and F. Watari, "Nanostructured scaffolds for bone tissue engineering," *Journal of Biomedical Materials Research - Part A*, vol. 101 A, no. 8, pp. 2424–2435, 2013.

[58] C. Zhong, J. Wu, C. A. Reinhart-King, and C. C. Chu, "Synthesis, characterization and cytotoxicity of photo-crosslinked maleic chitosan-polyethylene glycol diacrylate hybrid hydrogels," *Acta Biomaterialia*, vol. 6, no. 10, pp. 3908–3918, 2010.

[59] D. Eglin, D. Mortisen, and M. Alini, "Degradation of synthetic polymeric scaffolds for bone and cartilage tissue repairs," *Soft Matter*, vol. 5, no. 5, p. 938, 2009.

[60] P.-C. Chang, B.-Y. Liu, C.-M. Liu, H.-H. Chou, M.-H. Ho, H.-C. Liu, D.-M. Wang, and L.-T. Hou, "Bone tissue engineering with novel rhBMP2-PLLA composite scaffolds.," *Journal of biomedical materials research. Part A*, vol. 81, no. 4, pp. 771–780, 2007.

[61] P. Singhal, W. Small, E. Cosgriff-Hernandez, D. J. Maitland, and T. S. Wilson, "Low density biodegradable shape memory polyurethane foams for embolic biomedical applications," *Acta Biomaterialia*, vol. 10, no. 1, pp. 67–76, 2014.

[62] A. T. Stevenson, L. M. Reese, T. K. Hill, J. McGuire, A. M. Mohs, R. Shekhar, L. R. Bickford, and A. R. Whittington, "Fabrication and characterization of medical grade polyurethane composite catheters for near-infrared imaging," *Biomaterials*, vol. 54, pp. 168–176, 2015.

[63] Q. Chen, S. Liang, and G. A. Thouas, "Elastomeric biomaterials for tissue engineering," *Progress in Polymer Science*, vol. 38, no. 3-4, pp. 584–671, 2013.

[64] R.S.Bezwada, "U.S. Patent," 2014.

[65] D. Heederik, P. K. Henneberger, and C. A. Redlich, "Primary prevention: Exposure reduction, skin exposure and respiratory protection," *European Respiratory Review*, vol. 21, no. 124, pp. 112–124, 2012.

[66] J. E. Lockey, K. Dunning, T. J. Hilbert, E. Borton, L. Levin, C. H. Rice, R. T. McKay, R. Shipley, C. A. Meyer, C. PErme, and G. K. LeMasters, “HRCT/CT and associated spirometric effects of low libby amphibole asbestos exposure,” *Journal of Occupational and Environmental Medicine (JOEM)*, vol. 57, no. January, pp. 6–13, 2015.

[67] H. Panwar, G. V. Raghuram, D. Jain, A. K. Ahirwar, S. Khan, S. K. Jain, N. Pathak, S. Banerjee, K. K. Maudar, and P. K. Mishra, “Cell cycle deregulation by methyl isocyanate: Implications in liver carcinogenesis,” *Environmental Toxicology*, vol. 29, pp. 284–297, mar 2014.

[68] S.-H. Pyo, P. Persson, M. A. Mollaahmad, K. Sörensen, S. Lundmark, and R. Hatti-Kaul, “Cyclic carbonates as monomers for phosgene- and isocyanate-free polyurethanes and polycarbonates,” *Pure and Applied Chemistry*, vol. 84, no. 3, pp. 637–661, 2011.

[69] S. A. Guelcher, A. Srinivasan, J. E. Dumas, J. E. Didier, S. McBride, and J. O. Hollinger, “Synthesis, mechanical properties, biocompatibility, and biodegradation of polyurethane networks from lysine polyisocyanates,” *Biomaterials*, vol. 29, no. 12, pp. 1762–1775, 2008.

[70] R. E. Chapin, J. Adams, K. Boekelheide, L. E. Gray, S. W. Hayward, P. S. J. Lees, B. S. McIntyre, K. M. Portier, T. M. Schnorr, S. G. Selevan, J. G. Vandenbergh, S. R. Woskie, and M. D. Shelby, “NTP-CERHR expert panel report on the reproductive and developmental toxicity of bisphenol A,” *Birth Defects Research Part B - Developmental and Reproductive Toxicology*, vol. 83, no. 3, pp. 157–395, 2008.

[71] O. Kreye, H. Mutlu, and M. a. R. Meier, “Sustainable routes to polyurethane precursors,” *Green Chemistry*, vol. 15, no. 6, pp. 1431–1455, 2013.

[72] M. S. Kathalewar, P. B. Joshi, A. S. Sabnis, and V. C. Malshe, “Non-isocyanate polyurethanes: from chemistry to applications,” *RSC Advances*, vol. 3, no. 13, p. 4110, 2013.

[73] J. C. Anastas, P. T.; Warner, *Green Chemistry: Theory and Practice,*. New York: Oxford University Press, 1998.

[74] J. D. Holbrey, W. M. Reichert, R. P. Swatloski, G. A. Broker, W. R. Pitner, K. R. Seddon, and R. D. Rogers, “Efficient, halide free synthesis of new, low cost

ionic liquids: 1,3-dialkylimidazolium salts containing methyl- and ethyl-sulfate anions," *Green Chemistry*, vol. 4, no. 5, pp. 407–413, 2002.

[75] K. Kumaravel and G. Vasuki, "Four-component catalyst-free reaction in water: Combinatorial library synthesis of novel 2-amino-4-(5-hydroxy-3-methyl-1H-pyrazol-4-yl)-4H-chromene-3-carbonitrile derivatives," *Green Chemistry*, vol. 11, no. 12, p. 1945, 2009.

[76] A. Loupy, "Solvent-free microwave organic synthesis as an efficient procedure for green chemistry," *Comptes Rendus Chimie*, vol. 7, no. 2, pp. 103–112, 2004.

[77] V. M. Lombardo, E. A. Dhulst, E. K. Leitsch, N. Wilmot, W. H. Heath, A. P. Gies, M. D. Miller, J. M. Torkelson, and K. A. Scheidt, "Cooperative Catalysis of Cyclic Carbonate Ring Opening: Application Towards Non-Isocyanate Polyurethane Materials," *European Journal of Organic Chemistry*, vol. 2015, pp. 2791–2795, may 2015.

[78] H. Tomita, F. Sanda, and T. Endo, "Structural analysis of polyhydroxyurethane obtained by polyaddition of bifunctional five-membered cyclic carbonate and diamine based on the model reaction," *Journal of Polymer Science, Part A: Polymer Chemistry*, vol. 39, no. 6, pp. 851–859, 2001.

[79] S. H. Pyo and R. Hatti-Kaul, "Selective, green synthesis of six-membered cyclic carbonates by lipase-catalyzed chemospecific transesterification of diols with dimethyl carbonate," *Advanced Synthesis and Catalysis*, vol. 354, no. 5, pp. 797–802, 2012.

[80] Y. R. Chang, V. K. Raghunathan, S. P. Garland, J. T. Morgan, P. Russell, and C. J. Murphy, "Automated AFM force curve analysis for determining elastic modulus of biomaterials and biological samples," *Journal of the Mechanical Behavior of Biomedical Materials*, vol. 37, pp. 209–218, 2014.

[81] G. Rokicki, "Aliphatic cyclic carbonates and spiroorthocarbonates as monomers," *Progress in Polymer Science (Oxford)*, vol. 25, no. 2, pp. 259–342, 2000.

[82] Y. Lu, G. Mapili, G. Suhali, S. Chen, and K. Roy, "A digital micro-mirror device-based system for the microfabrication of complex, spatially patterned tissue engineering scaffolds.," *Journal of biomedical materials research. Part A*, vol. 77, pp. 396–405, may 2006.

[83] S.-H. Pyo and R. Hatti-Kaul, "Chlorine-Free Synthesis of Organic Alkyl Carbonates and Five- and Six-Membered Cyclic Carbonates," *Advanced Synthesis & Catalysis*, vol. 358, pp. 834–839, mar 2016.

[84] J. Feng, R. X. Zhuo, and X. Z. Zhang, "Construction of functional aliphatic polycarbonates for biomedical applications," *Progress in Polymer Science (Oxford)*, vol. 37, no. 2, pp. 211–236, 2012.

[85] L. Mespouille, O. Coulembier, M. Kawalec, A. P. Dove, and P. Dubois, "Implementation of metal-free ring-opening polymerization in the preparation of aliphatic polycarbonate materials," *Progress in Polymer Science*, vol. 39, no. 6, pp. 1144–1164, 2014.

[86] V. Ladero, M. Calles-Enriquez, M. Fernandez, and M. A. Alvarez, "Toxicological Effects of Dietary Biogenic Amines," *Current Nutrition & Food Science*, vol. 6, no. 2, pp. 145–156, 2010.

[87] A. A. Askadskii, "Influence of crosslinking density on the properties of polymer networks," *Polymer Science U.S.S.R.*, vol. 32, no. 10, pp. 2061–2069, 1990.

[88] C. Decker, "Kinetic study and new applications of UV radiation curing," *Macromolecular Rapid Communications*, vol. 23, no. 18, pp. 1067–1093, 2002.

[89] X. Qu, W. Zhu, S. Huang, Y. S. Li, S. Chien, K. Zhang, and S. Chen, "Relative impact of uniaxial alignment vs. form-induced stress on differentiation of human adipose derived stem cells," *Biomaterials*, vol. 34, no. 38, pp. 9812–9818, 2013.

[90] K. C. Hribar, D. Finlay, X. Ma, X. Qu, M. G. Ondeck, P. H. Chung, F. Zanella, A. J. Engler, F. Sheikh, K. Vuori, and S. C. Chen, "Nonlinear 3D projection printing of concave hydrogel microstructures for long-term multicellular spheroid and embryoid body culture," *Lab Chip*, vol. 15, no. 11, pp. 2412–2418, 2015.

[91] N. Mitrousis, R. Y. Tam, A. E. G. Baker, D. Van Der Kooy, and M. S. Shoichet, "Hyaluronic Acid-Based Hydrogels Enable Rod Photoreceptor Survival and Maturation in Vitro through Activation of the mTOR Pathway," *Advanced Functional Materials*, vol. 26, no. 12, pp. 1975–1985, 2016.

[92] M. Eiraku, N. Takata, H. Ishibashi, M. Kawada, E. Sakakura, S. Okuda, K. Sekiguchi, T. Adachi, and Y. Sasai, "Self-organizing optic-cup morphogenesis in three-dimensional culture," *Nature*, vol. 472, pp. 51–56, apr 2011.

[93] Y. Liu, R. Wang, T. I. Zarembinski, N. Doty, C. Jiang, C. Regatieri, X. Zhang, and M. J. Young, "The Application of Hyaluronic Acid Hydrogels to Retinal Progenitor Cell Transplantation," *Tissue Engineering Part A*, vol. 19, pp. 135–142, jan 2013.

[94] B. G. Ballios, M. J. Cooke, L. Donaldson, B. L. K. Coles, C. M. Morshead, D. van derăKooy, M. S. Shoichet, D. van der Kooy, and M. S. Shoichet, "A Hyaluronan-Based Injectable Hydrogel Improves the Survival and Integration of Stem Cell Progeny following Transplantation," *Stem Cell Reports*, vol. 4, no. 6, pp. 1–15, 2015.

[95] A. E. Sorkio, E. P. Vuorimaa-Laukkanen, H. M. Hakola, H. Liang, T. a. Ujula, J. J. Valle-Delgado, M. Österberg, M. L. Yliperttula, and H. Skottman, "Biomimetic collagen I and IV double layer LangmuirSchaefer films asămicroenvironment for human pluripotent stem cell derived retinal pigment epithelial cells," *Biomaterials*, vol. 51, pp. 257–269, 2015.

[96] P. Baranov, a. Michaelson, J. Kundu, R. L. Carrier, and M. Young, "Interphotoreceptor matrix-poly(ă-caprolactone) composite scaffolds for human photoreceptor differentiation," *Journal of Tissue Engineering*, vol. 5, no. 0, 2014.

[97] C. Yvon, C. M. Ramsden, A. Lane, M. B. Powner, L. da Cruz, P. J. Coffey, and A.-J. F. Carr, "Using stem cells to model diseases of the outer retina," *Computational and Structural Biotechnology Journal*, 2015.

[98] C. M. Ramsden, M. B. Powner, A.-J. F. Carr, M. J. K. Smart, L. da Cruz, and P. J. Coffey, "Stem cells in retinal regeneration: past, present and future.," *Development (Cambridge, England)*, vol. 140, no. 12, pp. 2576–85, 2013.

[99] S. T. H. David E. Buchholz, "E MBRYONIC S TEM C ELLS / I NDUCED P LURIPOTENT S TEM C ELLS Derivation of Functional Retinal Pigmented Epithelium from Induced," *Stem Cells*, vol. 27, pp. 2427–2434, 2009.

[100] J. Luo, P. Baranov, S. Patel, H. Ouyang, J. Quach, F. Wu, A. Qiu, H. Luo, C. Hicks, J. Zeng, J. Zhu, J. Lu, N. Sfeir, C. Wen, M. Zhang, V. Reade, S. Patel, J. Sinden, X. Sun, P. Shaw, M. Young, and K. Zhanga, "Human retinal progenitor cell transplantation preserves vision," *Journal of Biological Chemistry*, vol. 289, no. 10, pp. 6362–6371, 2014.

[101] R. Zhu, M. A. Millrod, E. T. Zambidis, and L. Tung, “Variability of Action Potentials Within and Among Cardiac Cell Clusters Derived from Human Embryonic Stem Cells,” *Scientific Reports*, vol. 6, no. 1, p. 18544, 2016.

[102] X. Zhong, C. Gutierrez, T. Xue, C. Hampton, M. N. Vergara, L.-H. Cao, A. Peters, T. S. Park, E. T. Zambidis, J. S. Meyer, D. M. Gamm, K.-W. Yau, and M. V. Canto-Soler, “Generation of three-dimensional retinal tissue with functional photoreceptors from human iPSCs.,” *Nature communications*, vol. 5, no. May, p. 4047, 2014.

[103] B. Lorber, W.-K. K. Hsiao, I. M. Hutchings, and K. R. Martin, “Adult rat retinal ganglion cells and glia can be printed by piezoelectric inkjet printing,” *Biofabrication*, vol. 6, no. 1, p. 015001, 2014.

[104] N. C. Hunt, D. Hallam, A. Karimi, C. B. Mellough, J. Chen, D. H. Steel, and M. Lako, “3D culture of human pluripotent stem cells in alginate hydrogel improves retinal tissue development,” *Acta Biomaterialia*, 2016.

[105] J. A. Burdick and G. D. Prestwich, “Hyaluronic acid hydrogels for biomedical applications,” *Advanced Materials*, vol. 23, no. 12, pp. 41–56, 2011.

[106] D. L. Hern and J. A. Hubbell, “Incorporation of adhesion peptides into nonadhesive hydrogels useful for tissue resurfacing,” *Journal of Biomedical Materials Research*, vol. 39, no. 2, pp. 266–276, 1998.

[107] K. C. Hribar, P. Soman, J. Warner, P. Chung, and S. Chen, “Light-assisted direct-write of 3D functional biomaterials.,” *Lab on a chip*, vol. 14, no. 2, pp. 268–75, 2014.

[108] F. Zhao, J. Kreutzer, S. Pajunen, and P. Kallio, “Mechanical analysis of a pneumatically actuated concentric double-shell structure for cell stretching,” *Micromachines*, vol. 5, no. 4, pp. 868–885, 2014.

[109] J. Baier Leach, K. a. Bivens, C. W. Patrick Jr., and C. E. Schmidt, “Photocrosslinked hyaluronic acid hydrogels: Natural, biodegradable tissue engineering scaffolds,” *Biotechnology and Bioengineering*, vol. 82, no. 5, pp. 578–589, 2003.

[110] K. S. Worthington, L. A. Wiley, A. M. Bartlett, E. M. Stone, R. F. Mullins, A. K. Salem, C. A. Guymon, and B. A. Tucker, “Mechanical properties of murine and porcine ocular tissues in compression,” *Experimental Eye Research*, vol. 121, pp. 194–199, 2014.

[111] J. Hertz, R. Robinson, D. a. Valenzuela, E. B. Lavik, and J. L. Goldberg, “A tunable synthetic hydrogel system for culture of retinal ganglion cells and amacrine cells,” *Acta Biomaterialia*, vol. 9, pp. 7622–7629, aug 2013.

[112] T. Nakano, S. Ando, N. Takata, M. Kawada, K. Muguruma, K. Sekiguchi, K. Saito, S. Yonemura, M. Eiraku, and Y. Sasai, “Self-formation of optic cups and storable stratified neural retina from human ESCs,” *Cell Stem Cell*, vol. 10, no. 6, pp. 771–785, 2012.

[113] H. Kolb, “Facts and Figures Concerning the Human Retina Size of Optic Nerve Head or Disc Cross Diameter of the Macula Cross Diameter of the Central Fovea from Foveal Rim to Foveal Rim Cross Diameter of Central Rod-free Area Central Region of Fovea Where There Are N,” no. 1, pp. 1–10, 2007.

[114] S. Schmitt, U. Aftab, C. Jiang, S. Redenti, H. Klassen, E. Miljan, J. Sinden, and M. Young, “Molecular characterization of human retinal progenitor cells.,” *Investigative ophthalmology & visual science*, vol. 50, no. 12, pp. 5901–5908, 2009.

[115] K.-W. Lee and Y. Wang, “Elastomeric PGS Scaffolds in Arterial Tissue Engineering,” *Journal of Visualized Experiments*, no. 50, pp. 1–6, 2011.

[116] D. L. Stocum, “New Tissues from Old,” *Science*, vol. 276, pp. 15–0, apr 1997.

[117] J. Li and D. J. Mooney, “Designing hydrogels for controlled drug delivery,” *Nature Reviews Materials*, vol. 1, no. 12, p. 16071, 2016.

[118] M. Yamamoto, Y. Ikada, and Y. Tabata, “Controlled release of growth factors based on biodegradation of gelatin hydrogel.,” *Journal of biomaterials science. Polymer edition*, vol. 12, no. 1, pp. 77–88, 2001.

[119] M. J. Whitaker, R. A. Quirk, S. M. Howdle, and K. M. Shakesheff, “Growth factor release from tissue engineering scaffolds.,” *The Journal of pharmacy and pharmacology*, vol. 53, pp. 1427–37, nov 2001.

[120] J. Su, B.-H. Hu, W. L. Lowe, D. B. Kaufman, and P. B. Messersmith, “Anti-inflammatory peptide-functionalized hydrogels for insulin-secreting cell encapsulation.,” *Biomaterials*, vol. 31, pp. 308–14, jan 2010.

[121] P. J. Butterworth, “Lehninger: principles of biochemistry (4th edn) D. L. Nelson and M. C. Cox, W. H. Freeman & Co., New York, 1119 pp (plus 17 pp

glossary), ISBN 0-7167-4339-6 (2004)," *Cell Biochemistry and Function*, vol. 23, pp. 293–294, jul 2005.

[122] A. Fu, K. Gwon, M. Kim, G. Tae, and J. A. Kornfield, "Visible-light-initiated thiol-acrylate photopolymerization of heparin-based hydrogels," *Biomacromolecules*, vol. 16, no. 2, pp. 497–506, 2015.

[123] D. B. Pike, S. Cai, K. R. Pomraning, M. A. Firpo, R. J. Fisher, X. Z. Shu, G. D. Prestwich, and R. A. Peattie, "Heparin-regulated release of growth factors in vitro and angiogenic response in vivo to implanted hyaluronan hydrogels containing VEGF and bFGF," *Biomaterials*, vol. 27, no. 30, pp. 5242–5251, 2006.

[124] J. Wu, J. Ye, J. Zhu, Z. Xiao, C. He, H. Shi, Y. Wang, C. Lin, H. Zhang, Y. Zhao, X. Fu, H. Chen, X. Li, L. Li, J. Zheng, and J. Xiao, "Heparin-Based Coacervate of FGF2 Improves Dermal Regeneration by Asserting a Synergistic Role with Cell Proliferation and Endogenous Facilitated VEGF for Cutaneous Wound Healing," *Biomacromolecules*, vol. 17, no. 6, pp. 2168–2177, 2016.

[125] G. Tae, Y. J. Kim, W. I. Choi, M. Kim, P. S. Stayton, and A. S. Hoffman, "Formation of a novel heparin-based hydrogel in the presence of heparin-binding biomolecules," *Biomacromolecules*, vol. 8, no. 6, pp. 1979–1986, 2007.

[126] A. K. Jha, A. Mathur, F. L. Svedlund, J. Ye, Y. Yeghiazarians, and K. E. Healy, "Molecular weight and concentration of heparin in hyaluronic acid-based matrices modulates growth factor retention kinetics and stem cell fate," *Journal of Controlled Release*, vol. 209, pp. 308–316, 2015.

[127] C. A. Collins, V. F. Gnocchi, R. B. White, L. Boldrin, A. Perez-Ruiz, F. Relaix, J. E. Morgan, and P. S. Zammit, "Integrated functions of Pax3 and Pax7 in the regulation of proliferation, cell size and myogenic differentiation," *PLoS ONE*, vol. 4, no. 2, 2009.

[128] A. D. Rape, M. Zibinsky, N. Murthy, and S. Kumar, "A synthetic hydrogel for the high-throughput study of cell-ECM interactions.," *Nature communications*, vol. 6, no. May, p. 8129, 2015.

[129] P. Wang, X. Li, W. Zhu, Z. Zhong, A. Moran, W. Wang, K. Zhang, and S. Chen, "3D bioprinting of hydrogels for retina cell culturing," *Bioprinting*, vol. 12, no. September, pp. 1–6, 2018.

[130] A. K. Jha, K. M. Tharp, J. Ye, J. L. Santiago-Ortiz, W. M. Jackson, A. Stahl, D. V. Schaffer, Y. Yeghiazarians, and K. E. Healy, "Enhanced survival and engraftment of transplanted stem cells using growth factor sequestering hydrogels," *Biomaterials*, vol. 47, pp. 1–12, apr 2015.

[131] J. Siepmann and F. Siepmann, "Modeling of diffusion controlled drug delivery," *Journal of Controlled Release*, vol. 161, no. 2, pp. 351–362, 2012.

[132] S. Muschert, F. Siepmann, B. Leclercq, B. Carlin, and J. Siepmann, "Prediction of drug release from ethylcellulose coated pellets," *Journal of Controlled Release*, vol. 135, no. 1, pp. 71–79, 2009.

[133] S. P. Zustiak, H. Boukari, and J. B. Leach, "Solute diffusion and interactions in cross-linked poly(ethylene glycol) hydrogels studied by Fluorescence Correlation Spectroscopy," *Soft Matter*, vol. 6, no. 15, p. 3609, 2010.

[134] M. H. Hettiaratchi, A. Schudel, T. Rouse, A. J. García, S. N. Thomas, R. E. Guldberg, and T. C. McDevitt, "A rapid method for determining protein diffusion through hydrogels for regenerative medicine applications," *APL Bioengineering*, vol. 2, p. 026110, jun 2018.

[135] A. P. Zhang, X. Qu, P. Soman, K. C. Hribar, J. W. Lee, S. Chen, and S. He, "Rapid fabrication of complex 3D extracellular microenvironments by dynamic optical projection stereolithography," *Advanced Materials*, vol. 24, no. 31, pp. 4266–4270, 2012.

[136] P. Soman, P. H. Chung, A. P. Zhang, and S. Chen, "Digital microfabrication of user-defined 3D microstructures in cell-laden hydrogels," *Biotechnology and Bioengineering*, vol. 110, no. 11, pp. 3038–3047, 2013.

[137] J. Koffler, W. Zhu, X. Qu, O. Platoshyn, J. N. Dulin, J. Brock, L. Graham, P. Lu, J. Sakamoto, M. Marsala, S. Chen, and M. H. Tuszynski, "Biomimetic 3D-printed scaffolds for spinal cord injury repair," *Nature Medicine*, vol. 25, no. February, 2019.

[138] D. B. Berry, S. You, J. Warner, L. R. Frank, S. Chen, and S. R. Ward, "A 3D Tissue-Printing Approach for Validation of Diffusion Tensor Imaging in Skeletal Muscle," *Tissue Engineering Part A*, vol. 23, pp. 980–988, sep 2017.

[139] Y. Liang and K. L. Kiick, "Heparin-functionalized polymeric biomaterials in tissue engineering and drug delivery applications," *Acta Biomaterialia*, vol. 10, pp. 1588–1600, apr 2014.

[140] D. S. Benoit and K. S. Anseth, “Heparin functionalized PEG gels that modulate protein adsorption for hMSC adhesion and differentiation,” *Acta Biomaterialia*, vol. 1, pp. 461–470, jul 2005.

[141] K. Gwon, E. Kim, and G. Tae, “Heparin-hyaluronic acid hydrogel in support of cellular activities of 3D encapsulated adipose derived stem cells,” *Acta Biomaterialia*, vol. 49, pp. 284–295, 2017.